AD-A164 815   PLASMA THEORY AND SIMULATION(U) CALIFORNIA UNIV   1/1
BERKELEY ELECTRONICS RESEARCH LAB   C K BIRDSALL
31 DEC 84 N00014-77-C-0578

UNCLASSIFIED   F/G 20/9   NL

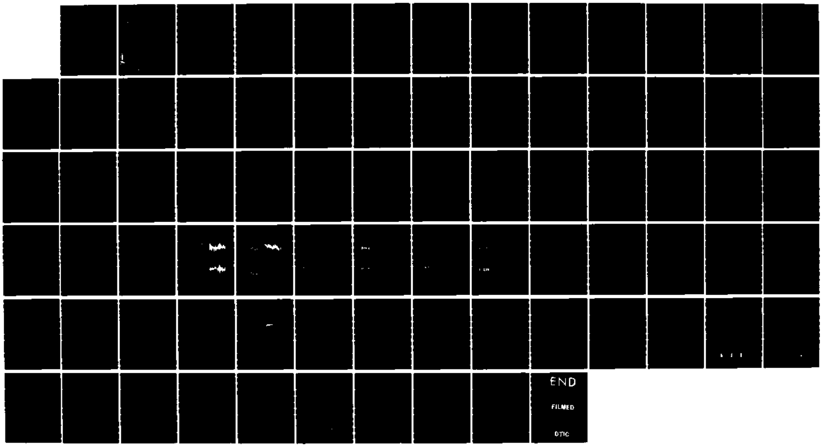

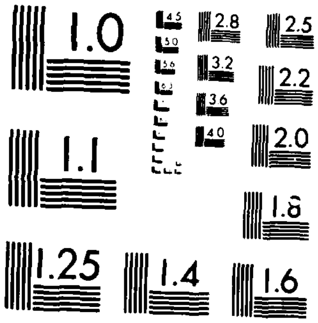

MICROCOPY RESOLUTION TEST CHART
NATIONAL BUREAU OF STANDARDS 1963-A

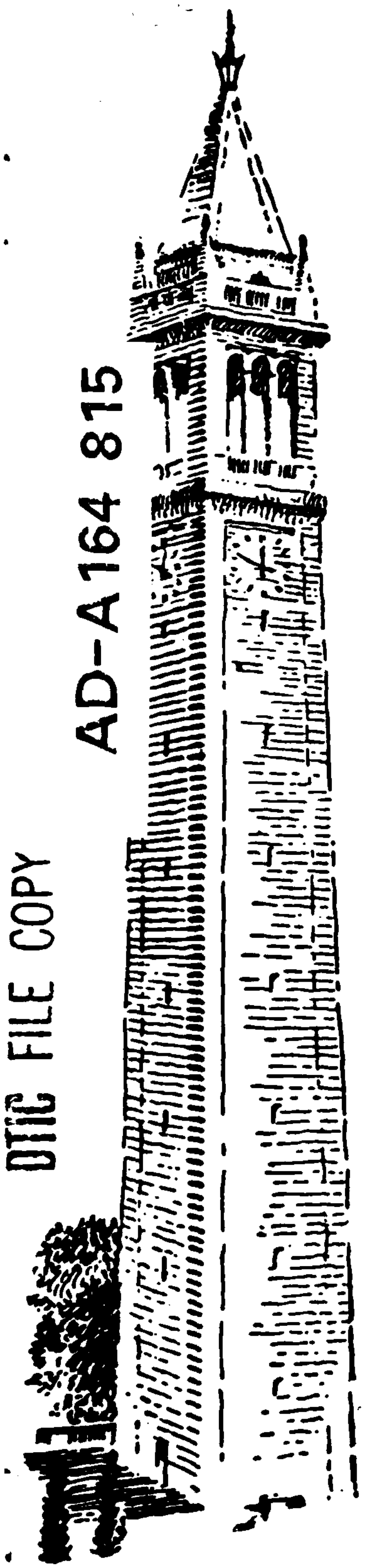

THIRD & FOURTH QUARTER PROGRESS REPORT 1984
ON PLASMA THEORY AND SIMULATION

July 1 to December 31, 1984

DOE Contract DE-AS03-76-F00034-DE-AT03-76ET53064
ONR Contract N00014-77-C-0578
Varian Associates Gift

ELECTRONICS RESEARCH LABORATORY

College of Engineering
University of California, Berkeley, CA 94720

SECURITY CLASSIFICATION OF THIS PAGE (When Data Entered)

REPORT DOCUMENTATION PAGE

READ INSTRUCTIONS
BEFORE COMPLETING FORM

1. REPORT NUMBER

2. GOVT ACCESSION NO. [illegible]

3. RECIPIENT'S CATALOG NUMBER

4. TITLE (and Subtitle)
Quarterly Progress Report III, IV
July 1, 1984 - December 31, 1984

5. TYPE OF REPORT & PERIOD COVERED
Progress, 7/1 - 12/30, 1984

6. PERFORMING ORG. REPORT NUMBER

7. AUTHOR(s)
Professor Charles K. Birdsall

8. CONTRACT OR GRANT NUMBER(s)
ONR N00014-77-C-0578

9. PERFORMING ORGANIZATION NAME AND ADDRESS
Electronics Research Laboratory
University of California
Berkeley, CA 94720

10. PROGRAM ELEMENT, PROJECT, TASK AREA & WORK UNIT NUMBERS
Element No. 61153N, Project Task Area RR01-09-01, Work Unit No. NR 012-742

11. CONTROLLING OFFICE NAME AND ADDRESS
ONR Physics Division
Department of the Navy, ONR
Arlington, VA 22217

12. REPORT DATE

13. NUMBER OF PAGES

14. MONITORING AGENCY NAME & ADDRESS (if different from Controlling Office)

15. SECURITY CLASS. (of this report)
Unclassified

15a. DECLASSIFICATION/DOWNGRADING SCHEDULE

16. DISTRIBUTION STATEMENT (of this Report)

Approved for public release; distribution unlimited

17. DISTRIBUTION STATEMENT (of the abstract entered in Block 20, if different from Report)

18. SUPPLEMENTARY NOTES
Our group uses theory and simulation as tools in order to increase the understanding of instabilities, heating, transport, and other phenomena in plasmas. We also work on the improvement of simulation both theoretically and practically

19. KEY WORDS (Continue on reverse side if necessary and identify by block number)

Research in plasma theory and simulation

20. ABSTRACT (Continue on reverse side if necessary and identify by block number)

Theory and Simulation

A. Oblique electron Bernstein wave investigations. Simulations of a plasma driven by these waves are continued. The thermodynamics of the simulations are checked using the fluctuation-dissipation theorem. The behavior of the waves is compared to linear dispersion theory, and the onsets of nonlinear effects are described.

B. Simulation of the effect of large amplitude RF waves on the interchange instability. The theoretical groundwork has been laid for both the theory

continues other side

and simulationof the stability of the interchange mode in the presence of an RF wave. Physically intuitive properties of the simulation equations have been found and estimates of RF wave quantities have been derived.

C. One-beam Alfvén ion-cyclotron instabilities of multibeam ion distribution functions. It is shown that for large wave numbers k, the Alfvén ion-cyclotron instability in the presence of a mult8ple-beam distribution function is dominated by the response of a single resonant beam.

D. Linear mode coupling in simulations of the Alfvén ion-cyclotron instability. Simulations of the Alfvén ion-cyclotron instability show that modes with $k > \omega_{eI}/v_A$ are strongly coupled to each other. This coupling arises from spatial non-uniformity due to the particle discreteness. A linear theory of the coupling is derived.

E. A model of the plasma-sheath region including ion reflection. Present simulation studies indicate that increasing ion reflection increases the electrostatic potential drop across the sheath region. A theory is derived for the dependence of the potential on the reflection coefficient for cold and warm ions. Regimes where this theory is not applicable are described qualitatively.

F. Planar magnetron discharges. We are using two approaches to understand crossed-field (magnetron) discharges: experiments and computer simulations. We are proceeding with the design and construction of a planar discharge of potentials, fields, densities and velocities as a function of a variety of parameters. We are also using plasma computer simulation for a similar configuration in order to measure the same qualities.

G. Particle simulations of the low-alpha Pierce diode. Particle simulations are used to study the evolution of small initial perturbations about the classical Pierce diode equilibrium in the parameter range $0 < \alpha \equiv \omega_p L/v_0 < 3\pi$. Linear properties recovered show quantitative agreement with theoretical predictions.

H. Theory and simulationof ion-acoustic double layers. The formation of double layers is investigated under the conditions $m_i/m_e = 100$ and $T << T_e$. It is found that weak ion-acoustic double layers can form even in short systems ($80\ \lambda_e$) and with relatively small electron drift ($v = 0.45\ v_{tk} = 4.5\ c$).

Code Development

A. Uniform number generation (for quiet starts). We describe a simple pseidu-random number generator based on n-reversing.

TABLE OF CONTENTS

---

*Supported in part by ONR

**Supported in part by Varian Associates

THIRD AND FOURTH QUARTER PROGRESS REPORT
ON
PLASMA THEORY AND SIMULATION

July 1 to December 31, 1984

Our research group uses both theory and simulation as tools in order to increase the understanding of instabilities, heating, transport, and other phenomena in plasmas. We also work on the improvement of simulation, both theoretically and practically.

Our staff is -

Professor C. K. Birdsall *Principal Investigator*	191M	Cory Hall	(643-6631)
Dr. Ilan Roth (part time); *Research Physicist, Space Science Lab, UCB*	187M	Cory Hall	(642-3477)
Dr. Kim Theilhaber (starting November); *Post-Doctorate; UCB*	187M	Cory Hall	(642-3477)
Dr. Bruce Cohen	L630	LLNL	(422-9823)
Dr. A. Bruce Langdon	L477	LLNL	(422-5444)
Dr. William Nevins	L630	LLNL	(422-7032)
Adjunct Lectureres, UCB; Physicists LLNL			
Mr. Perry Gray *Senior Engineering Aide*	119ME	Cory Hall	(642-3528)
Mr. William Lawson			
Mr. Niels Otani			
Ms. Lou Ann Schwager			
Mr. Damon Gath-de la Rosa			
Research Assistants	119MD	Cory Hall	(642-1297)
	119ME	Cory Hall	(642-3528)

December 31, 1984

DOE Contract DE-AS03-76-F00034-DE-AT03-76ET53064
ONR Contract N00014-C-0578
Varian Associated Gift

ELECTRONICS RESEARCH LABORATORY

University of California
Berkeley, California 94720

SECTION I: PLASMA THEORY AND SIMULATION

A. Oblique Electron Bernstein Wave Investigations

Wm. S. Lawson

Much progress has been made in the investigations of electron Bernstein waves begun last year using a modification of the code PDW1. Some results of interest are here detailed.

BWADR – linear dispersion relation code

The BWADR code (due to Jens-Peter Lynov), was written to compute the complex dispersion curves for oblique Bernstein waves The resulting curve show some interesting features, and are worthy of discussion. The parameters chosen are $\omega_p / \omega_c = 2$ and $\vartheta = 80°$. The real and imaginary parts of k are plotted for real ω.

Figure 1a shows the frequency region between 0 and ω_c. There is no mode in this region for normal Bernstein waves ($\vartheta = 90°$). The mode is, however, derivable from cold MHD theory. It has the dispersion relation (which includes the upper hybrid mode)

$$\omega^4 - (\omega_p^2 + \omega_c^2)\omega^2 + \omega_p^2\omega_c^2\cos^2\vartheta = 0$$

These modes are plotted versus ϑ in figure 1b. The lower mode degenerates to a static mode at $\vartheta = 90°$, and to an $\mathbf{E} = 0$ mode at $\vartheta = 0°$. This mode may well be unobservable for normal plasma parameters when *electromagnetic effects are* taken into account.

Figure 2 shows the frequency region between ω_c and $2\omega_c$. The normal Bernstein dispersion curve is shown for comparison. For a time, the two are very close, but for larger k values the damping rate becomes large, and the real part of k shifts drastically. This branch of the wave was used for most of the simulations.

Figure 3a shows the next frequency interval, that between $2\omega_c$ and $3\omega_c$. This interval shows *two* modes of importance. The structure of the modes is especially interesting in comparison to the normal Bernstein wave curve (figure 3b). The forward and backward portions of the curve for normal waves splits into two branches, each of which is purely forward or purely backward. Both modes have large damping rates above the maximum in ω for normal waves, and the backward wave has large damping below that maximum. The first part of the forward wave, however, has very little damping. This wave corresponds to the upper hybrid wave of MHD, and is the dominant wave in the noise spectrum.

In figure 4, it can be seen that the higher harmonics are rapidly becoming unimportant because of very strong damping. Higher harmonics are so strongly damped, that they can be for all intents and purposes ignored.

Fluctuation Dissipation Check

One problem which became apparent early, was the high noise level in the simulations, even for large numbers of particles. This suggested a method of checking the operation of the code, namely to compare the noise level with the level predicted by the fluctuation- dissipation theorem. This theorem states that

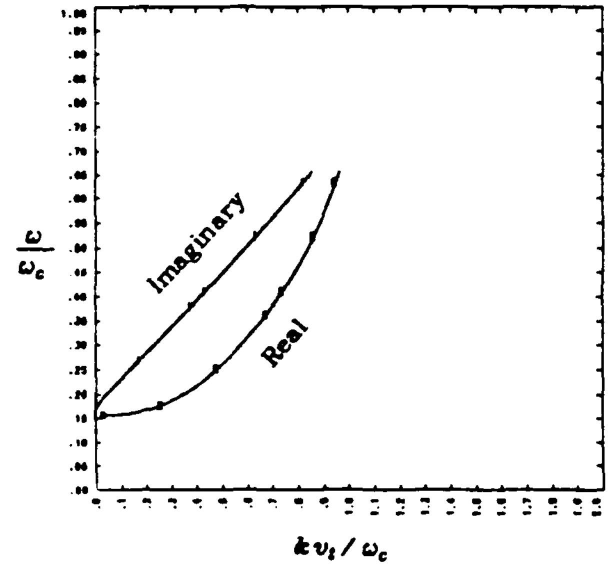

Figure 1a. $\vartheta=80°$, $0<\omega<\omega_c$

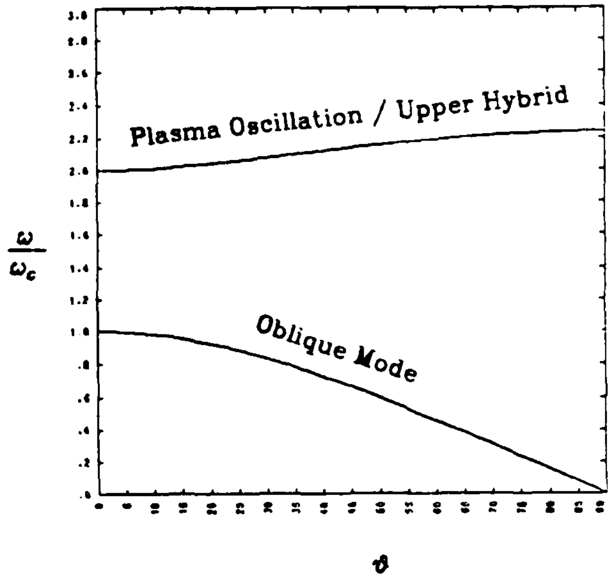

Figure 1b. ω vs. ϑ at $k=0$

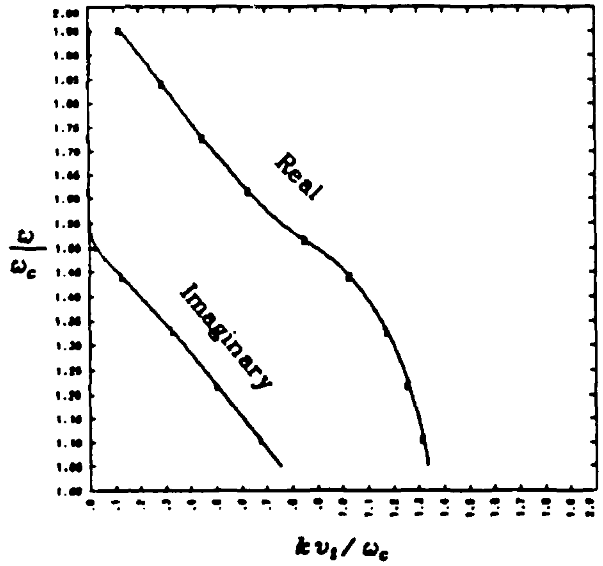

Figure 2a. $\vartheta=80°$, $\omega_c<\omega<2\omega_c$

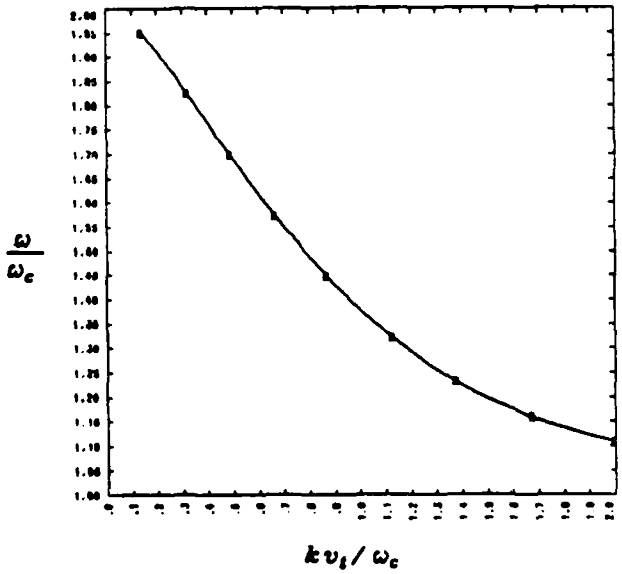

Figure 2b. $\vartheta=90°$, $\omega_c<\omega<2\omega_c$

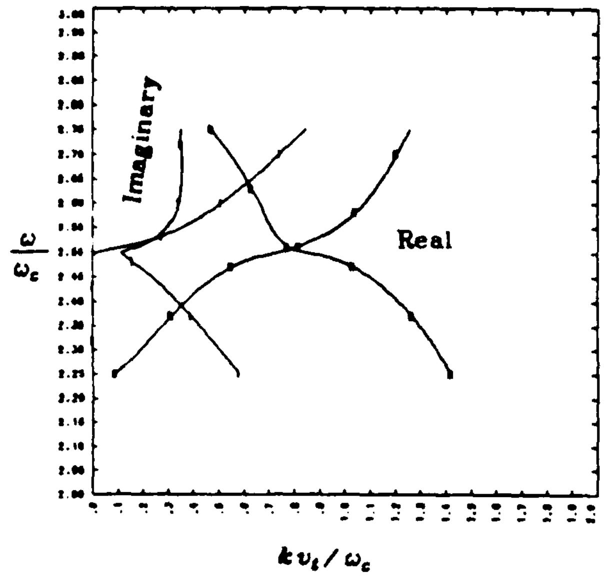

Figure 3a. $\vartheta=80^\circ$, $2\omega_c<\omega<3\omega_c$ (two roots)

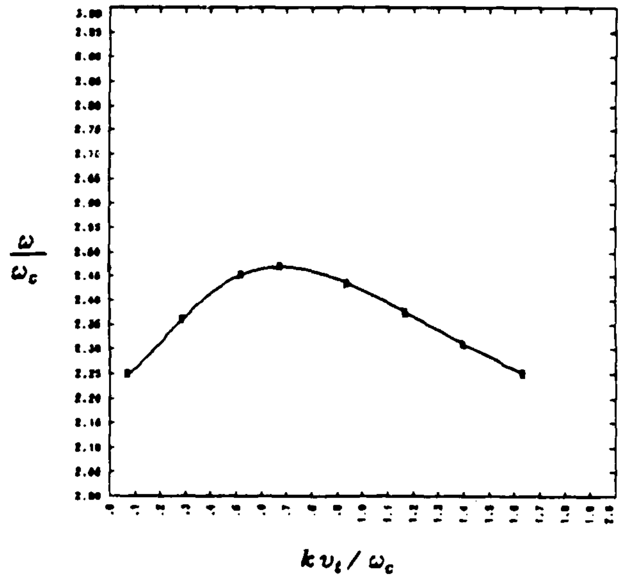

Figure 3b. $\vartheta=90^\circ$, $2\omega_c<\omega<3\omega_c$

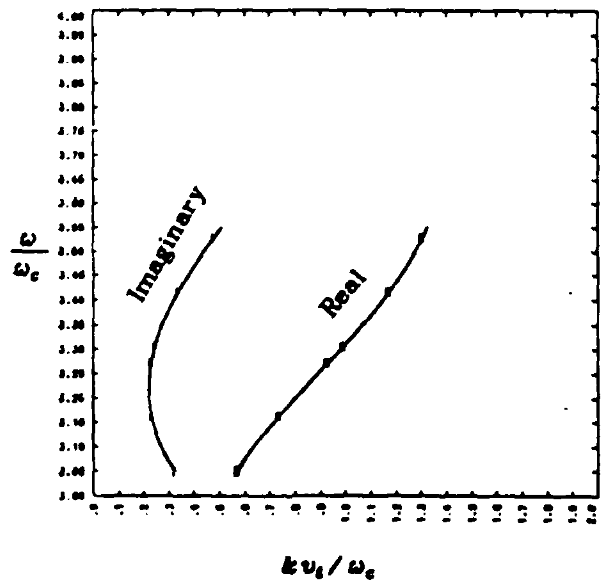

Figure 4a. $\vartheta=80^\circ$, $3\omega_c<\omega<4\omega_c$

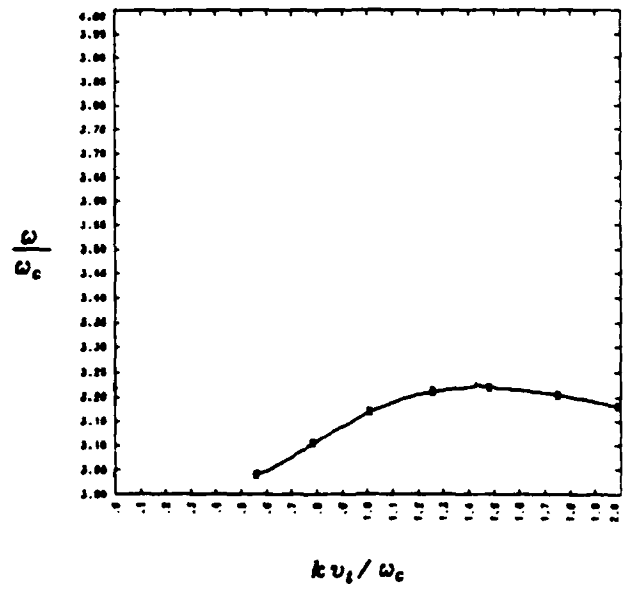

Figure 4b. $\vartheta=90^\circ$, $3\omega_c<\omega<4\omega_c$

$$<|E(k,\omega)|^2> = \frac{2\kappa T}{\omega}\frac{\mathrm{Im}\,\varepsilon(k,\omega)}{|\varepsilon(k,\omega)|^2}$$

or integrated,

$$<|E(\omega)|^2> = \frac{2\kappa T}{\omega}\int_{-\infty}^{\infty}\frac{\mathrm{Im}\,\varepsilon(k,\omega)}{|\varepsilon(k,\omega)|^2}\,\frac{dk}{2\pi}$$

A similar method was used successfully by Kamimura, Wagner, and Dawson [1] in two-dimensional simulations of perpendicular Bernstein waves.

The post-processor ZED (with some modification) was used to compute the fluctuation spectrum of the electric field at a point one quarter of the way across the system from the source. The result is seen in figure 5. Plotted are the theoretical and observed values of $<|E(\omega)|^2>/2kT$ versus frequency (note that for a given ω_p and v_t, T is a function of the particle number density).

The numerical integration of the theoretical spectrum deserves some comment, as it is not simple. The integrand has resonances in it, some of them very narrow and strong. These resonances must be subtracted to two orders in the width parameter in order to get something smooth enough to integrate numerically. Even this function is less than ideal, but the algebra of subtracting another order is much more difficult.

The resolution is, of course, much higher in the theoretical plot, but the degree of agreement can be seen by comparing a broad peak such as the one at $\omega=3.2\omega_c$. One apparent point of disagreement is the appearance of peaks at ω_c and $2\omega_c$ in the simulation. The origin of these peaks, if they are indeed real, is unknown, but the peaks may be due to the finite size particle approximation. This agreement between the theoretical and observed spectra gives some confidence in the accuracy of the simulation.

To see the magnitude of the noise relative to the signal in a typical driven run, figure 6 shows a spectrum plot of such a run at an excitation amplitude which just begins to show some non-linear effects. All these simulations used 130,000 particles – a large number for a one dimensional simulation. A heuristic reason for the high noise level is the large number of phase space dimensions (four) which must be filled. Just as increasing the number of spatial dimensions increases noise, so does increasing the number of velocity dimensions.

Linear and Non-linear Amplitudes

To find the limits of linear behavior, and the character of non-linear behavior, a set of runs was made at one set of parameters for varying excitation amplitudes. The observed *spatial* damping was then compared to linear theory and examined for interesting phenomena. These parameters are $\vartheta=80°$, $\omega_p/\omega_c=2$, $\omega_0/\omega_c=1.45$ (ω_0 is the driving frequency), and the length of the system was sixty-four thermal gyroradii. The results were rather interesting, and will be discussed, but first the method of obtaining the diagnostic plots must be discussed, as the diagnostic is not straight-forward.

Because of the high noise level, even very non-linear signals would be unobservable unless the noise were filtered out somehow. The method used to do this was to wait until the system had come to equilibrium, then take a running Fourier transform *at the driving frequency only*. This results in plots of the real and imaginary parts of $E(x,\omega_0)$. These profiles were then squared and added, and plotted on a log scale, yielding a plot of $\ln|E(x,\omega_0)|^2$ versus x.

Linear theory predicts that this plot should be a straight line.

The lowest amplitude excited is plotted in figure 7. The deviations from a straight line are small, and show no structure. The over-all slope of the curve is a very good match to the straight line of linear theory. Thus it is fair to conclude that the system is behaving in a linear fashion, and that linear theory is accurate in some neighborhood of the chosen parameters.

The next plot (figure 8) shows an excitation amplitude twice that of the first. The decay rate is still a good match with the linear decay rate, but beats and a plateau have appeared. Since these beats disappear when the left wall is made absorbing (and emitting) rather than reflecting, the beats can be ascribed to a ballistic mode which has traveled through the exciter, i. e. the electrons have been bunched in the process of damping the wave (which has a phase velocity moving *toward* the exciter).

The third plot (figure 9) is again at twice the amplitude of the previous one. Now a region of reduced damping near the exciter becomes evident. This is almost certainly evidence of the onset of trapping. The wave can be damped only to a point at the linear rate, then a slower process must take over.

This becomes clear in the next plot (figure 10), which is at five times the previous excitation level. Now the electrons are incapable of damping any but a small fraction of the wave energy (except at the wall, where the damping processes are presumably of a different nature). The wavelength of this wave has also roughly doubled, though this may be due to the heating of the distribution. The reason for the heating is also unclear. It may be due to the passage of the wave, but it seems more likely that it is due to the exciter itself.

The final figure (figure 11) shows an excitation amplitude of ten times the previous one. Now the damping returns at almost the linear rate, but the process must be different. The most likely explanation is a surfing effect which occurs when the electric field is large compared to $\mathbf{v}\times\mathbf{B}$ [2]. This effect can result in large damping even for Bernstein waves at 90° to the magnetic field.

[1] Kamimura, Wagner, and Dawson, Phys. Fluids **21**, 1167 (1978)

[2] T. Katsouleas, Ph.D. Thesis, 1984, UCLA

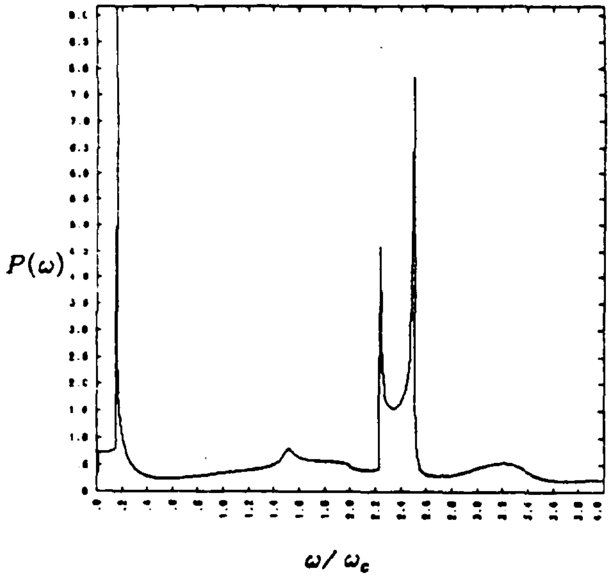

Figure 5a. Spectrum theoretical

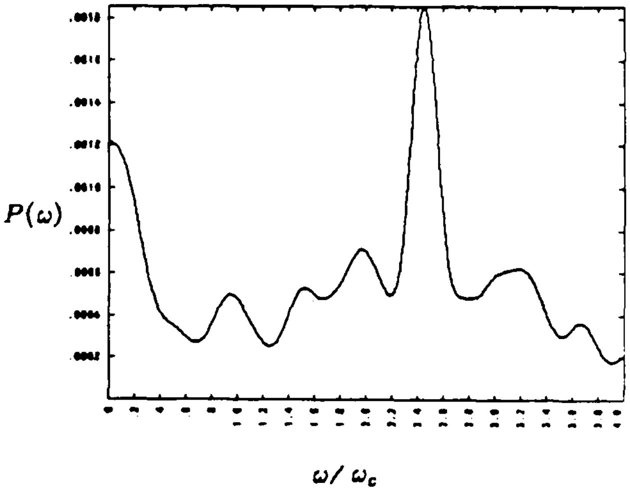

Figure 5b. Spectrum observed

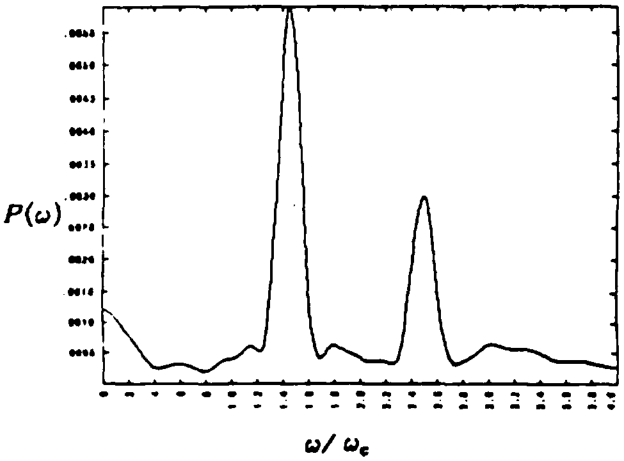

Figure 6. Spectrum with small excitation

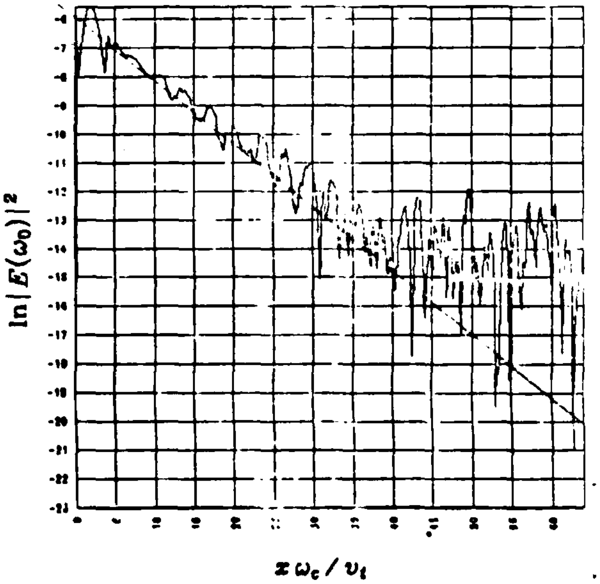

Figure 7. Excitation amplitude = 0.25

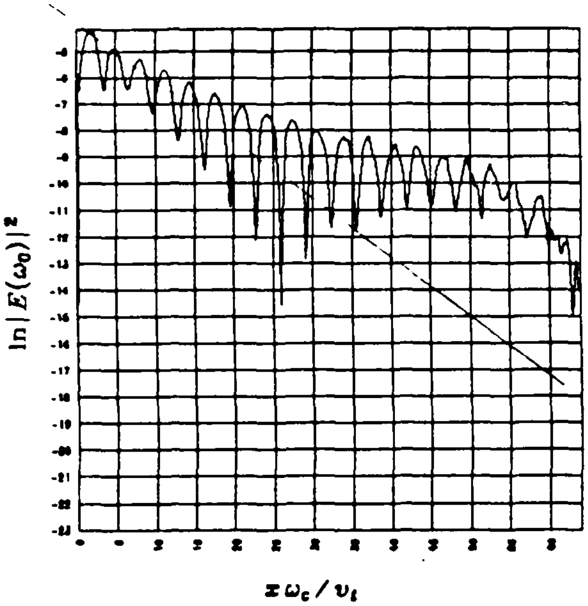

Figure 8. Excitation amplitude = 0.5

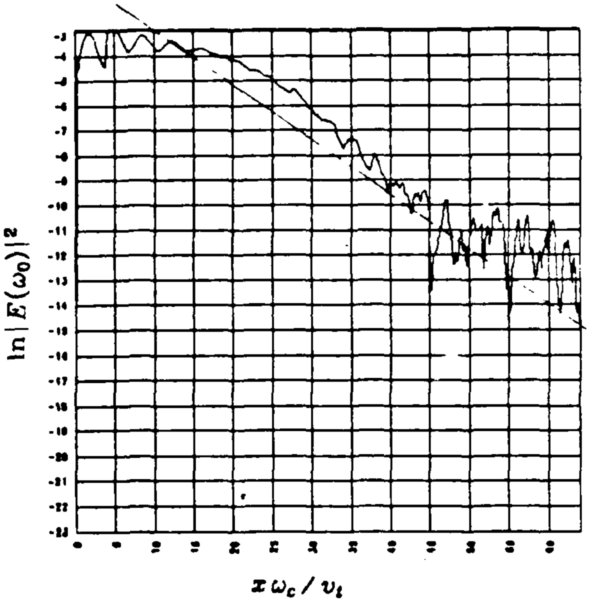

Figure 9. Excitation amplitude = 1.0

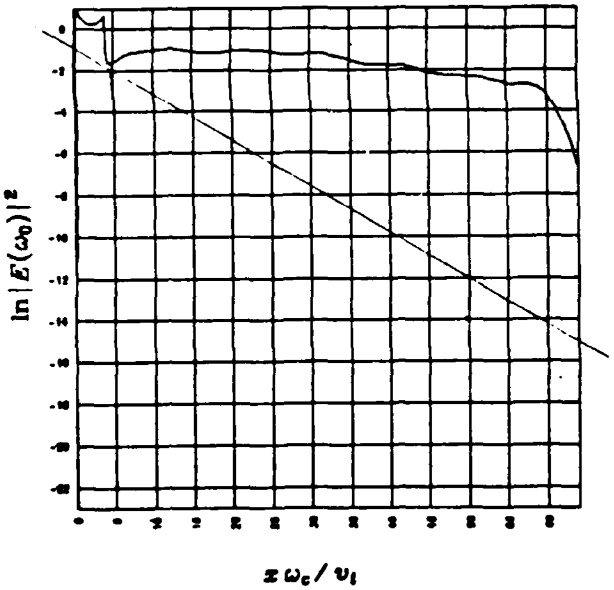

Figure 10. Excitation amplitude = 10

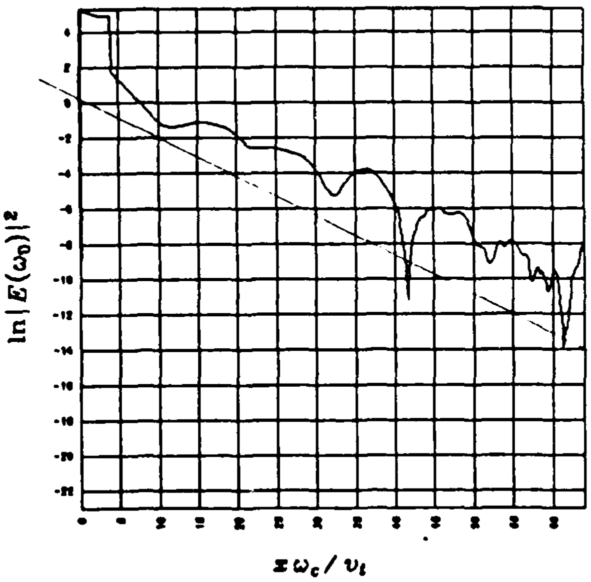

Figure 11. Excitation amplitude = 100

B. SIMULATION OF THE EFFECT OF LARGE AMPLITUDE RF WAVES ON THE INTERCHANGE INSTABILITY —SUPPORTING THEORY

Niels F. Otani (Dr. J. A. Byers and Prof. C. K. Birdsall)

I. Introduction

Recent experiments at the Phaedrus tandem mirror experiment at Wisconsin[1] have provided evidence that imposed RF waves with frequencies in the vicinity of the ion-cyclotron frequency may have a strong stabilizing effect on interchange modes in an axisymmetric plasma. In the experiments, the stabilizing properties of the RF wave were observed to change sharply at a critical frequency near the ion-cyclotron frequency, with the strong stabilizing effect evident only above the critical frequency. It was suggested[1] that the stabilizing effect may be due a ponderomotive force produced by the RF wave[2] which was counteracting the effective gravity driving the interchange instability.

In view of recent results, we have attempted to simulate some of the effects which may be contributing to the stabilization of the interchange mode in the Wisconsin experiment. The simulation code used is a modification of the 2 1/2-d quasineutral Darwin code PEPSI described in a previous report.[3]

The code simulates the x-y plane perpendicular to the magnetic field $B(x,y)\hat{\mathbf{z}}$. The RF wave propagation vector $\mathbf{k}_0(x)$, the equilibrium density $\nabla n_0(x)$ and an external gravitational field $\mathbf{g}(x)$ are all initialized to point in the $\hat{\mathbf{x}}$-direction, while a small interchange perturbation is initialized with a sinusoidal dependence in the $\hat{\mathbf{y}}$-direction. Full ion dynamics are included in the code, while $n_i = n_e$ and $\mathbf{u}_e = c\mathbf{E}\times\mathbf{B}/B^2$ are assumed for the electron density and fluid velocity respectively. A complete description of the code along with simulation results will appear later; however, individual results will be quoted here as needed.

In this report, we present supporting theory for the simulation. Appropriate fluid equations for our simulations will be derived and some of their properties demonstrated. Characteristics of the RF wave to second order in the wave amplitude will be described. Equations describing the linear behavior of the interchange mode in the presence of the RF wave are stated.

II. The Equations

The algorithm used by our simulations may be represented by the fluid equations :

$$\frac{\partial \mathbf{u}}{\partial t} + \mathbf{u}\cdot\nabla\mathbf{u} = \frac{e}{m}\left(\mathbf{E} + \frac{\mathbf{u}\times\mathbf{B}}{c}\right) + \mathbf{g}, \tag{1a}$$

$$\frac{\partial n}{\partial t} = -\nabla\cdot(n\mathbf{u}), \tag{1b}$$

$$\frac{\partial \mathbf{B}}{\partial t} = -c\nabla \times \mathbf{E}, \tag{1c}$$

$$\mathbf{E} = \left(\frac{\nabla \times \mathbf{B}}{4\pi en} - \frac{\mathbf{u}}{c}\right) \times \mathbf{B}, \tag{1d}$$

where $\mathbf{u}$ is the *ion* fluid velocity, $n = n_i = n_e$ is the density, and m is the ion mass. The form of the ion momentum equation Eq. (1a) is appropriate because all simulations to date have been initialized with cold ions. Equation (1d) comes from the zero-pressure, inertialess electron momentum equation

$$0 = \mathbf{E} + \frac{\mathbf{u}_e \times \mathbf{B}}{c}, \tag{2}$$

where for $\mathbf{u}_e$, Ampère's Law has been substituted neglecting the displacement current.

Since the simulation takes place in the x-y plane, the magnetic field need only have a z-component: $\mathbf{B} = B(x,y,t)\hat{\mathbf{z}}$. Noting also that $\mathbf{E}$ only appears in the combination $\mathbf{E} + \mathbf{u} \times \mathbf{B}/c$, Eqs. (1) may be simplified to

$$\frac{\partial \mathbf{u}}{\partial t} + \mathbf{u} \cdot \nabla \mathbf{u} = -\frac{B\nabla B}{4\pi mn} + \mathbf{g}, \tag{3a}$$

$$\frac{\partial n}{\partial t} = -\nabla \cdot (n\mathbf{u}), \tag{3b}$$

$$\frac{\partial B}{\partial t} = -\nabla \cdot (B\mathbf{u}) + \frac{cB}{4\pi e}\hat{\mathbf{z}} \cdot \nabla\left(\frac{1}{n}\right) \times \nabla B, \tag{3c}$$

where $\mathbf{u} = (u_x, u_y, 0)$. Equations (3) form the basis for all subsequent analysis in this report.

III. Properties

Several properties may be derived for the system described by Eqs. (3). A number of these properties are particularly appealing because they have a simple physical interpretation.

From Ampère's Law, the electron fluid velocity may be expressed as

$$\mathbf{u}_e = \mathbf{u} - \frac{c}{4\pi en}\nabla B \times \hat{\mathbf{z}}, \tag{4}$$

from which immediately follows $\mathbf{J} \cdot \nabla B = 0$ and $\nabla \cdot \mathbf{J} = 0$, as is also true of MHD theory. Thus the total current flows along constant-B contours and is divergence-free.

Substituting Eq. (4) into Eq. (3b) yields

$$\frac{\partial n}{\partial t} = -\nabla \cdot (n\mathbf{u}_e), \tag{5}$$

the electron continuity equation, while substitution into Eq. (3c) produces

$$\frac{\partial B}{\partial t} = -\nabla \cdot (B\mathbf{u}_e), \tag{6}$$

demonstrating conservation of magnetic flux $\int B\,dx\,dy$. Equations (3a), (4), (5), and (6) are an alternative and equivalent set of equations to Eqs. (3). The similarity of Eqs. (5) and (6) may be exploited to yield

$$\left(\frac{\partial}{\partial t} + \mathbf{u}_e \cdot \nabla\right)\left(\frac{B}{n}\right) = 0, \tag{7}$$

i.e., the ratio B/n is constant in the electron fluid frame. Thus, the magnetic field may be thought of as being frozen into the electrons.

An energy conservation theorem also exists for this system. Taking the dot product of both sides of Eq. (3a) with $mn\mathbf{u}$ produces

$$\frac{1}{2}mn\frac{\partial n^2}{\partial t} + \frac{1}{2}mn\mathbf{u}\cdot\nabla u^2 = -\frac{1}{4\pi}\mathbf{u}B\cdot\nabla B + mn\mathbf{u}\cdot\mathbf{g}. \tag{8}$$

Ampère's Law (Eq. (4)) may be used to show

$$\mathbf{u}B\cdot\nabla B = \mathbf{u}_e B\cdot\nabla B. \tag{9}$$

Multiplying both sides of Eq. (6) by B yields

$$\mathbf{u}_e B\cdot\nabla B = \frac{1}{2}\frac{\partial}{\partial t}(B^2) + \nabla\cdot(\mathbf{u}_e B^2). \tag{10}$$

Using ion continuity on the left side of Eq. (8) and substituting Eqs. (9) and (10), we obtain

$$\frac{\partial}{\partial t}\left(\frac{1}{2}nmu^2 + \frac{B^2}{8\pi} + nm\phi_g\right) + \nabla\cdot\left(\frac{1}{2}nmu^2\mathbf{u} + \frac{B^2}{4\pi}\mathbf{u}_e + nm\phi_g\mathbf{u}\right) = 0, \tag{11}$$

where $\mathbf{g} \equiv -\nabla\phi_g$. Thus the local total energy density defined as $nmu^2/2 + B^2/8\pi + nm\phi_g$ will be conserved in any region on the x-y plane up to a flux on the region boundary.

IV. The RF Wave

Estimates of the magnitudes of various quantities associated with the RF wave will be required for the stability analysis of the interchange mode when the RF wave is present. Since effects second order in the RF amplitude are expected to contribute the main stabilizing influence, calculations to that order were performed. We use the equations

$$\frac{\partial u_x}{\partial t} + u_x\frac{\partial u_x}{\partial x} = -\frac{B}{4\pi mn}\frac{\partial B}{\partial x} + g, \tag{12a}$$

$$\frac{\partial u_y}{\partial t} + u_x\frac{\partial u_y}{\partial x} = 0, \tag{12b}$$

$$\frac{\partial n}{\partial t} = -\frac{\partial}{\partial x}(nu_x), \tag{12c}$$

$$\frac{\partial B}{\partial t} = -\frac{\partial}{\partial x}(Bu_x), \tag{12d}$$

since the RF wave has been assumed to depend only on x.

Zero order. The equilibrium is assumed to be time-independent ($\partial/\partial t = 0$) with $u_x \equiv u_{x0} = 0$. Equation (12a) then implies a depression must exist in the magnetic field structure due to the gravity-induced current:

$$\frac{d}{dx}\left(\frac{B_0^2}{8\pi}\right) = mn_0 g, \tag{13}$$

while Eq. (12b) allows $u_{y0}(x)$ to be arbitrary. If we also require the electric field $\mathbf{E}_0$ to be zero in equilibrium, Eq. (1a) forces $u_{y0} = -mcg/eB_0$, the gravitational drift velocity. Equations (12c) and (12d) yield no further information.

First order. Equations (12a) through (12c) may be linearized about the equilibrium to yield a modified wave equation:

$$\frac{\partial^2}{\partial t^2}(u_{x1}B_0) = v_A^2(x)\left[\frac{1}{L_B}\left(\frac{1}{L_B} - \frac{1}{L_n}\right) + \frac{\partial^2}{\partial x^2}\right](u_{x1}B_0), \tag{14}$$

where u_{x1} is the first order component of u_x, $v_A \equiv B_0^2/(4\pi m n_0)$, $L_B^{-1} \equiv (1/B_0)(\partial B_0/\partial x)$, and $L_n^{-1} \equiv (1/n_0)(\partial n_0/\partial x)$. Equation (12d) may be linearized to yield an equation for u_{y1} which evidently plays no role in the wave mechanics.

For the remainder of this section, a uniform equilibrium ($g = 0$, $\partial n_0/\partial x = 0$) will be assumed, because as stated earlier, only estimates of the wave quantities will be required.

In a uniform system $L_B^{-1} = L_n^{-1} = 0$; thus Eq. (14) becomes simply the wave equation for the propagation of compressional Alfvén waves. If we assume a standing wave of a given frequency ω_0 (this is the type of wave initially loaded in the simulation), we find the following relative amplitudes and spatial and temporal phases among the wave components:

$$B_1 = \tilde{B}\cos k_0 x \cos\omega_0 t, \tag{15a}$$

$$n_1 = n_0\frac{\tilde{B}}{B_0}\cos k_0 x \cos\omega_0 t, \tag{15b}$$

$$u_{x1} = v_A\frac{\tilde{B}}{B_0}\sin k_0 x \sin\omega_0 t, \tag{15c}$$

$$u_{y1} = 0, \tag{15d}$$

$$E_{x1} = \frac{k_0 B_0 \tilde{B}}{4\pi e n_0}\sin k_0 x \cos\omega_0 t, \tag{15e}$$

$$E_{y1} = \frac{v_A}{c}\tilde{B}\sin k_0 x \sin\omega_0 t, \tag{15f}$$

where $k_0 \equiv \omega_0/v_A$.

Second order. When Eq.s (12a) and (12d) are expanded to second order and the uniform equilibrium assumption is again made, the result is

$$\frac{\partial^2}{\partial t^2}\left(\frac{B_2}{B_0}\right) = v_A^2\frac{\partial^2}{\partial x^2}\left(\frac{B_2}{B_0}\right) + \frac{1}{2}\omega_0^2\left(\frac{\tilde{B}}{B_0}\right)^2\cos 2k_0 x(1 - 3\cos 2\omega_0 t), \tag{16}$$

where expressions from Eqs. (15) have been used. This has a particular secular solution

$$\frac{B_2}{B_0} = \frac{1}{8}\left(\frac{\tilde{B}}{B_0}\right)^2 \cos 2k_0x(1 - 3\omega_0 t \sin 2\omega_0 t), \tag{17}$$

which has been observed in simulation. The d.c. portion of the solution is

$$\langle B_2 \rangle = \frac{1}{8}B_0\left(\frac{\tilde{B}}{B_0}\right)^2 \cos 2k_0x. \tag{18}$$

The equation corresponding to Eq. (16) may be derived for u_{x2}; it has a secular solution whose d.c. part is

$$\langle u_{x2} \rangle = 0. \tag{19}$$

The expression for $\langle B_2 \rangle$ in Eq. (18) provides some insight into the nature of the second order current. Since $\langle u_{y0} \rangle = \langle u_{ey0} \rangle = \langle u_{y1} \rangle = 0$, we have

$$-\frac{\partial \langle B_2 \rangle}{\partial x} = \frac{4\pi}{c}\langle J_{y2} \rangle = \frac{4\pi e n_0}{c}\langle u_{y2} - u_{ey2} \rangle - \frac{4\pi e}{c}\langle n_1 u_{ey1} \rangle. \tag{20}$$

The last term in Eq. (20) may be evaluated using Eqs. (15):

$$-\frac{4\pi e}{c}\langle n_1 u_{ey1} \rangle = \frac{1}{4}k_0 B_0\left(\frac{\tilde{B}}{B_0}\right)^2 \sin 2k_0x, \tag{21}$$

which we observe from Eq. (18) is equal to $-\partial\langle B_2 \rangle/\partial x$. Thus

$$\langle u_{y2} - u_{ey2} \rangle = 0, \tag{22}$$

which is somewhat of a surprise. We might have expected the second order current would be provided by a ponderomotive ion drift of the form

$$\langle u_{y2} \rangle = \frac{c\mathbf{F}_p \times \hat{\mathbf{z}}}{eB_0}, \tag{23}$$

where $\mathbf{F}_p$ is the ponderomotive force due to the RF wave; however if this is the case, it is canceled by the second order electron drift, and instead $\langle n_1 u_{ey1} \rangle$ must be considered as the important second-order current term. It is not clear whether this second-order mechanism will be of the type necessary to reverse the destabilizing gravitational current.

V. Stability of the Interchange Wave

By considering the system containing the RF wave to be a *modified* equilibrium, it is possible to investigate the stability properties of the interchange mode in the presence of the wave. Assuming the interchange perturbation to be of the form $\delta n(x,y,t) = \delta n(x,t)e^{iky}$ (similarly for $\delta\mathbf{u}$ and δB), we obtain to first order

$$\left(\frac{\partial}{\partial t} + iku_y + \frac{\partial u_x}{\partial x}\right)\delta u_x = -G\frac{\delta B}{B} + G\frac{\delta n}{n} - u_x\frac{\partial \delta u_x}{\partial x} - \frac{v_A^2}{B}\frac{\partial \delta B}{\partial x} \tag{24a}$$

$$\left(\frac{\partial}{\partial t} + iku_y\right)\delta u_y = -ikv_A^2\frac{\delta B}{B} - \frac{\partial u_y}{\partial x}\delta u_x - u_x\frac{\partial \delta u_y}{\partial x} \tag{24b}$$

$$\frac{1}{n}\left(\frac{\partial}{\partial t} + iku_y + \frac{\partial u_x}{\partial x}\right)\delta n = -\frac{1}{n}\frac{\partial n}{\partial x}\delta u_x - ik\delta u_y - \frac{\partial \delta u_x}{\partial x} - \frac{u_x}{n}\frac{\partial \delta n}{\partial x} \tag{24c}$$

$$\frac{1}{B}\left(\frac{\partial}{\partial t} + iku_y + \frac{\partial u_x}{\partial x} + \frac{ikv_A^2}{\omega_{ci}}\frac{1}{n}\frac{\partial n}{\partial x}\right)\delta B = \frac{ikG}{\omega_{ci}}\frac{\delta n}{n} - \frac{G}{v_A^2}\delta u_x - ik\delta u_y - \frac{\partial \delta u_x}{\partial x} - \frac{u_x}{B}\frac{\partial \delta B}{\partial x} \tag{24d}$$

All equilibrium quantities in Eqs. (24) contain the RF wave and therefore have both space and time dependence. Here $\omega_{ci} \equiv eB/mc$ and $G \equiv g - \partial u_x/\partial t - u_x \partial u_x/\partial x$. Equation (24) should be solvable in the local approximation using a method analogous to that used to solve Mathieu's Equation for multiply periodic solutions; this calculation is still in progress.

In the case of a vanishingly small RF wave, the assumptions $k^2 v_A^2 \ll \omega_{ci}^2$ and $\omega \ll \omega_{ci}$ in the local aproximation yield the usual interchange dispersion relation

$$\tilde{\omega}^2 + \frac{kg}{\omega_{ci}}\tilde{\omega} + \frac{g}{n_0}\frac{\partial n_0}{\partial x}\frac{\tilde{\omega}_{ci}}{\omega_{ci}} = 0 \tag{25}$$

where $\tilde{\omega} \equiv \omega - ku_{0y}$, ω is the interchange mode frequency, and $\tilde{\omega}_{ci} \equiv \omega_{ci} + \partial u_{0y}/\partial x$ is an effective ion cyclotron frequency.

VI. Conclusions

Theoretical groundwork has been laid for both the theory and simulation of the stability of the interchange mode in the presence of an RF wave. Physically intuitive properties of the simulation equations have been found. Estimates of RF wave quantities have been derived. We find that the current second-order in the RF wave flows due to an unexpected mechanism related to first order perturbations in the density and the electron fluid velocity. Finally equations linear in the interchange perturbation have been derived and are in the process of being solved.

References

[1] Ferron, J. R., N. Hershkowitz, R. A. Breun, S. N. Golovato, and R. Goulding, Phys. Rev. Lett. **51**, 1955 (1983).

[2] Dimonte, G., B. M. Lamb, and G. J. Morales, Physics of Fluids **26**, 2657 (1983).

[3] Otani, N. F. "PEPSI: A 2 1/2-Dimensional Periodic Quasineutral Darwin Simulation Code," Third and Fourth Quarter Progress Report on Plasma Theory and Simulation, July to December 1983, Electronics Research Lab., U. of Calif., Berkeley, CA 94720.

C. ONE-BEAM ALFVÉN ION-CYCLOTRON INSTABILITIES OF MULTIBEAM ION DISTRIBUTION FUNCTIONS

Niels F. Otani (Prof. C. K. Birdsall)

Tests of the simulation code TRACY used to study the Alfvén ion-cyclotron (AIC) instability have included simulations using multibeam ion distributions of the form,

$$f(\mathbf{v}) = \frac{1}{2\pi v_\perp N_b} \sum_{b=0}^{N_b-1} \delta(v_\perp - v_{\perp b})\,\delta(v_z - v_{zb}), \tag{1}$$

where N_b is the number of beams. These distributions were observed in simulation to yield growth rates very close to those expected of bimaxwellian ion distributions having the same $T_{i\parallel}$ and $T_{i\perp}$ for wavenumbers k on the principal growth peak. However, a deviation from bimaxwellian growth rates was observed for high k modes. In this article, we demonstrate that the observed deviation of the growth spectrum for high k may be explained by "one-beam" AIC instabilities. That is, for high enough k, it is possible for the ion response to be dominated by a single beam in the ion distribution function. The resonant beam has infinite temperature anisotropy and therefore is capable of driving the AIC instability.

From a form of the AIC dispersion relation derived previously,[1] we easily obtain the dispersion relation for the multibeam distribution function described by Eq. (1):

$$0 = \frac{\omega}{\Omega} + \frac{k^2 v_A^2}{\Omega^2} + \frac{1}{N_b} \sum_{b=0}^{N_b-1} \left(\frac{\omega - k v_{zb}}{\omega - k v_{zb} - \Omega} + \frac{\frac{1}{2} k^2 v_{\perp b}^2}{(\omega - k v_{zb} - \Omega)^2} \right). \tag{2}$$

We will be looking for a mode associated with a given beam, say, the beam $b = 0$ in Eq. (1). Accordingly, we rewrite Eq. (2) as

$$\begin{aligned} 0 = 1 &+ \frac{\omega_d + k v_{z0} + \Omega}{\Omega} + \frac{k^2 v_A^2}{\Omega^2} + \frac{1}{N_b} \left(\frac{\Omega}{\omega_d} + \frac{k^2 v_{\perp 0}^2}{2\omega_d^2} \right) \\ &+ \frac{1}{N_b} \sum_{b=1}^{N_b-1} \left(\frac{\Omega}{\omega_d + k(v_{z0} - v_{zb})} + \frac{\frac{1}{2} k^2 v_{\perp b}^2}{(\omega_d + k(v_{z0} - v_{zb}))^2} \right), \end{aligned} \tag{3}$$

where $\omega_d \equiv \omega - k v_{z0} - \Omega$ is the deviation of the mode frequency from the Doppler-shifted ion-cyclotron frequency. The mode will be assumed associated with the beam $b = 0$ in the sense that

$$\omega_d \equiv \omega_{d0} + \frac{\omega_{d1}}{k} + \frac{\omega_{d2}}{k^2} + O(k^{-3}) \quad \text{as} \quad k \to \infty, \tag{4}$$

where ω_{d0}, ω_{d1}, and ω_{d2} are independent of k; i.e., we are looking for roots near the resonant frequency of beam b as $k \to \infty$.

With this form of ω_d, the dispersion relation Eq. (3) may be expanded in powers of k^{-1} as

$$
\begin{aligned}
0 = &\left(\frac{k^2 v_A^2}{\Omega^2} + \frac{k^2 v_{\perp 0}^2}{2N_b \omega_{d0}^2}\right) \\
&+ \left(\frac{k v_{z0}}{\Omega} - \frac{k v_{\perp 0}^2 \omega_{d1}}{N_b \omega_{d0}^3}\right) \\
&+ \left\{2 + \frac{\omega_{d0}}{\Omega} + \frac{1}{N_b}\left(\frac{\Omega}{\omega_{d0}} + \sum_{b=1}^{N_b - 1} \frac{\frac{1}{2} v_{\perp b}^2}{(v_{z0} - v_{zb})^2}\right) - \frac{v_{\perp 0}^2}{2N_b \omega_{d0}^2}\left[\frac{2\omega_{d0}}{\omega_{d2}} - 3\left(\frac{\omega_{d1}}{\omega_{d0}}\right)^2\right]\right\} \\
&+ O(k^{-1}). \qquad (5)
\end{aligned}
$$

Solving Eq. (5) power by power in k^{-1}, we find that the k^2, k^1, and k^0 terms yield respectively,

$$\omega_{d0} = \pm \frac{i\Omega v_{\perp 0}}{\sqrt{2n_b} v_A}, \qquad (6)$$

$$\omega_{d1} = \frac{N_b v_{z0} \omega_{d0}^3}{v_{\perp 0}^2 \Omega}, \qquad (7)$$

and

$$\omega_{d2} = \frac{\omega_{d0}}{2}\left\{3\left(\frac{\omega_{d1}}{\omega_{d0}}\right)^2 + \frac{2N_b \omega_{d0}^2}{v_{\perp 0}^2}\left[2 + \frac{\omega_{d0}}{\Omega} + \frac{1}{N_b}\left(\frac{\Omega}{\omega_{d0}} + \sum_{b=1}^{N_b - 1} \frac{\frac{1}{2} v_{\perp b}^2}{(v_{z0} - v_{zb})^2}\right)\right]\right\}. \qquad (8)$$

Substituting Eq. (6) into Eqs. (7) and (8), and then substituting Eq. (7) into Eq. (8), we find

$$\frac{\omega_{d1}}{k} = \mp \frac{i\Omega}{2\sqrt{2N_b}}\left(\frac{\Omega}{k v_A}\right)\frac{v_{z0} v_{\perp 0}}{v_A^2}, \qquad (9)$$

and

$$
\begin{aligned}
\frac{\omega_{d2}}{k^2} = &\frac{\Omega v_{\perp 0}}{2\sqrt{2N_b} v_A}\left(\frac{\Omega}{k v_A}\right)^2 \left\{\frac{1}{\sqrt{N_b}}\left(\frac{v_{\perp 0}}{\sqrt{2} v_A} - \frac{\sqrt{2} v_A}{v_{\perp 0}}\right)\right. \\
&\left. \pm i\left[\frac{3}{4}\left(\frac{v_{z0}}{v_A}\right)^2 - 2 - \frac{1}{N_b}\sum_{b=1}^{N_b - 1} \frac{\frac{1}{2} v_{\perp b}^2}{(v_{z0} - v_{zb})^2}\right]\right\}. \qquad (10)
\end{aligned}
$$

Equations (6), (9), and (10) are thus the terms in Eq. (4) which described the behavior of individual beam-related modes as $k \to \infty$.

For large enough k, the ω_{d0} term dominates in Eq. (4) and we recover as the imaginary part of the frequency just the infinite-anisotropy AIC growth rate for that beam. The expression for ω_{d0} is pure imaginary, implying that the real part of the mode frequency is just the Doppler-shifted ion cyclotron frequency, $\Omega + k v_{z0}$. These being the characteristics expected of the AIC instability for an ion distribution consisting of the one beam, we conclude that for large enough k, Doppler-shifted AIC instabilities do indeed exist for the individual beams of the ion distribution.

References

[1] N. F. Otani, "Multifluid Derivation of the Alfvén Ion-Cyclotron Linear Dispersion Relation," First and Second Quarter Progress Report on Plasma Theory and Simulation, Jan. 1 to June 30, 1984, Electronics Research Lab, U. of Calif., Berkeley, CA 94720.

D. LINEAR MODE COUPLING IN SIMULATIONS OF THE ALFVÉN ION-CYCLOTRON INSTABILITY

Niels F. Otani (Prof. C. K. Birdsall)

The identical linear growth rates of the short-wavelength ($kv_A/\Omega > 1$) spatial Fourier modes observed in Alfvén ion-cyclotron (AIC) simulations (other than those involving multibeam ion distribution functions) suggest that the various wavelengths are strongly coupled. Such coupling in the linear regime only occurs when spatial non-uniformities are present in the equilibrium. In this case, the non-uniformities arise from the spatial ion-particle distribution. These non-uniformities are inevitable in warm particle simulations, since even if particles are initially loaded with regular spacing, the regularity is immediately destroyed as the simulation pushes the particles with their various zero-order velocities. There is one exception: if each velocity to be loaded is represented by a set of particles uniformly distributed throughout the simulation (i.e., a velocity beam), then clearly the uniformity of the zero-order particle distribution will be maintained. This explains why our multibeam AIC simulations do not suffer from coupled linear growth of the high-k modes.

The non-uniformity of the spatial particle distribution enters the equations through linearized source terms. In the case of our AIC simulations, the relevant term is the linearized transverse ion current. The essence of the linear coupling is thus easily understood. The linear current response of ions to a transverse wave at a given wavelength will not be entirely at that wavelength because the constituent linear particle currents are not uniformly distributed in space.

The details of this linear coupling effect may thus be formulated by examining the effect of the linear current response on the field equations. The linearized expression for the current $\mathbf{J}$ at grid-point J used in both simulation codes TRACY and PEPSI* is

$$\begin{aligned}\mathbf{J}_J(t) = \frac{n_0 e N_g}{N} \sum_i \Big[S(z_i^0(t) - z_J) \sum_s \delta \mathbf{v}_{is}(t) + S'(z_i^0(t) - z_J) \sum_s \mathbf{v}_{is}^0(t) \delta z_{is}(t) \Big] \\ + \frac{n_0 e}{B_0^2} \frac{\partial \mathbf{A}_J}{\partial t} \times \mathbf{B}_0 \qquad (1)\end{aligned}$$

where n_0 is the unperturbed density, N_g is the number of the grid-points in this periodic system, the index i refers to groups of particles with identical zero-order values of z, $v_{\parallel}$, and $v_{\perp}$, s indexes the particles in each such group, N is the total number of particles, $z_i^0(t) = z_i^0 + v_{\parallel}^0 t$, $v_{is}^0(t) = \hat{\mathbf{x}} v_{i\perp}^0 \sin(\theta_{is}^0 + \Omega t) + \hat{\mathbf{y}} v_{i\perp}^0 \cos(\theta_{is}^0 + \Omega t)$ are the zero-order trajectories, $S(z)$ is the shape factor of each particle, and z_J is the z-position of grid-point J. Here $\delta \mathbf{v}_{is}(t)$ and $\delta z_{is}(t)$ are the linear perturbed quantities for particle s in group i, $\mathbf{A}_J$ is the perturbed vector potential at grid J, $\mathbf{B}_0 = B_0 \hat{\mathbf{z}}$ is the unperturbed magnetic field which is uniform, constant in time and parallel to the grid direction, and Ω is the corresponding

---

* Note: PEPSI does not use the vector potential **A**. Thus slight errors arising from finite differencing are introduced here. These will be ignored.

ion-cyclotron frequency. Again, ions are represented as particles while electrons enter only through the electron $\mathbf{E} \times \mathbf{B}_0$ current. In this calculation we ignore the finite timestep size Δt.

Expressions for $\sum_s \delta \mathbf{v}_{is}(t)$ and $\delta z_{is}(t)$ in the ion terms in Eq. (1) may be calculated from the linearized ion equation of motion :

$$\frac{d}{dt}\delta \mathbf{v}_{is} + \mathbf{\Omega} \times \delta \mathbf{v}_{is} = \frac{e}{m}\sum_j S(z_j - z_{is}^0)\left(\delta \mathbf{E} + \frac{\mathbf{v}_{is}^0 \times \delta \mathbf{B}}{c}\right)$$
$$= -\frac{e}{mc}\sum_{j,k}\left[\left(\frac{\partial}{\partial t} + i\mathbf{k}\cdot \mathbf{v}_{is}^0(t)\right)\mathbf{A}_k - i\mathbf{k}(\mathbf{v}_{is}^0 \cdot \mathbf{A}_k)\right]e^{ikz_j} S(z_i^0(t) - z_j) \quad (2)$$

where we have rewritten $\mathbf{A}_j(t) = \sum_k \mathbf{A}_k(t)e^{ikz_j}$ in which j is a grid-point index and k assumes the values $k = 2\pi m/L$, $m = -N_g/2 + 1, \ldots, N_g/2$ and $\mathbf{k} = k\hat{\mathbf{z}}$.

Considering first the perpendicular perturbed velocity component $\delta v_{is}^+ \equiv (\delta v_{isx} + i\delta v_{isy})/\sqrt{2}$, we find

$$\left(\frac{d}{dt} + i\Omega\right)\sum_s \delta v_{is}^+ = \frac{N_s e}{mc}\sum_k\left(-\frac{\partial A_k^+}{\partial t} - ikv_{i\parallel}^0 A_k^+(t)\right)S_k N_g \exp[ik(z_i^0 + v_{i\parallel}^0 t)], \quad (3)$$

where the particle shape factor has been Fourier transformed $S(z) = \sum_{k'=-\infty}^{\infty} S_{k'}e^{ik'z}$ and grid aliasing effects have been ignored :

$$\sum_j S_{k'}e^{i(k-k')z_j} \approx S_k N_g \delta_{kk'}.$$

This is often a good approximation for wavenumbers k of interest, i.e., wavenumbers well within the first Brillouin zone $-\pi/\Delta z \ll k \ll \pi/\Delta z$; however, evidence suggests that grid aliasing is in fact important for this type of simulation. This will be amplified in future reports.

Assume now that $A_k^+(t)$ is a sum of waves,

$$A_k^+(t) = \int d\omega\, A_k^+(\omega)e^{-i\omega t}, \quad (4)$$

with the values of (complex) ω included in the sum to be specified later.

Equation (3) is easily solved for $\sum_s \delta v_{is}^+$ by multiplying by the integrating factor $e^{i\Omega t}$:

$$\frac{d}{dt}\left(e^{i\Omega t}\sum_s \delta v_{is}^+\right) = \frac{iN_s e}{mc}e^{i\Omega t}\sum_k \int d\omega\, S_k N_g(\omega - kv_{i\parallel}^0)A_k^+(\omega)\exp[ik(z_i^0 + v_{i\parallel}^0 t) - i\omega t], \quad (5a)$$

$$\sum_s \delta v_{is}^+ = \frac{N_s e}{mc}\Bigg(C_i^+ e^{-i\Omega t}$$
$$+ e^{-i\Omega t}\int^t dt' \sum_k \int d\omega\, S_k N_g i(\omega - kv_{i\parallel}^0)A_k^+(\omega)\exp[ik(z_i^0 + v_{i\parallel}^0 t') - (\omega - \Omega)t']\Bigg), \quad (5b)$$

yielding on integration,

$$\sum_s \delta v_{is}^{+} = \frac{N_s e}{mc}\left(C_i^{+} e^{i\Omega t} - \sum_k \int d\omega\, S_k N_g \frac{\omega - k v_{i\|}^0}{\omega - k v_{i\|}^0 - \Omega} A_k^{+}(\omega) \exp[ik(z_i^0 + v_{i\|}^0 t) - i\omega t]\right). \tag{5c}$$

The expression for $\delta z_{is}(t)$ is obtained by examining the parallel component of Eq. (2). Again ignoring grid aliases and using Eq. (4) we find the expression analogous to Eq. (5a):

$$\frac{d}{dt}\delta v_{is\|}(t) = \frac{e}{mc}\sum_k \int d\omega\, S_k N_g ik(\mathbf{v}_{is}^0(t)\cdot \mathbf{A}_k(\omega)) \exp[ik(z_i^0 + v_{i\|}^0 t) - i\omega t]. \tag{6}$$

Since in the $\{A_k^{+}, A_k^{-}\}$ basis,

$$\mathbf{v}_{is}^0(t)\cdot \mathbf{A}_k(\omega) = -\frac{i v_{i\perp}^0}{\sqrt{2}}\left\{A_k^{+}(\omega)\exp[i(\Omega t + \theta_{is}^0)] - A_k^{-}(\omega)\exp[-i(\Omega t + \theta_{is}^0)]\right\}, \tag{7}$$

we find upon substituting into Eq. (6)

$$\frac{d}{dt}\delta v_{is\|}(t) = \frac{e}{mc}\sum_k \int d\omega\, S_k N_g \frac{k v_{i\perp}^0}{\sqrt{2}} e^{ikz_i^0} \times \left\{A_k^{+}(\omega)e^{i\theta_{is}^0}\exp[-i(\omega - k v_{i\|}^0 - \Omega)t] - A_k^{-}(\omega)e^{-i\theta_{is}^0}\exp[-i(\omega - k v_{i\|}^0 + \Omega)t]\right\}. \tag{8a}$$

Two integrations with respect to t yield

$$\delta v_{is\|}(t) = \frac{e}{mc}\left[C_{1\|}^{is} + \sum_k \int d\omega\, S_k N_g \frac{k v_{i\perp}^0}{\sqrt{2}} e^{ikz_i^0} \times \left(A_k^{+}(\omega)e^{i\theta_{is}^0}\frac{\exp[-i(\omega - k v_{i\|}^0 - \Omega)t]}{-i(\omega - k v_{i\|}^0 - \Omega)} - A_k^{-}(\omega)e^{-i\theta_{is}^0}\frac{\exp[-i(\omega - k v_{i\|}^0 + \Omega)t]}{-i(\omega - k v_{i\|}^0 + \Omega)}\right)\right], \tag{8b}$$

and

$$\delta z_{is}(t) = \frac{e}{mc}\left[C_{2\|}^{is} + C_{1\|}^{is} t - \sum_k \int d\omega\, S_k N_g \frac{k v_{i\perp}^0}{\sqrt{2}} e^{ikz_i^0} \times \left(A_k^{+}(\omega)e^{i\theta_{is}^0}\frac{\exp[-i(\omega - k v_{i\|}^0 - \Omega)t]}{(\omega - k v_{i\|}^0 - \Omega)^2} - A_k^{-}(\omega)e^{-i\theta_{is}^0}\frac{\exp[-i(\omega - k v_{i\|}^0 + \Omega)t]}{(\omega - k v_{i\|}^0 + \Omega)^2}\right)\right]. \tag{8c}$$

The (+)-polarization portion of the $\delta z_{is}(t)$ term in Eq. (1) may now be evaluated:

$$\hat{\mathbf{x}}^{-}\cdot \sum_s \mathbf{v}_{is\perp}^0(t)\delta z_{is}(t) = \sum_s \frac{i v_{i\perp}^0}{\sqrt{2}} e^{-i\theta_{is}^0} e^{-i\Omega t}\delta z_{is}(t). \tag{9a}$$

Here $\hat{\mathbf{x}}^{-} = (\hat{\mathbf{x}}^{+})^{*} = \hat{\mathbf{x}} + i\hat{\mathbf{y}}$ is the dual basis vector to $\hat{\mathbf{x}}^{+} \equiv \hat{\mathbf{x}} - i\hat{\mathbf{y}}$. Now assuming the particles in each group i are uniformly loaded in gyrophase space with at least three particles (the four-spokes distributions used in our simulations have four uniformly loaded particles per group) then

$$\sum_{s=1}^{N_s} e^{-2i\theta_{is}^0} = 0$$

kills the last term in Eq. (8c) when substituted into Eq. (9a). Thus we obtain

$$\begin{aligned}\hat{\mathbf{x}}^- \cdot \sum_s \mathbf{v}_{is\perp}^0(t)\delta z_{is}(t) &= \frac{N_s e}{mc}\Big(C_{2\|}^i e^{-i\Omega t} + C_{1\|}^i t e^{-i\Omega t} \\ &- \sum_k \int d\omega\, S_k N_g \frac{k(v_{i\perp}^0)^2}{2} \frac{i}{(\omega - k v_{i\|}^0 - \Omega)^2} A_k^+(\omega) \exp[ik(z_i^0 + v_{i\|}^0 t) - i\omega t]\Big). \qquad (9b)\end{aligned}$$

Finally, the $\mathbf{E} \times \mathbf{B}$ term from Eq. (1) may be evaluated as

$$\hat{\mathbf{x}}^- \cdot \frac{\partial \mathbf{A}_J}{\partial t} \times \mathbf{B}_0 = -\sum_k \int d\omega\, \omega B_0 A_k^+(\omega) \exp(ikz_J - i\omega t). \qquad (10)$$

Substituting Eqs. (5c), (9b), and (10) into Eq. (1), we obtain for the linearized current,

$$\begin{aligned}J_J^+(t) &= \frac{n_0 e^2}{mc}\frac{N_s N_g}{N} \sum_i \sum_\kappa S_\kappa \exp[-i\kappa(z_i^0 + v_{i\|}^0 t - z_J)]\Big[(C_1^i + C_2^i t)e^{-i\Omega t} \\ &- \sum_k \int d\omega\, S_k N_g A_k^+(\omega) \exp[ik(z_i^0 + v_{i\|}^0 t) - i\omega t]\left(\frac{\omega - k v_{i\|}^0}{\omega - k v_{i\|}^0 - \Omega} + \frac{\frac{1}{2}\kappa k (v_{i\perp}^0)^2}{(\omega - k v_{i\|} - \Omega)^2}\right)\Big] \\ &- \frac{n_0 e}{B_0} \sum_k \int d\omega\, \omega A_k^+(\omega) \exp(ikz_J - i\omega t), \qquad (11)\end{aligned}$$

where the even symmetry of S, $S_k = S_{-k}$, has been used. Here constants have been absorbed as needed into the constants of integration C_1^i and C_2^i. Ignoring aliases again and using the fact that the initial value terms $(C_1^i + C_2^i t)e^{-i\Omega t}$ will eventually be dominated by terms proportional to $e^{-i\omega t}$, $\mathrm{Im}(\omega) > 0$, we obtain from Ampère's Law

$$\begin{aligned}&\int d\omega'\, D^+(k', \omega') A_{k'}^+(\omega') e^{-i\omega' t} = \\ &\left(\frac{N}{N_s}\right)^{-1} \sum_i \sum_{k \neq k'} \int d\omega\, D^+(k, \omega, k', \mathbf{v}_i^0) A_k^+(\omega) e^{-i(k'-k)z_i^0} \exp[-i(\omega - (k - k')v_{i\|}^0)t]. \qquad (12)\end{aligned}$$

Here,

$$\begin{aligned}&D^+(k', \omega') \equiv \\ &\quad \frac{k'^2 v_A^2}{\Omega^2} + \frac{\omega'}{\Omega} + \left(\frac{N}{N_s}\right)^{-1} \sum_i S_{k'}^2 N_g^2 \left(\frac{\omega' - k' v_{i\|}^0}{\omega' - k' v_{i\|} - \Omega} + \frac{\frac{1}{2}k'^2 (v_{i\perp}^0)^2}{(\omega' - k' v_{i\|} - \Omega)^2}\right), \qquad (13a)\end{aligned}$$

is the linear dispersion function that would result if each of the particles were spread uniformly in physical space, and

$$D^{+}(k,\omega;k',\mathbf{v}_i^0) \equiv -S_k S_{k'} N_g^2 \left(\frac{\omega - k v_{i\parallel}^0}{\omega - k v_{i\parallel}^0 - \Omega} + \frac{\frac{1}{2} k k' (v_{i\perp}^0)^2}{(\omega - k v_{i\parallel}^0 - \Omega)^2} \right), \tag{13b}$$

is the linear coupling coefficient for coupling from wavenumber k and frequency ω to wavenumber k' due to scattering off particle group i. Note that the complex exponential in Eq. (12) forces the scattered frequency to be $\omega' = \omega - (k - k')v_{i\parallel}^0$.

The coupling process may be diagnosed by formally expanding Eq. (12) in orders of $(N/N_s)^{-1}$. (The actual expansion parameter is not in general $(N/N_s)^{-1}$ but depends on the statistics of how the particles were loaded. For example, if the particles were randomly loaded, the expansion parameter may be expected to be of the form a constant times $(N/N_s)^{-1/2}$. The constant will usually be appreciably greater than one, since typically the resonant particles dominate the sum over i in Eq. (12) and thus effectively prevent the larger number of non-resonant particles from contributing to the statistics.)

The effect is most clearly illustrated by considering the coupling from a single "pump" wave with designated wavenumber and frequency k_0 and ω_0. The only equation that survives to zero-order in $(N/N_s)^{-1}$ is the k_0 component of Eq. (12):

$$D^{+}(k_0,\omega_0)A_{k_0}(\omega_0) = 0 \tag{14a}$$

which just indicates the pump wave must satisfy the uniform, linear dispersion relation to zero-order. The $k' \neq k$ equations (coupling equations) first appear at first order:

$$\sum_{\omega'} D^{+}(k',\omega')A_{k'}^{+}(\omega')e^{-i\omega' t} =$$

$$\left(\frac{N}{N_s}\right)^{-1} \sum_{i} D^{+}(k_0,\omega_0;k',\mathbf{v}_i^0)A_{k_0}^{+}(\omega_0)e^{-i(k'-k_0)z_i^0} \exp[-i(\omega_0 - (k_0 - k')v_{i\parallel}^0)t]. \tag{14b}$$

There is thus one scattered wave for each group of particles having amplitude

$$A_{k'}^{+}(\omega'_{ik'}) = \left(\frac{N}{N_s}\right)^{-1} \frac{D^{+}(k_0,\omega_0;k',\mathbf{v}_i^0)}{D^{+}(k',\omega'_{ik'})} e^{-i(k'-k_0)z_i^0} A_{k_0}^{+}(\omega_0), \tag{15}$$

and scattered frequency

$$\omega'_{ik'} \equiv \omega_0 - (k_0 - k')v_{i\parallel}^0. \tag{16}$$

Equations (14b) and (15) and definitional Eqs. (13a), (13b), and (16) serve to characterize the linear mode coupling process in one-dimensional AIC simulations.

Observe first the complex exponential factor involving the unperturbed particle group positions z_i^0 in Eq. (14b). When the particle group positions may be considered to obey random statistics, the presence of this factor causes the right-hand side of Eq. (14b) to scale as the square root of the number of groups $((N/N_s)^{1/2})$ as suggested above. In contrast, suppose that each loaded unperturbed velocity $\mathbf{v}^0$ is represented by particle groups $i_1,\ldots,i_p,\ldots,i_P$, i.e., $\mathbf{v}_{i_1}^0 = \ldots = \mathbf{v}_{i_p}^0 = \mathbf{v}^0$ which are uniformly loaded as $z_{i_p} = L_z p/P +$

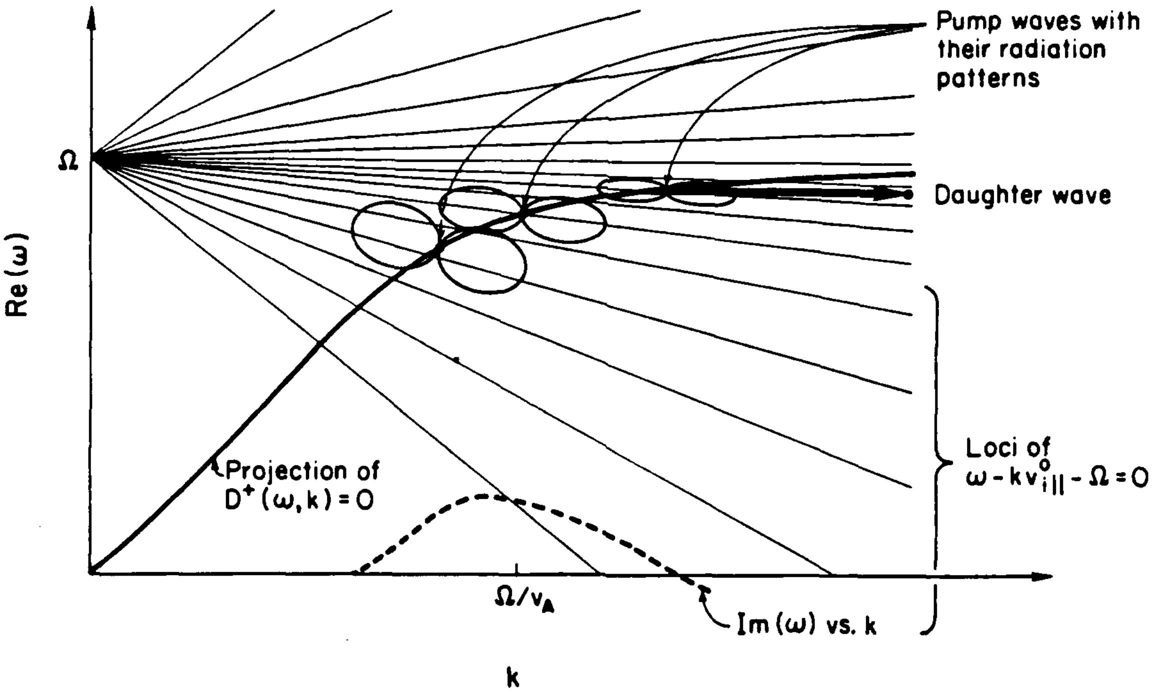

FIG. 1. Linear scattering characteristics of AIC simulations in $(\mathrm{Re}(\omega), k)$ space. Scattering occurs along fan lines emanating from the point $(\Omega, 0)$. The slopes of the fan lines correspond to the parallel velocities present in the ion distribution function. Radiation patterns are shown schematically for the most effective pump waves, i.e., those with the largest growth rates $\mathrm{Im}(\omega)$. An example of linear scattering is depicted by the heavy arrow. Note that (1) scattering is from a mode for which $D^+(\omega, k) \approx 0$ and $\mathrm{Im}(\omega)$ is large, (2) scattering is along a fan line, and (3) (ω', k') of the scattered wave lies near the locus of $D^+(\omega, k) = 0$.

const. in the periodic simulation system (length L_z). Then for any pump wave (ω_0, k_0) and any other wavenumber k', the sum in Eq. (14b) may be broken up into sub-sums each involving a single value of $\mathbf{v}^0$ which then reduces to the simple sum $\sum_{i_p} \exp[-i(k' - k)z^0_{i_p}]$. This sum always vanishes when enough particle groups are loaded per loaded velocity $\mathbf{v}^0$ so that $|k' - k_0|L_z < 2\pi P$ for the maximum wavenumber difference $|k' - k_0|$ allowed by the simulation. When the number of groups is not large enough, mode-coupling has been observed for wavenumbers for which the inequality is not satisfied. Details of this observation will appear in future reports.

We next turn to the coupling coefficients $D^+(k_0, \omega_0, k', \mathbf{v}^0_i)/D^+(k', \omega')$ as they appear in Eq. (15). Clearly the coupling will be most important between those modes and wavelengths for which $|D^+(k_0, \omega_0, k', \mathbf{v}_i^0)|$ is large while $|D^+(k', \omega'_{ik})|$ is small. From Eq. (13b), we observe that the former condition is most easily achieved for pump waves which can resonate with some portion of the ion distribution function (i.e., $\omega_0 - kv_{i\parallel}^0 - \Omega \approx 0$), while the latter condition simply requires that the scattered wave be of wavenumber and frequency close to an eigenmode of the corresponding uniform system described by $D^+(k', \omega') \approx 0$. Figure 1 illustrates the consequences of these two conditions. The fan of lines emanating from $(\Omega, k = 0)$ represent the locus of points in $(\mathrm{Re}(\omega), k)$ space which are in resonance with some particle group in the ion distribution function. There is one line for each value of $v_{i\parallel}^0$ present in the distribution. The fan spreads out as the parallel ion beta parameter is increased, with the line representing the parallel thermal velocity (for a bimaxwellian distribution) intersecting $k = \Omega/v_A$ when $\beta_{i\parallel} \approx 1$. For $\beta_{i\parallel} \lesssim 1$, the uniform system dispersion curve $D^+(k_0, \omega_0) = 0$ enters the thick of the fan of lines when $k_0 > \Omega/v_A$. Thus the most effective pump waves for linear mode coupling may be expected to be those modes which are both growing with significant growth rate (since the coupling also depends on the amplitude of the wave through the factor $e^{\mathrm{Im}(\omega)t}$) and have $k_0 > \Omega/v_A$. The finite $e^{\mathrm{Im}(\omega)t}$ also serves to smear out the resonance lines in the fan. The dispersion curve may be thought to lie above the $(\mathrm{Re}(\omega), k)$ plane for $\mathrm{Im}(\omega) > 0$ or below it for $\mathrm{Im}(\omega) < 0$, where the third dimension corresponds to $\mathrm{Im}(\omega)$. The coupled modes that these pump waves will drive most strongly may be determined from the wave-particle scattering relation Eq. (16). Since the line connecting $(\Omega, 0)$ and pump wave (ω_0, k_0) has slope $v_{i\parallel}^0$ which also appears in Eq. (16), coupling from the corresponding pump wave would expected to be strongest to modes along this line. More precisely, since the effective pump waves typically have finite $\mathrm{Im}(\omega_0)$, there will be strong coupling to any available modes in some spread about the line. Each effective pump wave may be thought to be a transmitter in $(\mathrm{Re}(\omega), k)$ space transmitting with frequency $\mathrm{Re}(\omega)$ all over (ω, k)-land with some radiation pattern determined by the details of Eq. (13b) and the magnitude of $\mathrm{Im}(\omega_0)$. The radiation patterns of the effective pump waves are shown schmatically in Fig. 1.

The best "receivers" (i.e., (ω', k') of the scattered wave) clearly lie to the high-k side of each pump wave, as illustrated in Fig. 1. Here the receivers are more in line with the peak of the pump waves' radiation peaks. Also note that the higher-k pump waves have radiation patterns which tend to line up more closely with the slope of the dispersion relation, implying that the more k is increased the tighter the coupling becomes. This effect is augmented by the presence of the factor kk' in the last term in Eq. (13b).

We conclude then that linear mode coupling due to the discreteness of simulation particles primarily concerns those wavenumbers for which roughly $k > \Omega/v_A$. The primary pump waves are those which both satisfy this condition and have significant growth rates. The most strongly scattered waves reside to the high-k side of the pump waves which spawn them. The higher k modes are tightly coupled and become more and more tightly coupled as k is increased. In stark contrast, the lower k modes ($k < \Omega/v_A$) are outside both the fan of Doppler-shifted cyclotron resonances and the radiation patterns of the active pump waves and so do not participate in linear mode coupling. All of these conclusions are consistent with simulation results obtained so far.

E. A Model of the Plasma-Sheath Region Including Ion Reflection

Lou Ann Schwager (Prof. C. K. Birdsall)

I. Introduction

Ion reflection at the collector plate affects the electrostatic potential and transport of the incident plasma. Present simulation studies indicate that increasing ion reflection increases the electrostatic potential drop across the sheath region. We also derive theories for the dependence of potential on reflection coefficient R for cold and warm ions. Simulation results compare well with theory for small R at the ion to electron mass ratio of 40. For large R the magnitude of potential drop from the computer simulation increases beyond the theoretical value. Also the oscillation amplitude widens. As we observe in the phase space plots, ion-ion two-streaming causes an instability which generates large amplitude oscillations in potential. Hence we also derive a dispersion relation for this two-streaming.

II. Simulation Model

The computer code **PDW1** models this interaction. The system model is shown in Fig. 1. This differs from the model in the previous report (QPR I,II 1984). Presently the plasma source, at the left boundary, is at the reference potential. The plate or wall, at the right boundary, floats to the wall potential ϕ_w. The plate current sums to zero. Previously the plate was at the reference potential. Also presently the velocity distribution of the reflected ions at the plate matches that of the incident ions (specular reflection). Earlier the user specified the value of the constant, "reflected" ion flux. The present model causes all reflected ions to return to the plasma because they have sufficient energy from the incident, accelerated ions to overcome the sheath potential. Previously with a half-Maxwellian, "re-emitted" flux, some ions could not overcome the barrier and so returned to the wall. Electrons reaching the plate are absorbed. The phase space plots in both cases clearly indicate this effect. As before, ions and electrons returning to the source are thermalized and re-injected (refluxed) with the input flux. We have chosen a mass ratio of 40 for $R=0$, 22, 44, 67, and 89%. *

As indicated in the previous report, for a hydrogen plasma with temperatures of 30 – 100 *eV* incident on molybdenum, particle reflection coefficients vary from 60% to 80%. Reflected ions account for only 10-15% of the reflected flux. Neutrals fill in the remainder.[1] The velocity of reflected particles depends upon the relative mass ratio of the incident ions and target atoms. The ratio of reflected to incident velocities typically is about 90%. We chose to simulate the wide range of R to fully understand the effect of ion reflection on potential.

III. Time-Independent Analysis

A. Theory

The theory for the dependence of potential drop on ion reflection for cold ions is as follows. Consider an infinite wall with floating potential (an open external circuit) at $x=0$ in contact with a plasma at $x>0$. Poisson's equation describes the electrostatic potential:

$$\frac{d^2\phi}{dx^2} = \frac{e}{\epsilon_0}(n_e - n_i - n_r) \tag{1}$$

with

$$\phi(\infty) = 0$$

where n_e and n_i are the densities of plasma electrons and ions and n_r is the density of reflected ions. Charge neutrality occurs as $x \rightarrow \infty$, thus

$$n_e(\infty) = n_i(\infty) + n_r(\infty) = n_\infty. \tag{2}$$

---

* Originally $R=20$, 40, 60, and 80% was input but a counting error generated the actual numbers given above.

Plasma electrons have a Maxwellian velocity distribution with temperature T. Their density is

$$n_e(x) = n_\infty \exp[e\phi(x)/kT]. \tag{3}$$

The plasma ions are cold and arrive at the sheath edge with an energy of $E = \frac{1}{2}Mv_{i\infty}^2$. Because all these ions entering the sheath fall freely to the wall, continuity of particles and conservation of energy determines their density:

$$n_i(x) = n_{i\infty}E^{1/2}[E - e\phi(x)]^{-1/2}. \tag{4}$$

The current of reflected ions depends on the incident current at the wall by the coefficient,

$$R \equiv -J_{r0}/J_{i0}. \tag{5}$$

We assume these reflected ions leave with the incident velocity of

$$v_{r0} = -v_{i0}. \tag{6}$$

No net current flows to the wall, thus

$$J_{e0} + J_{i0} + J_{r0} = 0. \tag{7}$$

From the conservation of energy for reflected ions and Eq. (6), we have that

$$v_r^2 = 2/M(E - e\phi). \tag{8}$$

The reflected flux is constant in x. With this and Eqs. (5) and (7), the reflected ion density becomes

$$n_r = \frac{-J_{e0}}{ev_r}\left(\frac{R}{1-R}\right). \tag{9}$$

We then substitute Eq. (8) into Eq. (9) to determine that

$$n_r = \left(\frac{-J_{e0}}{e}\right)\left(\frac{R}{1-R}\right)\left[\frac{2}{M}(E - e\phi)\right]^{-1/2}. \tag{10}$$

Because only the fastest electrons leaving the plasma source arrive at the wall, the electron density current becomes

$$J_{e0} = -en_\infty (m/2\pi kT)^{1/2} \int_{v_{min}}^{\infty} v \exp(-mv^2/2kT)dv \tag{11}$$

where $v^2{}_{min} = -2e\phi_0/m$, by conservation of energy. Integrating we find that

$$-J_{e0}/e = n_\infty \exp(\psi_0)(kT/2\pi m)^{1/2} \tag{12}$$

where $\psi = e\phi/kT$. We substitute this into Eq. (10) to solve for reflected ion density,

$$n_r = n_\infty \exp(\psi_0)\left(\frac{kT\,M}{4\pi m}\right)^{1/2}(E - e\phi)^{-1/2}\frac{R}{1-R}. \tag{13}$$

We find the incident ion density in combining Eqs. (2) and (4). Next we substitute the value for $n_{r\infty}$ which is found in letting $\phi \to 0$ in Eq. (13). Thus

$$n_i = n_\infty (E - e\phi)^{-1/2}\left[E^{1/2} - \exp(\psi_0)\left(\frac{R}{1-R}\right)\left(\frac{kT\,M}{4\pi m}\right)^{1/2}\right]. \tag{14}$$

The three densities, in Eqs. (3), (13), and (14), are then placed in Poisson's equation (Eq. (1)),

$$\frac{\epsilon_0}{en_\infty}\frac{d^2\phi}{dx^2} = \exp(\psi) - E^{1/2}(E - e\phi)^{-1/2}. \tag{15}$$

At the plasma source where $x \to \infty$, then $\phi \to 0$ and $-d\phi/dx \to 0$ because of charge neutrality. We then investigate the behavior of Eq. (15) as $x \to 0$. Multiplying by $d\phi/dx$ and integrating from ∞ to x gives

$$\frac{\epsilon_0}{kT\,n_\infty}\left(\frac{d\phi}{dx}\right)^2 = \exp(\psi) - 1 + \frac{2E}{kT}\left[\left(1 - \frac{e\phi}{E}\right)^{1/2} - 1\right]. \tag{16}$$

Expanding $e\phi/kT$ and $e\phi/E$ in a Taylor series and retaining the first three terms determines that

$$\frac{\epsilon_0}{kT\,n_\infty}\left(\frac{d\phi}{dx}\right)^2 \approx \frac{1}{2}\psi^2 - \frac{1}{4}\frac{\psi e\phi}{E}. \tag{17}$$

As $x \rightarrow \infty$ then the electric field is always positive and approaches zero. Hence $(d\phi/dx)^2 \geq 0$ which when applied to Eq. (17) implies that as $x \rightarrow \infty$

$$E \geq kT/2. \tag{18}$$

This is also the Bohm condition for an absorbing wall.

We next find the dependence of potential on R. Re-arranging the zero wall current condition and using Eq. (12) for electron current density at the wall, gives

$$(1-R)J_{i0} = en_\infty \exp(\psi_0)\left(\frac{kT}{2\pi m}\right)^{1/2}. \tag{19}$$

By continuity, ion current into the wall equals that leaving the plasma source. We find this current density J_{i0} in using $v_{i\infty}^2 = 2E/M$ and Eq. (14) with $\phi \rightarrow 0$. This current density is substituted into Eq. (19) which we manipulate to obtain

$$\exp(-\psi_0) = \left(\frac{1+R}{1-R}\right)\left(\frac{M\,kT}{m4\pi E}\right)^{1/2}. \tag{20}$$

Using $E \geq kT/2$ derives

$$-\frac{e\phi_0}{kT} = \ln\left[\left(\frac{1+R}{1-R}\right)\left(\frac{M}{2\pi m}\right)^{1/2}\right]. \tag{21}$$

The effect of reflected ions on the heat insulating ability of the sheath is evaluated by calculating the net energy flux Q at the wall. Each incident electron, which has a speed of $\langle v\rangle = (2kT/\pi m)^{1/2}$, carries an energy of $2kT$ to the wall by thermal effusion. [See Appendix for derivation of thermal effusion.] The incident electron density is one-half of

n_{e0}. An incident ion brings in the same energy as a reflected one removes. This energy is $(E - e\phi_0)$. The kinetic energy flux to the wall becomes

$$Q = \frac{1}{2} n_{e0} \langle v \rangle (2kT) + n_{i0} v_{i0} (E - e\phi_0) - n_{r0} v_{r0} (E - e\phi_0)$$

or

$$Q = \frac{1}{2} n_\infty \exp(\psi_0) \left(\frac{2kT}{\pi m}\right)^{1/2} (2kT + E - e\phi_0). \tag{22}$$

The electron free-flow energy flux is

$$Q_{free} = \frac{1}{2} n_\infty \left(\frac{2kT}{\pi m}\right)^{1/2} 2kT. \tag{23}$$

Thus

$$Q = Q_{free} * G(R) \tag{24}$$

where

$$G(R) = \frac{1}{2} \exp(\psi_0) \left(2 + \frac{E}{kT} - \psi_0\right).$$

We use our previous results from Eqs. (18) ($E = kT/2$) and (21) to see the dependence of G on R. For a hydrogen plasma interacting with a purely absorbing wall then $G(0) = 0.156$. For a low temperature plasma with a metal collector plate $R_{max} \approx 0.12$ (Reflected ions are 15% of the reflected particles which are 80% of the incident ions.) Then $G(0.12) = 0.128$. Hence ion reflection improves the thermal insulating effect of the sheath at most by 18%. If some material were found to have an ion reflection coefficient of 50%, then the thermal insulating effect would be improved by 60%.

We also derive the dependence of potential drop on reflection coefficient when the ions are warm and the ion and electron temperatures are equal. The model follows the previous derivation for cold ions. The electrons, primary ions, and reflected ions have a Maxwellian velocity distribution with temperature T at the plasma source. Here charge neutrality also applies (Eq. (2)). At the wall the reflected ion current depends on R and the incident velocity (Eqs. (5) and (6)). The wall current sums to zero (Eq. (7)). The electron wall current density is specified with Eq. (12). We assume that all ions emitted at the source reach the wall. Similarly all ions reflected from the wall arrive at the source. Hence

$$J_{i0} = en_{i\infty}\left(\frac{kT}{2\pi M}\right)^{1/2} \tag{25}$$

and

$$J_{r0} = en_{r\infty}\left(\frac{kT}{2\pi M}\right)^{1/2}. \tag{26}$$

Substituting Eq. (25) into the current balance of Eq. (19) yields

$$n_{\infty}\,\exp(\psi_0)\,(M/m)^{1/2} = (1-R)n_{i\infty}. \tag{27}$$

By the definition of R, charge neutrality, and Eqs. (25) and (26) then

$$n_{\infty} = n_{i\infty}(1+R). \tag{28}$$

The dependence of ϕ_0 on R is found when we substitute Eq. (28) into Eq. (27):

$$-\frac{e\phi_0}{kT} = \ln\left[\frac{1+R}{1-R}\left(\frac{M}{m}\right)^{1/2}\right]. \tag{29}$$

B. Results

We graph both results (Eqs. (21) and (29)) and compare these with simulation in Fig. 2. The simulation uses a plasma source of Maxwellian ions and electrons at equal temperatures. The source sheath accelerates ions above the sound speed. Thus after this acceleration into the central region, where charge neutrality results, the ion temperature is 1.5 to 2 times less than the electron temperature. This was also observed in the phase space plots of the previous QPR for a purely, absorbing wall. Thus simulation results for ϕ_w fall between the two theories but much closer to the cold ion derivation.

Note also that beyond 22% the amplitude of oscillation increases considerably. The history of wall potential for $R = 22$, 44, 67, and 89% is shown in Figs. 3 and 4. (The previous QPR shows potential history at $R = 0\%$.) As R increases, the onset of large amplitude oscillations occurs earlier in time. Also the amplitude relative to time-averaged potential increases. The reason for this is seen in the phase space plots.

For $R = 22\%$ at a time of 125, phase space plots for ions and electrons and potential profile are in Fig. 5. The electrons have a quiet, cutoff Maxwellian distribution. The ions stream with a thermal spread and follow the potential profile. Note that a few ions have fallen below the sharp edge velocity. This indicates a time-dependent interaction of the ion streams. At a later time the beam velocity of each stream has fallen to the ion sound speed, defined as $v_S = v_{te}(m_i/m_e)^{\frac{1}{2}}$. This phase space configuration shown has been constant for the last 20% of the simulation.

For $R = 89\%$, the phase space and potential plots at times of 25, 37.5, and 100 in Figs. 6, 7, and 8 indicate a strong interaction. In Fig. 6 the ion streams begin to pinch together., presumably in some form of two-stream interaction. Later in Fig. 7 vortices have evolved. Finally in Fig. 8 the streams have collapsed and have reached a new equilibrium. In each case the electrons appear to play no role in the interaction. Also at a time of 100 the number of particles is still increasing.

IV. Time-Dependent Analysis

A. Theory

We gain a better understanding of the ion-ion two-streaming in solving its dispersion relation. Assume that two opposing ion streams exist far from a wall. The primary stream has a current density of $en_{i_p}v_0$. The reflected stream has a current density of $-en_{i_r}v_0$. In one dimension with the previous definition for reflection coefficient R and continuity then

$$R = n_{i_r}/n_{i_p}. \tag{30}$$

By charge neutrality the total ion density equates with the electron density n_0 so that

$$n_{ip} = n_0/(1+R) \tag{31}$$

$$n_{ir} = n_0/[R/(1+R)]. \tag{32}$$

Both species of ions are cold. Plasma electrons have a Maxwellian velocity distribution with temperature T.

The subsequent derivation follows that illustrated in Chen for the electron two-stream instability.[2] We look for electrostatic waves with solution

$$\vec{E}_1 = E\, e^{i(\kappa x - \omega t)} \hat{x}$$

with $\hat{x}$ along $\vec{v}_0$ and $\vec{\kappa}$. Next linearize the equation of motion for the ions and arrive at the perturbed velocity for each stream.

$$\vec{v}_{1\alpha} = \frac{ieE}{M}\left(\frac{1}{\omega - \kappa v_\alpha}\right)\hat{x} \qquad \alpha = p, r \tag{33}$$

The linearized continuity equation for the ions gives the perturbed density

$$n_{1\alpha} = \kappa n_\alpha v_{1\alpha}/(\omega - \kappa v_\alpha) \qquad \alpha = p, r \tag{34}$$

The Boltzmann electrons have density

$$n_{1e} = e n_0 \phi_1/kT \tag{35}$$

where

$$E = -i\kappa\phi_1. \tag{36}$$

We then substitute Eq. (33) into (34) and Eqs. (34), (35), and (36) into the linearized Poisson's equation,

$$i\kappa E = \frac{e}{\epsilon_0}(n_{1r} + n_{1p} - n_{1e}). \tag{37}$$

The resultant dispersion relation is

$$1+\kappa^2\lambda_D^2=\frac{\kappa^2 v_S^2}{1+R}\left[\frac{1}{(\omega-\kappa v_0)^2}+\frac{R}{(\omega+\kappa v_0)^2}\right] \tag{38}$$

where

$$v_S^2=kT/M$$

and

$$\lambda_D^2=\epsilon kT/q^2 n_0.$$

Note that we recover the dispersion relation for ion acoustic waves when $v_0=0$ and $R=0$.

Consider the form of Eq. (38) as $R=0$. This equation becomes quadratic in ω^2, which gives either four real or two imaginary and two real solutions for each real κ. Thus the value of κ for marginal stability occurs where $\omega=0$. Equation (38) then yields, for $R\approx 1$,

$$1+\kappa^2\lambda_D^2\approx v_S^2/v_0^2.$$

Thus for small κ, such that $\kappa\lambda_D \ll 1$, then

$$v_S \gtrsim v_0.$$

B. Results

We observe the change in instability growth as v_0 and v_S change their relative values in time. Early in our simulations, $v_0>3v_S$. Ion velocity then approaches v_S within the time required for a thermal ion to travel to and from the wall. This time is $2L/v_{ti}=4/.158=25$. For each value of R, the ion streams begin to pinch when $v_0\approx v_S$. For $R=89\%$, Figs. 9A and 9B show the histories of electron thermal velocity and of ion beam velocity. Simulation values just before and after the time when $v_0\approx v_S$ are substituted into Eq. (38). Figures

10A, 10B, and 10C illustrate the solution with these values. For $v_0 > v_S$ only real roots exist. For $v_0 < v_S$ solutions with imaginary ω emerge indicating growth of the instability. Observe the pinching of the streams in Fig. 8B where $v_0 < v_S$. Thus Eq. (36) crudely models the two-streaming we observe by predicting the initiation of the instability. However the growth rate predicted (*e.g.* at 89% the maximum value of imaginary ω is about 1) is an order of magnitude greater than that observed. This is because the dispersion relation assumes cold ions. Simulation ions have a thermal spread which is damping the instability.

As indicated earlier, small values of R provide a modest two-stream interaction. From the ω-κ plots, we observe that as R is decreased, the value of κ for minimum stability with $v_0 < v_S$ also decreases. In our simulations $\kappa_{min} = 2\pi/L_{max} = \pi$. Hence we may be observing a modest interaction for small R because our system length is too short.

Usually the initiation of the instability occurs within the time that the slower simulation ions have travelled across $2L$. Thus instead of intializing the system empty, we may try to begin fully loaded with Maxwellian particles.

V. Suggestions

Future work will include the effects of system length and simulation initiation on the two-stream interaction. We will also study the dependence of potential and instability growth on mass ratio. Diagnostics for temperature profile and particle and energy flux to the wall will also be implemented.

VI. Acknowledgements

The author wishes to thank W. Lawson for solving the thermal effusion mystery, I. Roth for his useful suggestions, and N. Otani and P. Gray for their enlightening discussions.

Appendix

We present the following derivation of the energy transported by thermal effusion after a long library search in vain.[3] Assume that particles have a Maxwellian distribution of velocity with temperature T in three dimensions x, y, and z. We are interested in the kinetic energy flux along $\hat{x}$.[4] This kinetic energy flux is

$$\mathcal{E}_x = \frac{\int_{-\infty}^{\infty}\int_{-\infty}^{\infty}\int_{0}^{\infty} \frac{1}{2} m v^2 v_x f_0 \, d^3v}{\int_{-\infty}^{\infty}\int_{-\infty}^{\infty}\int_{0}^{\infty} f_0 \, d^3v} \tag{A1}$$

where

$$f_0 = A \exp\left(\frac{v_x^2 + v_y^2 + v_z^2}{-2v_t^2}\right),$$

$$v_t^2 = kT/m,$$

and

$$A = n\left(2\pi v_t^2\right)^{-3/2}.$$

Thus

$$\frac{n}{2}\mathcal{E}_x = \int_{-\infty}^{\infty}\int_{-\infty}^{\infty}\int_{0}^{\infty} \frac{1}{n} m v_x^3 f_0 \, d^3v + \int_{-\infty}^{\infty}\int_{-\infty}^{\infty}\int_{0}^{\infty} \frac{1}{n} m v_y^2 v_x f_0 \, d^3v + \int_{-\infty}^{\infty}\int_{-\infty}^{\infty}\int_{0}^{\infty} \frac{1}{n} m v_z^2 v_x f_0 \, d^3v \tag{A2}$$

$$= \mathcal{E}_{xx} + \mathcal{E}_{xy} + \mathcal{E}_{xz}.$$

Next we evaluate each term of Eq. (A2),

$$\mathcal{E}_{xx} = \frac{Am}{n}\left[\int_0^\infty v_x^3 \exp\left(\frac{-v_x^2}{2v_t^2}\right) dv_x\right]\left[\int_{-\infty}^{\infty} \exp\left(\frac{-v_y^2}{2v_t^2}\right) dv_y\right]^2$$

$$= 4\pi m v_t^6 A/n$$

or

$$\mathcal{E}_{xx} = \langle v\rangle\, kT \tag{A3}$$

where

$$\langle v\rangle = \sqrt{\frac{2}{\pi}}\, v_t.$$

$$\mathcal{E}_{xy} = \frac{Am}{n}\left[\int_0^\infty v_x \exp\left(\frac{-v_x^2}{2v_t^2}\right) dv_x\right]\left[\int_{-\infty}^{\infty} v_y^2 \exp\left(\frac{-v_y^2}{2v_t^2}\right) dv_y\right]\left[\int_{\infty}^{\infty} \exp\left(\frac{-v_z^2}{2v_t^2}\right) dv_z\right]$$

$$= 2\pi m v_t^6 A/n$$

or

$$\mathcal{E}_{xy} = \frac{1}{2}\langle v\rangle\, kT. \tag{A4}$$

Similarly

$$\mathcal{E}_{xz} = \frac{1}{2}\langle v\rangle\, kT. \tag{A5}$$

Combining Eqs. (A3)-(A5), we find

$$\mathcal{E}_x = \langle v\rangle\, 2kT. \tag{A6}$$

Thus the average particle carries an energy of $2kT$ along the x direction.

References

1. R. A. Langley *et al*, "Data Compendium for Plasma Surface Interactions", *Nuclear Fusion* special issue, (1984), pp.186-187.

2. F. F. Chen, *Introduction to Plasma Physics*, Plenum Press, New York, 1974, pp.186-187.

3. W. S. Lawson, Plasma Theory and Simulation Group, EECS Dept., U. C. Berkeley - private communication, June 1985.

4. Shkarofsky, Johnston, and Bachinshi, *Particle Kinetics of Plasmas*, Addison-Wesley, Reading, Massachusetts, 1966.

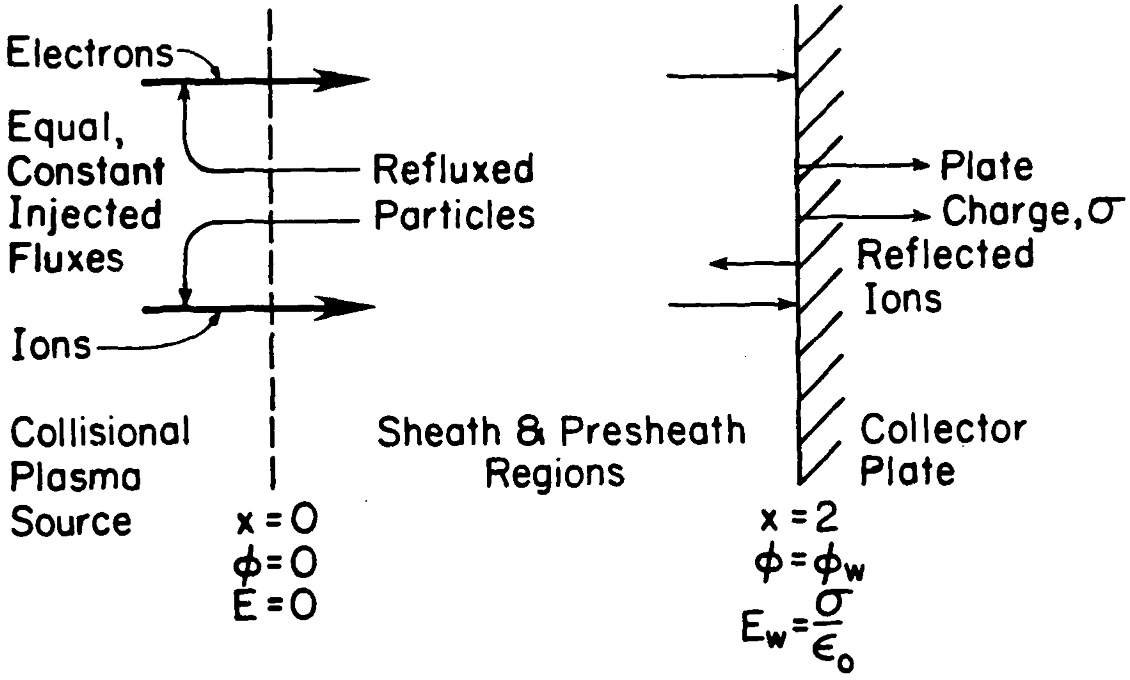

Figure 1. Plasma Model

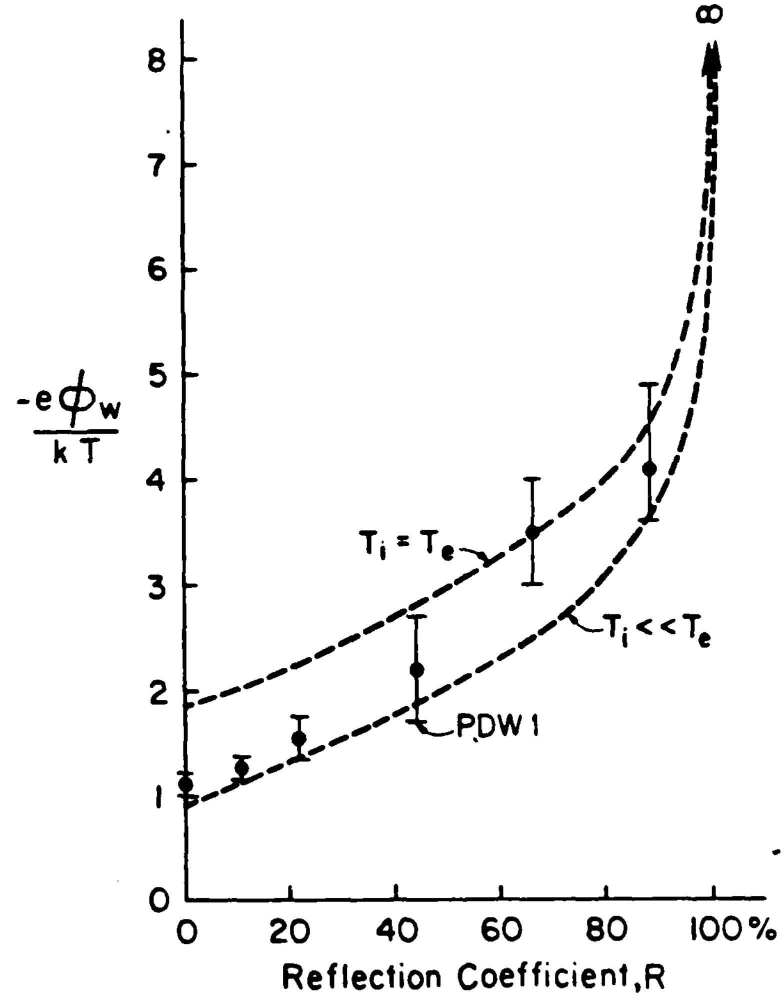

Figure 2. Dependence of wall potential on ion reflection for M/m = 40.

$T_i << T_e$: $\frac{e\phi_w}{kT} = \ln\left[\frac{1-R}{1+R}\left(\frac{2\pi m}{M}\right)^{\frac{1}{2}}\right]$

$T_i = T_e$: $\frac{e\phi_w}{kT} = \ln\left[\frac{1+R}{1+R}\left(\frac{m}{M}\right)^{\frac{1}{2}}\right]$

Bars indicate oscillation amplitude.

For R = 89%, number of particles did not equilibrate.

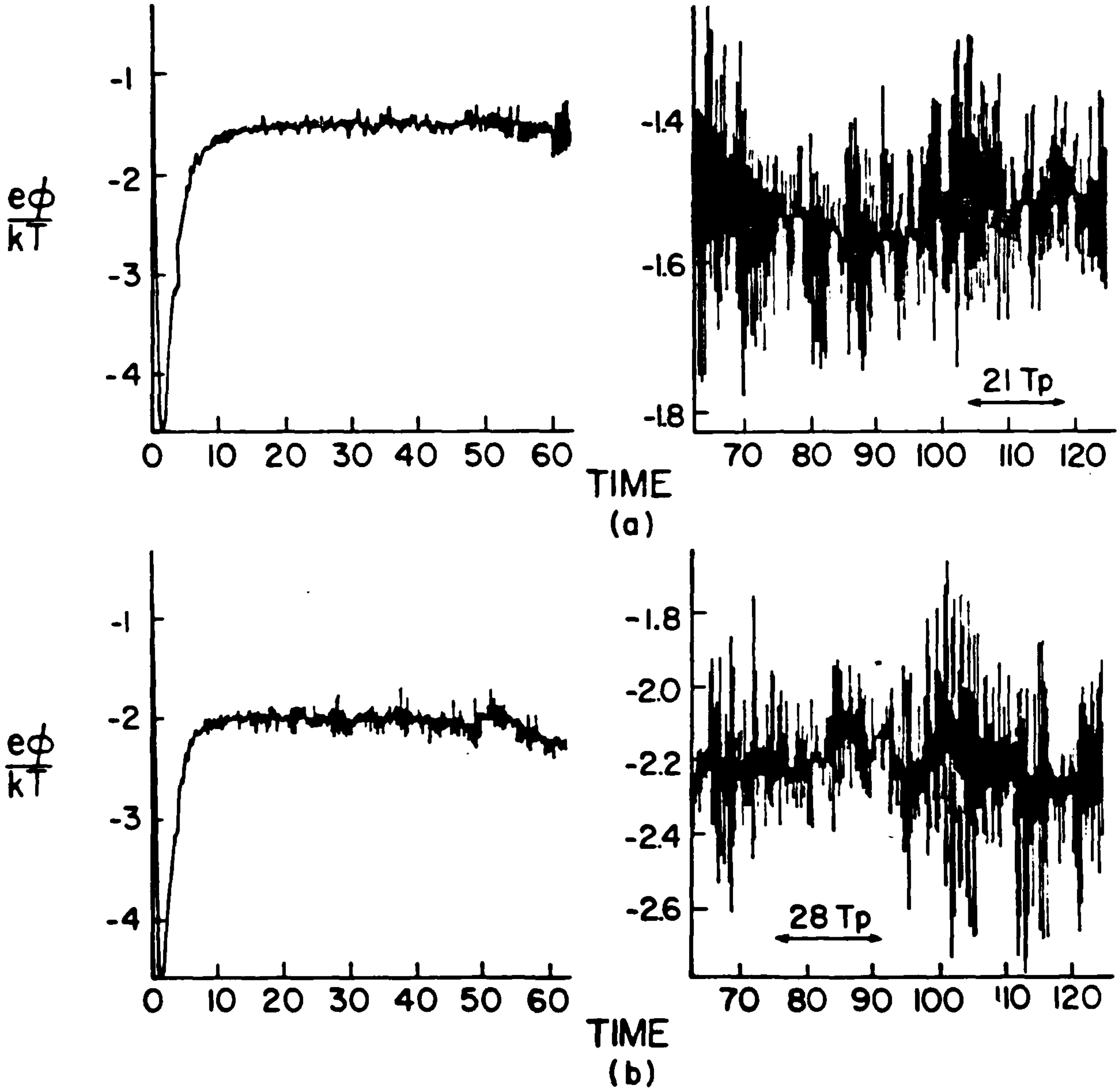

Figure 3. Wall potential history with time in step number * DT for (a) 22% and (b) 44% ion reflection.

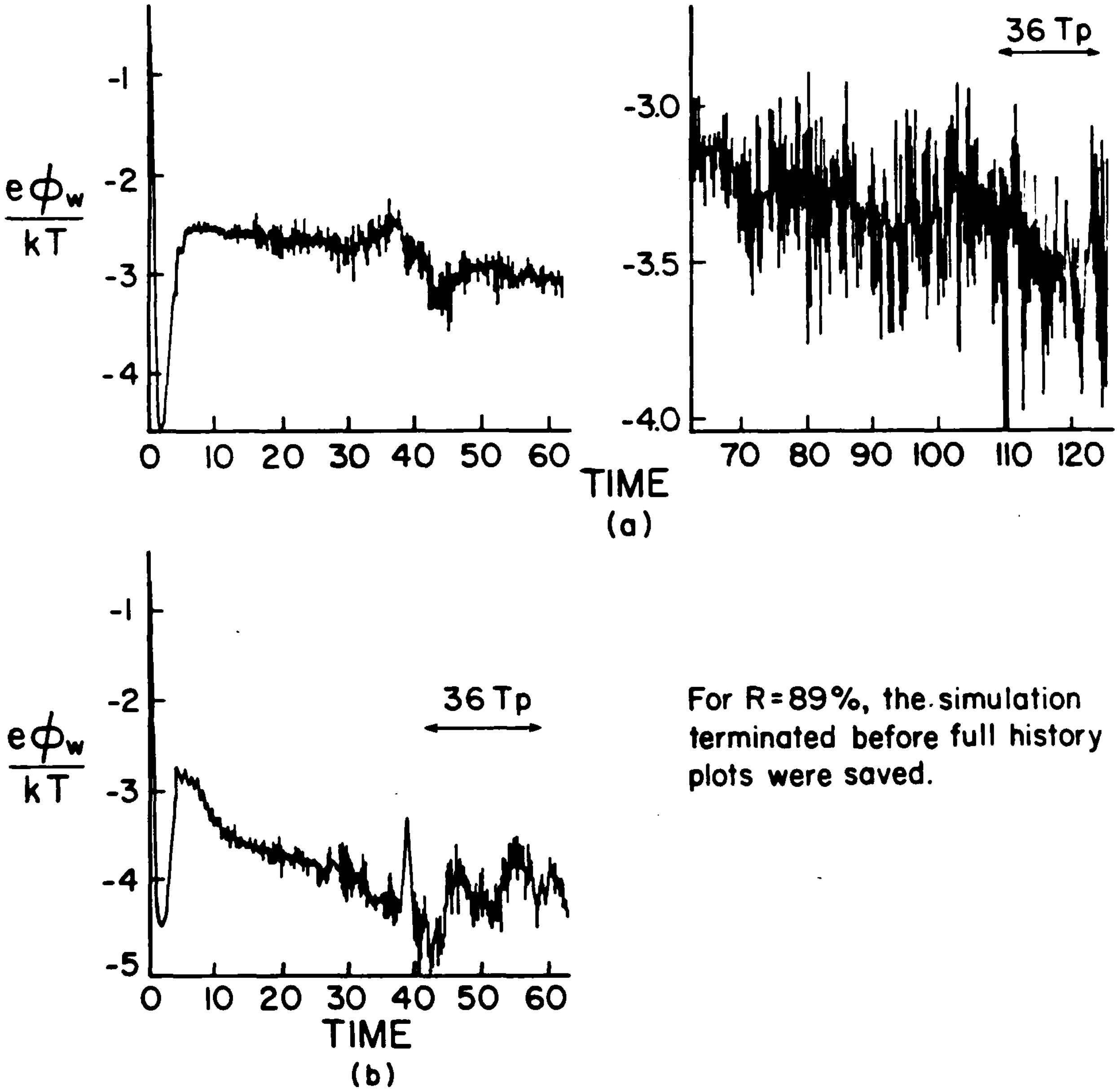

For R=89%, the simulation terminated before full history plots were saved.

Figure 4. Wall potential history with time in step number * DT for (a) 67% and (b) 89% ion reflection.

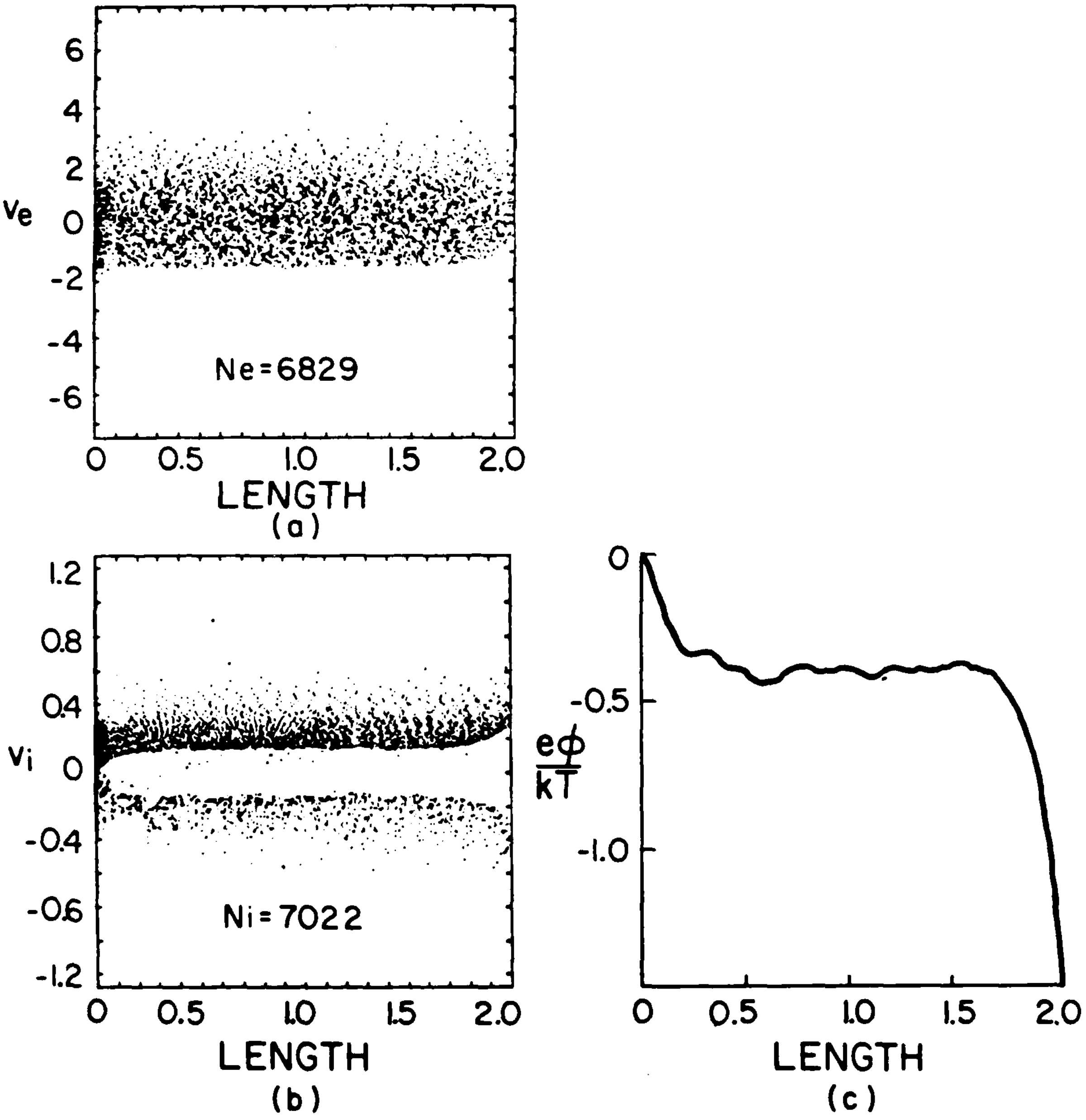

Figure 5. Profiles in (a) electron phase space, (b) ion phase space, and (c) potential for 22% ion reflection at equilibrium (t = 125)

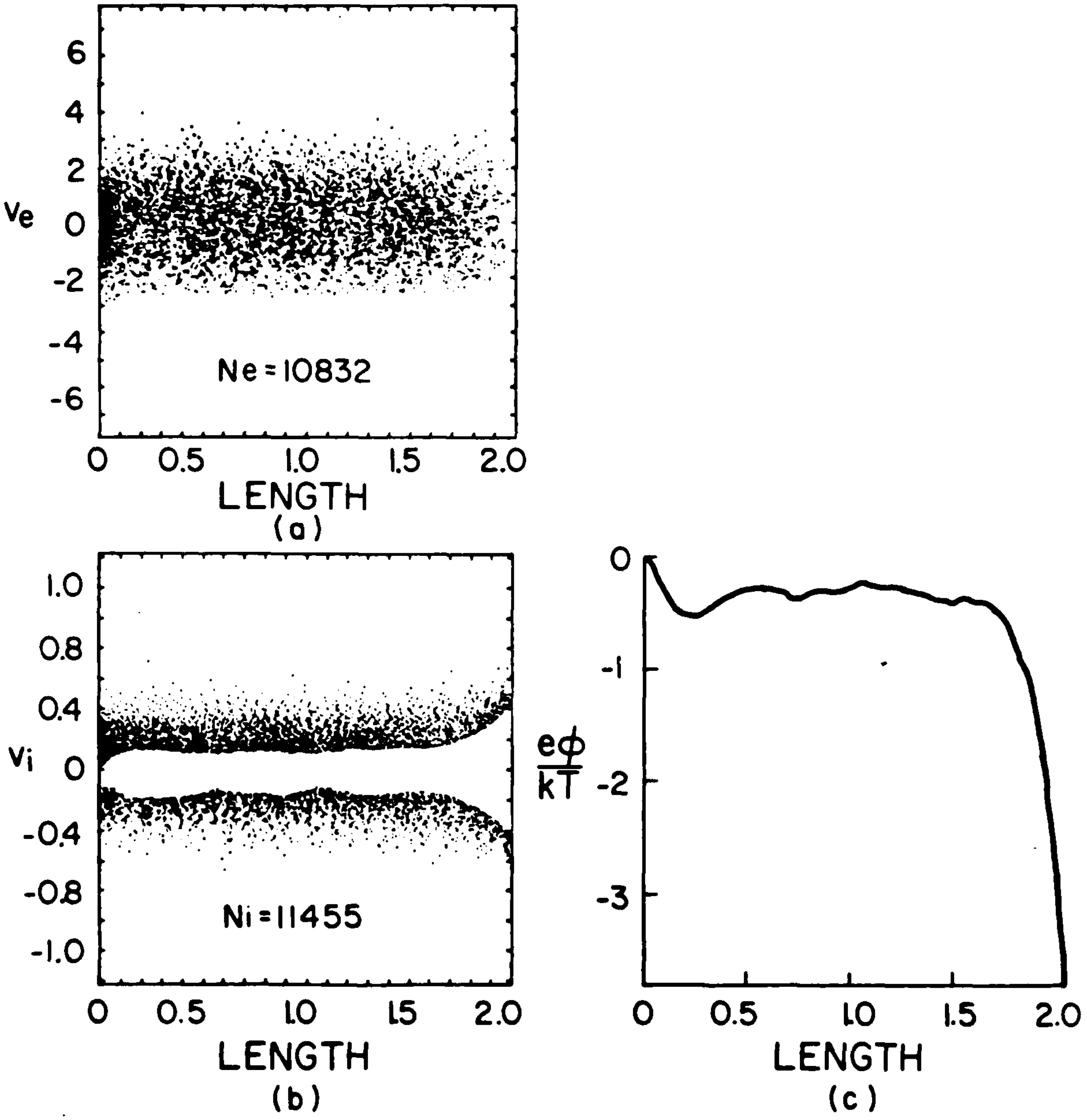

Figure 6. Profiles in (a) electron phase space, (b) ion phase space, and (c) potential for 89% ion reflection at t = 25

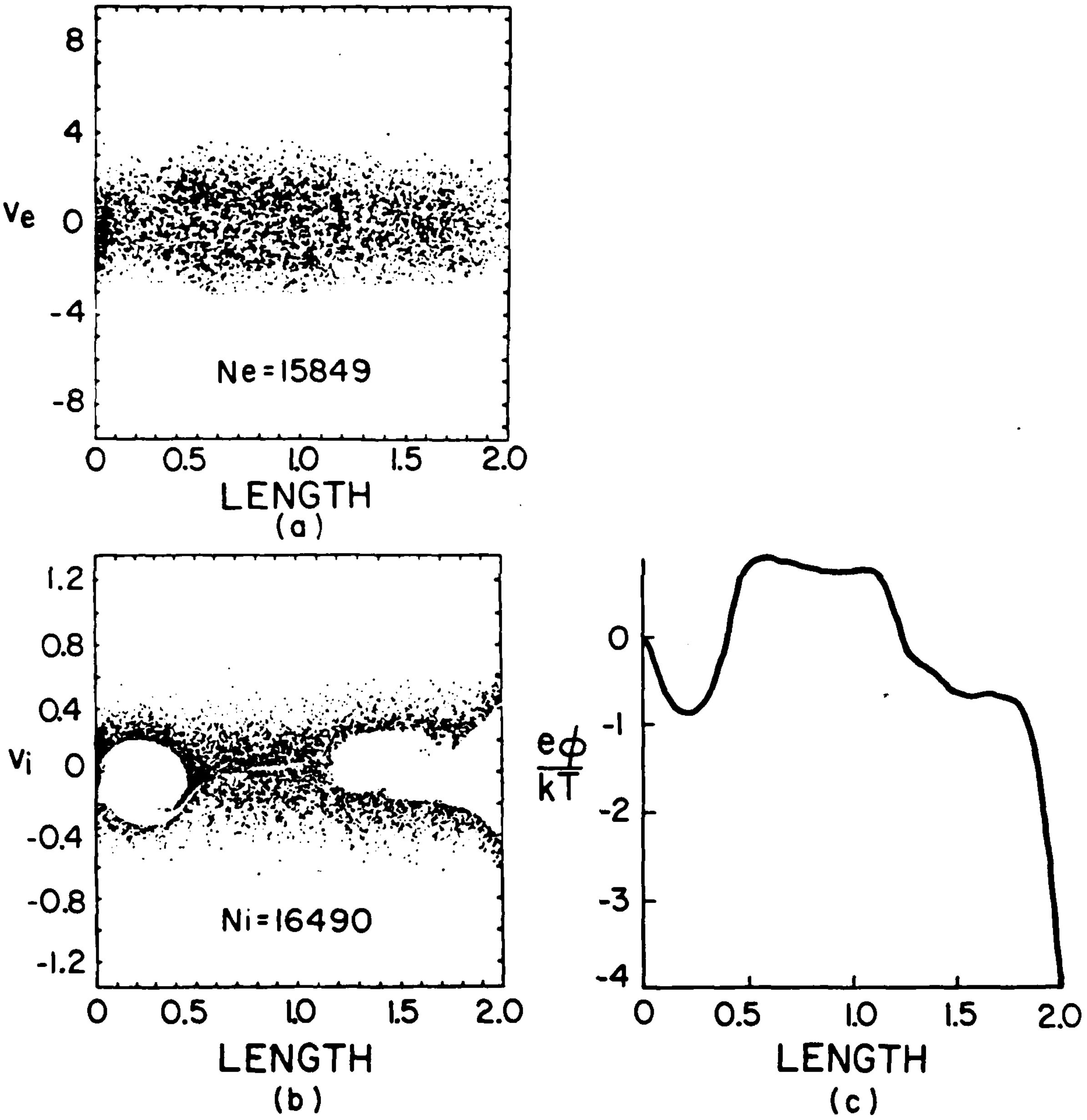

Figure 7. Profiles in (a) electron phase space, (b) ion phase space, and (c) potential for 89% ion reflection at t=37.5

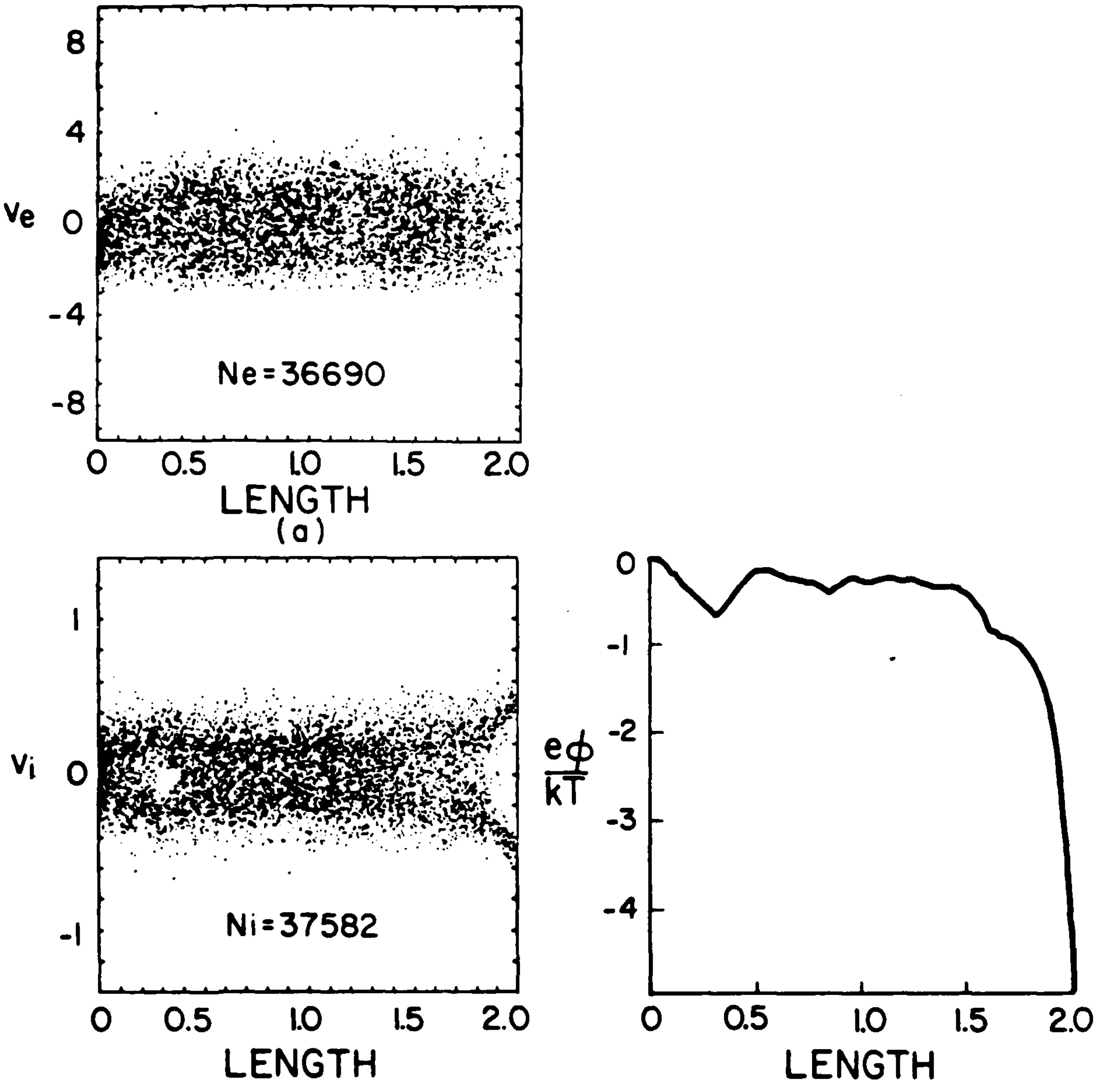

Figure 8. Profiles in (a) electron phase space, (b) ion phase space, and (c) potential for 89% ion reflection at t=100

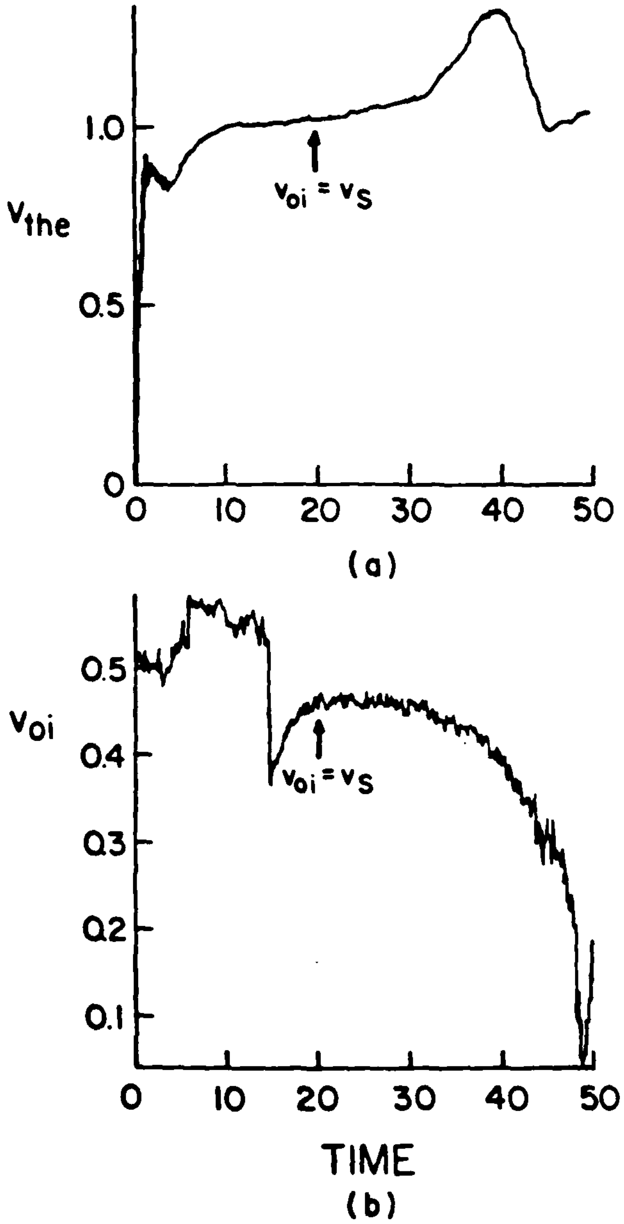

Figure 9. Histories of (a) electron thermal velocity and (b) ion beam velocity for R=89%. $v_s = 40^{-\frac{1}{2}} * v_{the}$. Time in step number * DT. Velocities are averaged over the central half of the simulation length.

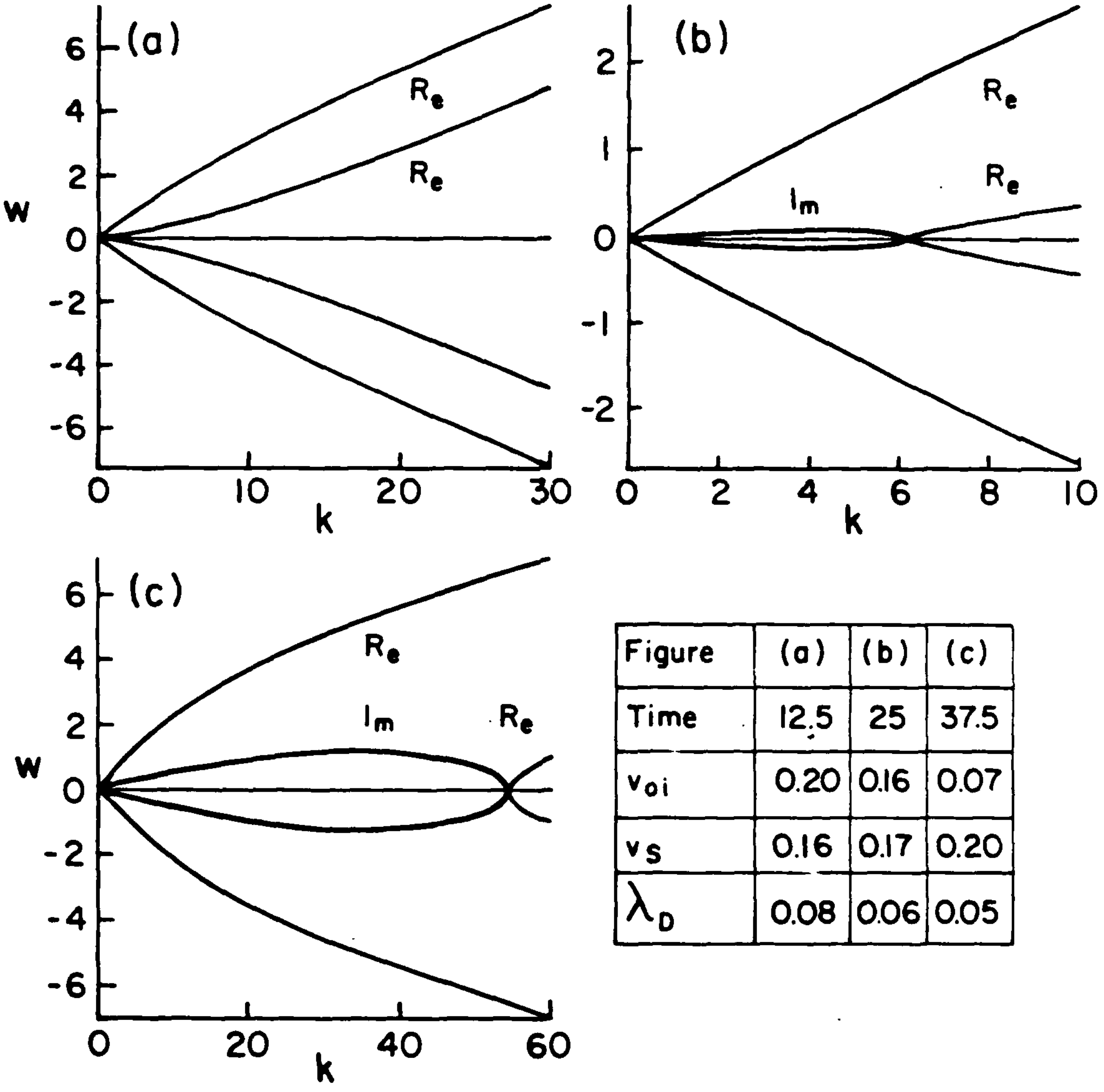

Figure	(a)	(b)	(c)
Time	12.5	25	37.5
v_{oi}	0.20	0.16	0.07
v_S	0.16	0.17	0.20
λ_D	0.08	0.06	0.05

Figure 10. Dispersion diagram for ion - ion two streaming (Eq. 38) for R = 89 %. Parameters measured from simulation.

F. PLANAR MAGNETRON DISCHARGES

Perry Gray (Prof. C.K. Birdsall)
Amy Wendt (Prof. M.A. Lieberman)

This is a new project, initiated recently, primarily by Varian Associates. It is related to our other projects, through the study of the general problem of magnetized sheaths.

INTRODUCTION

We are using two approaches to understand planar crossed field (magnetron) discharges: experiments and computer simulation. We are proceeding with the design and construction of a planar discharge device which is well instrumented to measure the space and time dependence of potentials, fields, densities, and velocities as a function of a variety of parameters. We are also using plasma computer simulation for a similar configuration in order to "measure" the same qualities. This interplay between experiment and simulation is expected to be as productive of understanding in this area as it has been in other areas of plasma research (e.g., fusion). Part A of this report describes the experiment, showing the design and giving future plans. Part B describes the computer simulations done to date and the next steps in modeling.

The past year (August 1983-August 1984) is our initial step in the study of crossed-field discharges. There has been considerable preparatory effort, examining the physics and parameter ranges, designing and building the experiment, and using our existing simulation codes on rudimentary models. As yet, there are no experimental results; there are some simulation results of a general nature. However, results directly applicable to planar magnetron discharges are yet to come.

A typical magnetron discharge is shown in fig.(1); imagine this model rotated about a vertical axis standing on its left side, so as to obtain the so-called racetrack magnetron discharge.

A EXPERIMENT

1. *Summary of Progress*

Mechanical design of the experiment has been completed, and machine shop work is in progress. The experimental chamber and end plate design is shown in Figure2 . Two 8" diameter plates are mounted on the axis of the 12" diameter, 30" long, aluminum vacuum vessel. Each plate is water cooled, insulated from the vacuum vessel, and can be moved along the axis (by means of a hand crank at each end) while the system is under vacuum and the plasma is present. Seven 2" diameter ports in the plane of symmetry provide diagnostic access. Axial access (through each 8" plate) is also available. The azimuthal symmetry of the design allows comparison of two-dimensional (r,z) measurements with two-dimensional computer simulations.

Vacuum design of the experiment has been completed, and all new equipment necessary has been purchased and received. The design makes use of an existing, six-inch, oil diffusion pump system. The chamber pressure can be varied in the range 10^{-6} to 10 torr, and will be feedback controlled in the range 10^{-4} to 1 torr using a 1-3/8", motor-driven, butterfly throttle valve and a capacitance manometer A calibrated, variable leak will be used to set gas flow rates. The first experiments will be done in argon plasmas.

The cooling and electrical system designs have been completed. Most components (cooling manifold, etc.) are in hand, and minimal machine shop work will be necessary. A 0-5 kV, 0-3 A dc power supply for the discharge is in hand for the initial experiments. A higher current source will be purchased if needed.

Space for the experiment has been cleared in Room 111, Cory Hall. The support structure has been designed, all necessary materials have been ordered, and most have been received.

The electromagnet design has been completed, and is shown in Figure 3. All necessary materials have been ordered. Machine shop work will commence after machining of the experiment chamber. The coil will be wound with 104 turns of 0.125" o.d., 0.065" i.d. copper tubing, insulated with 2 mil mylar tape. The coil resistance is estimated to be 0.057 Ω. For a current of 50 A (5200 ampere-turns), the ohmic power dissipation will be 140 W. For this current, the magnetic induction at the pole faces is estimated to be 1.3 Tesla. The cooling water flow rate (two, 520 turn sections in parallel) has been measured to be 7.8 cm^3/sec. For a magnet current of 50 A, the temperature rise will be small 4.4° C. The magnet will be powered using an existing 0-60 A, 0-12 V power supply. At 50 A, the magnet voltage will be 2.9 V.

Plasma diagnostics will at first include the use of Langmuir probes and Faraday cups. Langmuir probes are used to determine ion density, electron temperature, and floating potential within the plasma. Two Langmuir probes and their probe driving circuits are available for use in the experiment. Faraday cups can be used to measure ion and electron fluxes to surfaces, and to obtain information on the energy distributions of these fluxes. A design of miniature Faraday cups for the cathode and anode end plates has been completed.

A time-shared link to the existing plasma data acquisition system is planned. Nearly all the equipment required is presently on hand.

2. *Future Plans*

Machine shop work on the experimental chamber will be completed. The support structure will be constructed, and the chamber and vacuum system will be assembled and tested. A dc glow discharge will be established and used for initial checkout of machine and plasma diagnostics.

After machining of the chamber is completed, the electromagnet will be machined, wound, and tested. It will then be mounted on the cathode plate and used in the generation of planar magnetron discharges.

Measurements of magnetic field $\bar{B}$ will be made using a Bell 615 Gaussmeter, which is available on short term loan. Langmuir probe measurements of ion density n_i, floating potential Φ_f, and electron temperature T_e will subsequently be made. A Faraday cup will be mounted on the cathode plate and its usefulness in determining the local ion flux Γ_i and energy distribution will be studied. Small magnetic field (insulated loops) and electric field (insulated wires) probes will be used to search for rf fluctuation activity in the plasma. Such fluctuations have important implications for particle and energy transport in the discharge.

The time-shared link to the plasma data acquisition system will be installed and tested. This link will make it possible to obtain detailed local measurements of $\bar{B}$, n_i, Φ_f, T_e, and rf fluctuation levels (if any) as functions of r and z (the system is azimuthally symmetric). If Faraday cup measurements are successful, then measurements of ion and electron flux as a function of r can also be made at the cathode and anode plates.

This second phase of detailed (r-z) measurements will extend into the third year of our program to construct a well-instrumented planar magnetron discharge and to study its properties. The objective of this second phase is to provide the data on particle and energy densities and transport coefficients required to compare the experimental results to computer simulation results. Using these experimental and simulation studies, we intend to construct a model of the planar magnetron discharge. Initially, a point model (averaging over r and z) will be developed. However, the goal of the analytical work is to develop a fully two-dimensional (r-z) model of the discharge, as a function of the discharge control parameters (pressure, voltage, power, magnetic field strength, surface materials, and geometry). We believe such a model will be very useful in understanding how the discharge scales to larger sizes, what factors lead to non-uniformity in the deposition pattern, and which pressures, voltages, geometries, etc. maximize the deposition rate.

B COMPUTER SIMULATION

1. *Summary of Progress*

We have begun applying computer simulation to crossed-field glow discharges by starting with a simpler model which is better understood. However, new physics is being added step by step. The current model is planar, one dimensional, bounded, and magnetized. Thousands of charged particles are used to model the electrons and ions, all followed self-consistently in their own and the applied electric and magnetic fields.

The state of the art in many-particle simulation is found in any plasma and computational journals and in our new book*. The simulations are initial-value, boundary-value solutions, *including sources and sinks, complete with non-intrusive* diagnostics. The generally presented results are graphical, both during and at the end of computer runs of a few thousand time steps. In one dimension, x, v_x, v_y, v_z, (which is favored, as being most economical and most easily transferable from Berkeley to other computer systems) moderate runs on a CRAY-1 computer take 5-10 minutes (10,000 electrons and ions for 10,000 time steps) and about 50 to 100 times that on a VAX computer. In two dimensions, x, y, v_x, v_y, v_z, there must be substantial time increases, as many more particles are needed to fill the second dimension. There is no lack of 1d and 2d codes, but ***all*** must be modified and run carefully to produce believeable physics,

The major support for the PTS Group is for fusion plasma research, from DOE and ONR; the Varian Associates support allows us to complement such, moving into plasma-wall research with non-fusion applications.

The most thorough study of a bounded plasma done by us this past year was for a Q-machine model; one end plate was an electron and ion source and the other was an absorbing cold plate, which could be biased or floating. Normally there are two sheaths, one at each end, with a zero field region in between. One finding, reversing an assumption made for decades, with ion rich emission, was that there was no electron hole (it was filled) at the emitter sheath; this was found by comparing φ_{max} and φ_{plasma} from simulation with predictions from time-independent theory, which gave different answers and was subsequently

---

*C. K. Birdsall and A. B. Langdon, ***Plasma Physics via Computer Simulation***, McGraw-Hill, N.Y., 1985 (out late October 1984).

improved to have the "filled" hole (with excellent agreement). See Figure 4. Another finding, quite striking, was the plasma turbulence seen in electron and ion phase space plots, and the moving double layer seen in potential plots, for moderate positive bias. While the disruptive currents found have been observed before, experimentally and in simulation, it is believed that the showing of all plots simultaneously (a movie) is a major step in identifying almost all of the anomalous behavior. See Figure 5. Simulation results provide us with the velocity distributions and transport coefficients in the plasma and sheath regions of the discharge, for comparison to experimental results.

A step in the direction of understanding cros sed-field models is to add a static magnetic field at angle ψ with the axis (between plates). Our initial observations of magnetized plasmas (and also by Roland Chodura, IPP, Garching bei Munchen, FGR) are that with $\psi < 90°$, the usual positive plasma is observed (electrons lost to the walls); however, we find with $\psi = 90°$ ($\underline{B}$ parallel to the plates), the plasma becomes negative as ion gyroradii exceed those of electrons and thus ion transport exceeds electron transport to the wall, as at the cathode surface of a planar magnetron discharge. For ψ nearly 90°, the initially-negative plasma soon becomes positive, as electrons move along the field lines to the wall; *the sensitivity to ψ near 90° needs investigation.* Chodura's theory and simulations indicate a magnetic pre-sheath, lengthening as $\psi \rightarrow 90°$; he has no results for $\psi = 90°$. We plan collaboration with Chodura early next year, partially to resolve the "90° sheath" or "side wall sheath," of interest to both fusion and crossed-field devices.

Another magnetized model is shown in fig.6. A 1d3v simulation has been started in the xy plane, using $B_z(x)$ only, and we are looking at a slice in the middle of the linear dipole field.

Future Plans

We are also adding binary charged particle collisions, scattering with neutrals, charge exchange, reflected ions, and secondary (and other) electrons to the code. Each of these steps is nontrivial. We expect to make most of these additions during the next year.

A major step will be to a two-dimensional model, fully crossed-field, in the cross-sectional plane of the typical permanent magnet crossed-field discharge used in sputtering. This model will be developed during the second and third years of our studies.

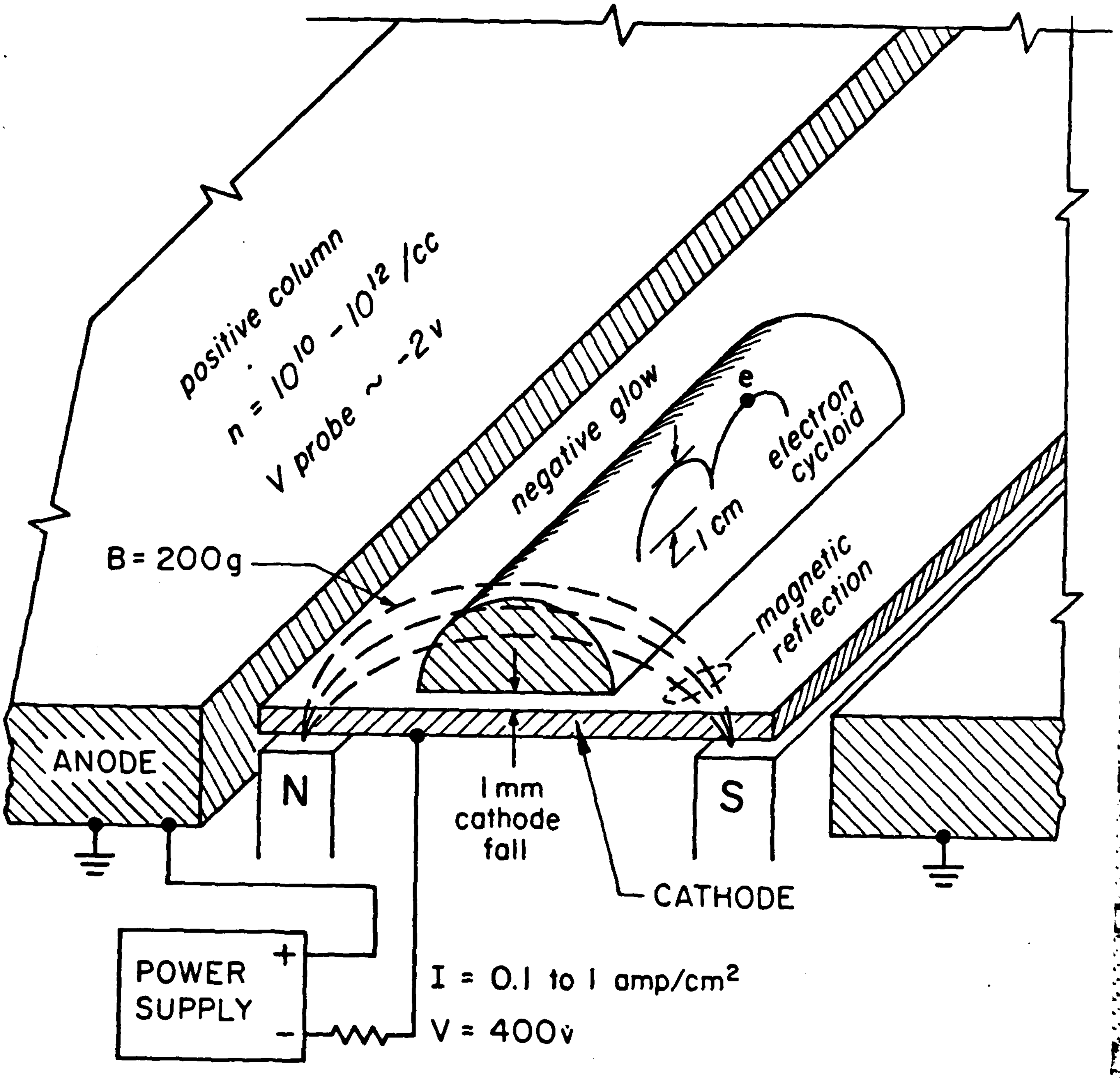
positive column
n = 10^{10} - 10^{12} /cc
V probe ~ -2v
negative glow
e
electron cycloid
1 cm
B = 200g
magnetic reflection
ANODE
N
S
1mm cathode fall
CATHODE
POWER SUPPLY
+
–
I = 0.1 to 1 amp/cm^2
V = 400v

Fig. 1

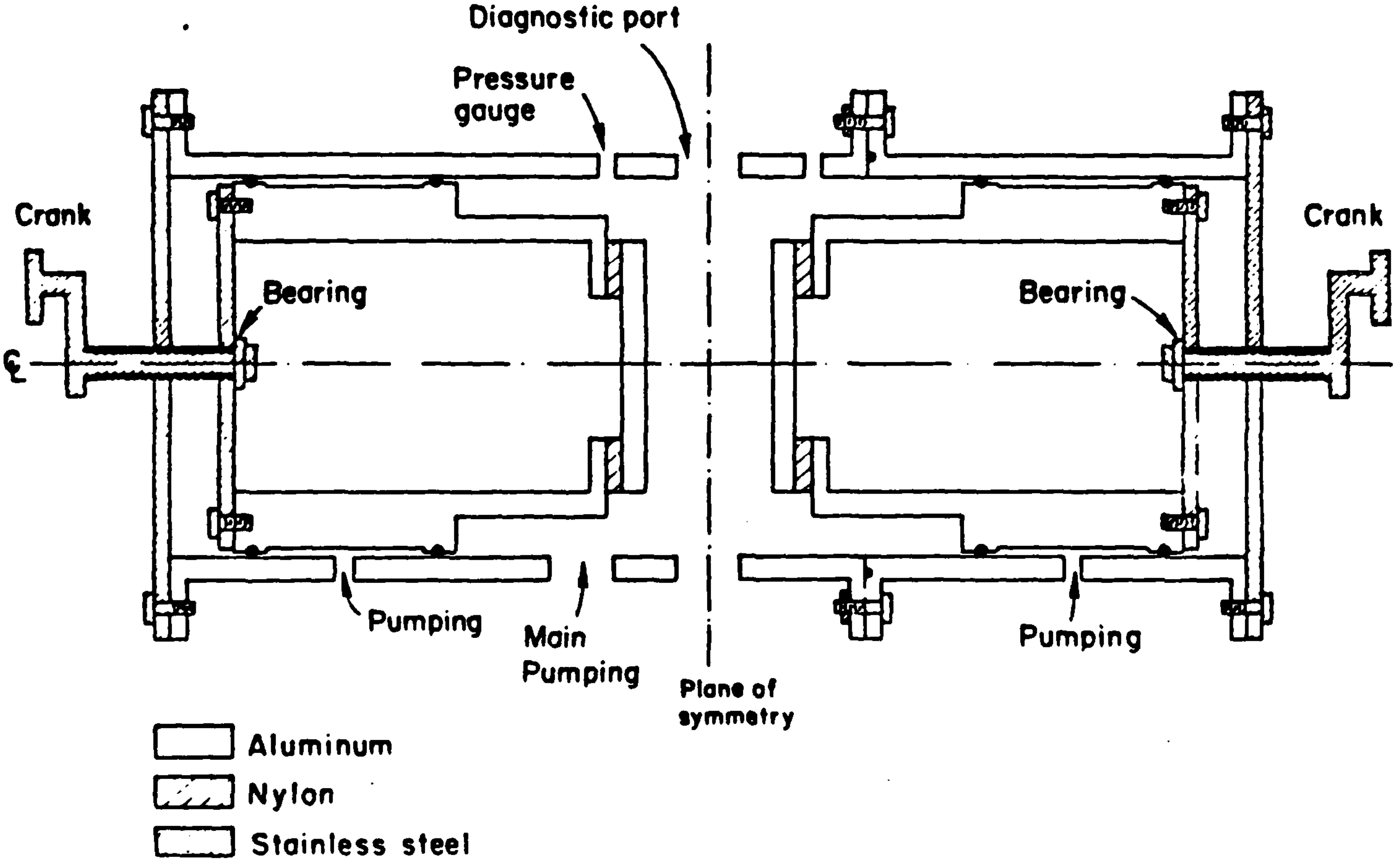

Figure 2. Experimental chamber and end plate design.

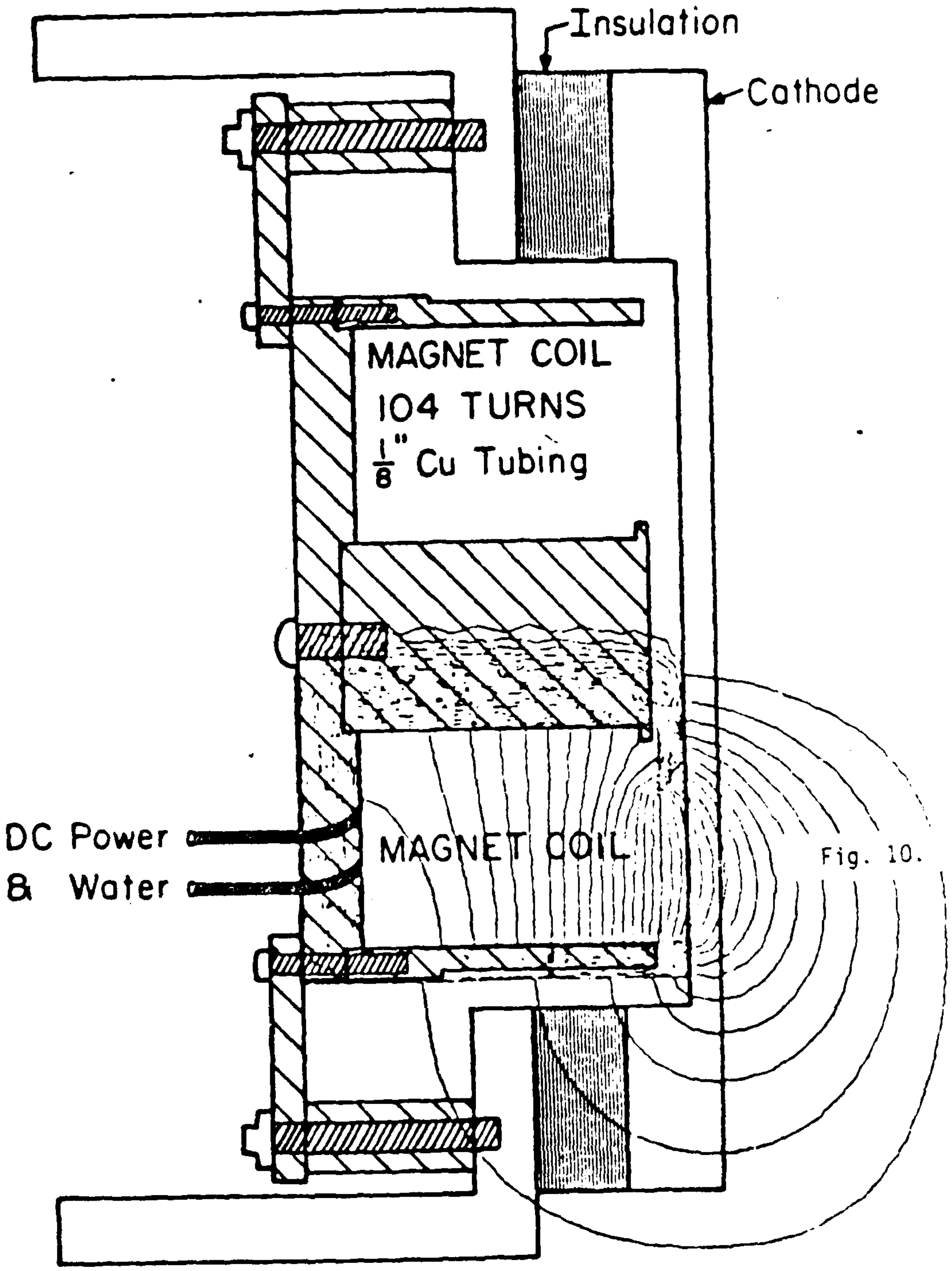

Fig. 3. Cross-section of cathode configuration.

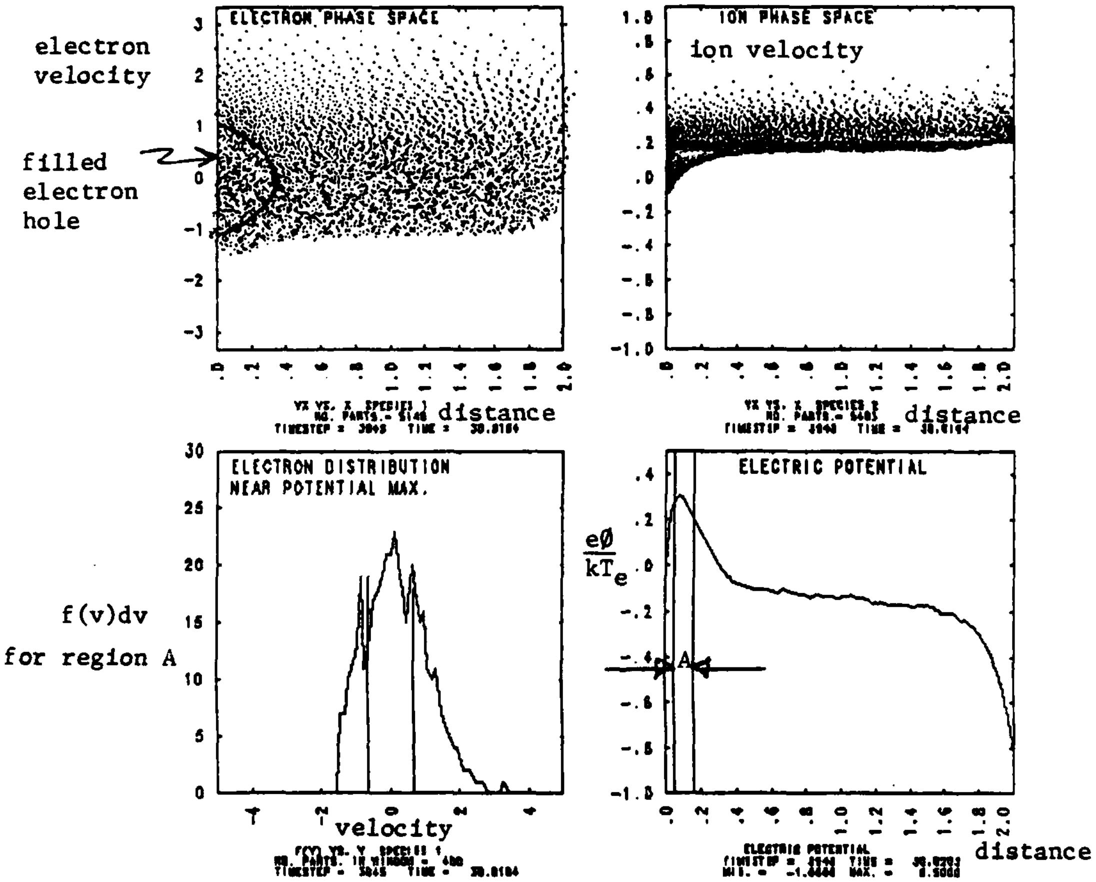

Figure 4. Particle simulation snapshot, for ion-rich source, showing filled electron hole, causing change in theory. Electron and ion source is at left, absorbing, floating plate at the right.

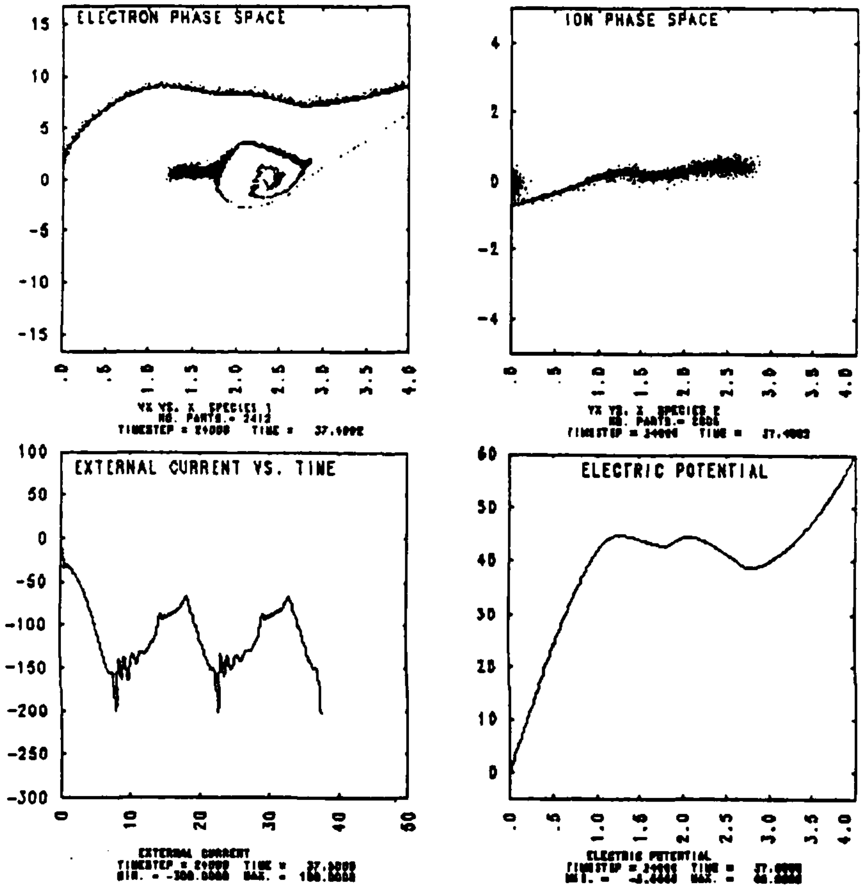

Figure 5. Similar to Figure 4, but with absorbing plate biased (by a battery) with a moderate voltage. A potential minimum formed at earlier time, trapping the electron vortex shown in electron phase space. The current in the external circuit shows the anomalous effects, repetitive, with both high and low frequency parts. The ions are returned to the source at about the full applied potential (many times $v_{\text{thermal, ion}}$).

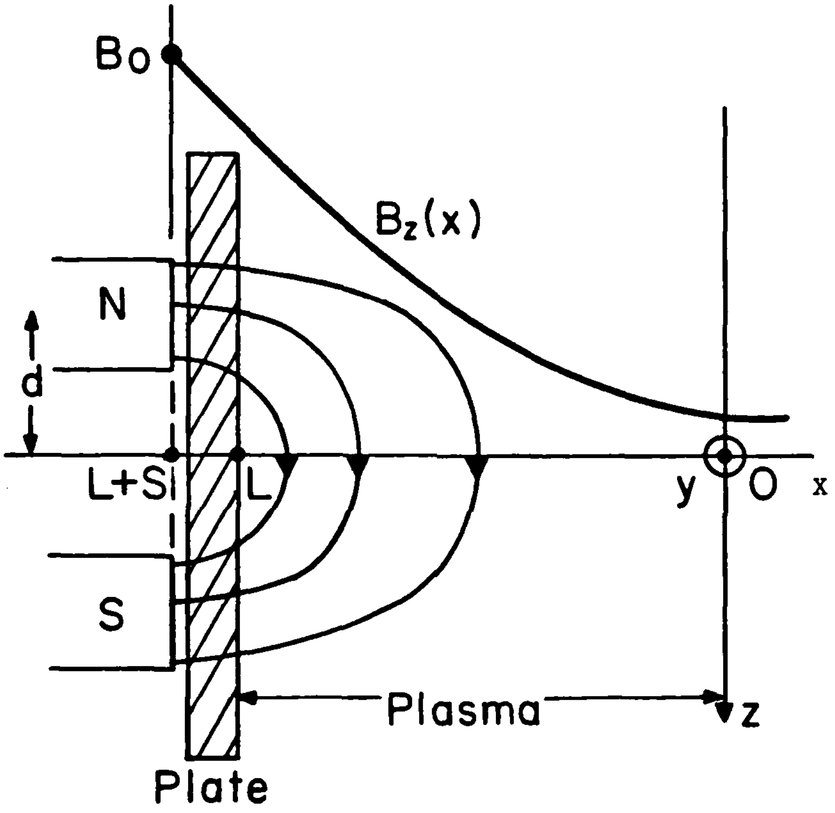

Fig.6

G. PARTICLE SIMULATIONS OF THE LOW-ALPHA PIERCE DIODE.

Paper presented at the International Conference on Plasma
Physics, June 27-July 3rd 1985, Lausanne, Switzerland.

PARTICLE SIMULATIONS OF THE LOW-ALPHA PIERCE DIODE*)

T.L. Crystal and S. Kuhn*)

Plasma Theory and Simulation Group, EECS/ERL
University of California, Berkeley, CA 94720

Abstract. Particle simulations are used to study the evolution of small initial perturbations about the uniform classical Pierce diode equilibrium in the parameter range $0 < \alpha = \omega_p L/v_0 < 3\pi$. Linear properties recovered show quantitative agreement with theoretical predictions. Long-time behavior is found to depend on α and, in one case, also on the initial conditions.

1. Introduction. The "classical" Pierce diode[1-3] is characterized by externally shorted electrodes (at x=0,L), a uniform background of immobile ions, and cold electrons injected constantly at x=0 with density n_0 and velocity v_0. Out of the various equilibrium states this classical Pierce diode may exhibit,[2] the uniform one ($\partial/\partial x=0$, $\partial/\partial t=0$) is of particular importance. The linear eigenfrequencies associated with it, $\omega_\mu = \omega_{\mu r} + i\gamma_\mu$ (with μ = 1,2, ...), are the roots of the characteristic equation[1-3]

$$e^{i\alpha\eta}[(\eta^2+1)\sin\alpha + 2i\eta\cos\alpha] + \alpha\eta^3 - \alpha\eta^2 - 2i\eta = 0,$$

where $\eta = \omega/\omega_p$ and $\alpha = \omega_p L/v_0$, with $\omega_p = \sqrt{n_0 e^2/\epsilon_0 m_e}$. The potential pattern of eigenmode μ may be written in the form[3]

$$\phi_\mu(x,t) = [\phi_{\mu r}(x)\cos(\omega_{\mu r}t+\delta) + \phi_{\mu i}(x)\sin(\omega_{\mu r}t+\delta)]\exp(\gamma_\mu t).$$

All linear properties are conveniently classified in terms of α. The α-values considered below (0.5π, 1.5π, 2.5π) are representative of the "archetypical" α-intervals (0,π), (π,2π), and (2π,3π), for which detailed predictions on linear behavior are available.[2,3] The purpose of the present paper is to check some of these predictions, and to study, in the linearly unstable cases, the nonlinear evolution as well as the "final" states of the classical Pierce diode.

The simulations were performed with the new bounded-plasma code PDW1[4] in the one-dimensional electrostatic mode. Each run was initialized with a slightly perturbed electron density profile $n(x,t=0) = n_0 + \hat{n}\cos\frac{2\pi x}{L}$ ("positive" initialization) or $n(x,0) = n_0 - \hat{n}\cos\frac{2\pi x}{L}$ ("negative" initialization), where $\hat{n} \ll n_0$. In all cases, the number of simulation particles involved was about 2000, and the fields were calculated on a grid of 128 points using a finite-difference Poisson scheme. We also chose $e/m_e=1$, $\epsilon_0=1$, $L=1$, and $v_0=1$. As useful diagnostic quantities we define an "internal electrostatic energy" and its rate of change by

$$W(t) = \frac{e}{2}\int_0^L dx\,[n_0 - n(x,t)]\,\phi(x,t) \quad \text{and} \quad \gamma_W(t) = \frac{d\ \ln W}{dt},$$

respectively. In the linear regime, we only consider the dominant (μ=1) and next-to-dominant (μ=2) eigenmodes.

2. α = 0.5π. Theoretical predictions:[3] $\omega_1^{th}/\omega_p = -1.2271i$ (non-oscillatory decay), ϕ_{1r}^{th} as shown in Fig. 1a; $\omega_2^{th}/\omega_p = 5.412 - 2.546i$ (oscillatory decay). Results of a simulation run with positive initialization are shown in Figs. 1b-d. From Figs. 1b and 1c, the dominant-eigenmode stage (in which, by definition, all other eigenmodes are negligible relative to the dominant one) is seen to set in a t≈3.5. In this stage, the difference $\gamma_W(t)-2\gamma_1^{th}$ (where "th" stands for "theoretical") is practically zero, thus confirming the predicted decay. Also, the simulated [illegible] t=4 (Fig. 1d) [illegible] with that of Fig. 1a. Finally, the oscillation frequency of the transients in Fig. 1c was measured to be [illegible]ω_p, which is in fair agreement with ω_{2r}^{th}. Similar agreement was found in a run with negative initialization.

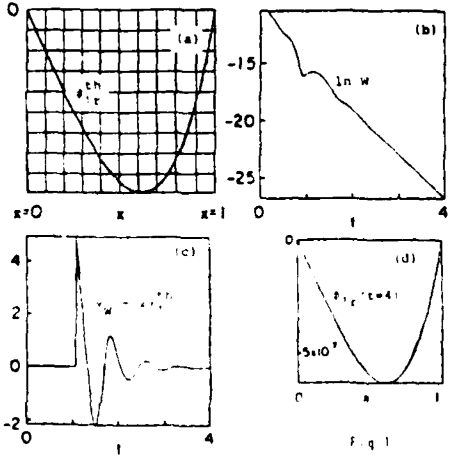

Fig 1

3. α = 1.5π. Theoretical predictions:[3] $\omega_1^{th}/\omega_p = 0.1525i$ (non-oscillatory growth), ϕ_{1r}^{th} (not shown here); $\omega_2^{th}/\omega_p = 2.5130 - 0.6869i$. These linear properties were verified quantitatively as described for α=0.5π. The global evolution of the (unstable) system for positive initialization is documented by Fig. 2,

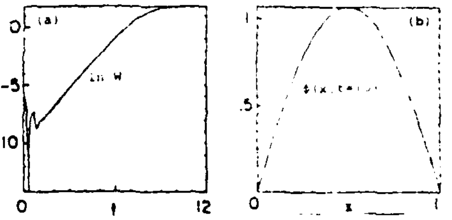

Fig. 2

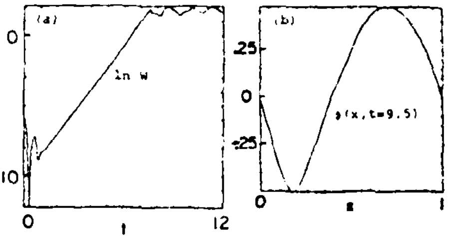

Fig. 3

according to which the diode reaches, at t≈10, a new, non-uniform, stable d.c. equilibrium with the parabolic potential profile shown in Fig. 2b. This is in sharp contrast to the *case of negative initialization*, in which the final state is characterized by large-amplitude relaxation oscillations (Fig. 3a). The related potential profile basically maintains the shape shown in Fig. 3b, but oscillations of the virtual cathode near the injection plane periodically interrupt the flow of electrons to the right, thus giving rise to large-amplitude oscillations in the external current.

4. α = 2.5π. Theoretical predictions:[3] $\omega_1^{th}/\omega_p = 0.1319 + 0.0750i$ (oscillatory growth), $\phi_{1r}^{th}(x)$ and $\phi_{1i}^{th}(x)$ (not shown here); $\omega_2^{th}/\omega_p = 1.9203 - 0.3748i$. The predicted properties of the dominant eigenmode were again verified as before, but the next-to-dominant eigenfrequency extracted was too inaccurate to be conclusive. Figure 4a shows the global evolution for positive initialization, which again leads to a state of significant noise. What is new is that there are now *two* oscillating virtual cathodes (Fig. 4b), which alternatingly reflect electrons and thus give rise to a *fairly complex distribution* in phase space (Fig. 4c). The same type of final state was observed for negative initialization.

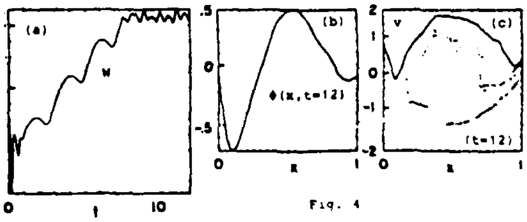

Fig. 4

---

*) Work supported by DOE Grant DE-AT03-76ET53604, ONR Grant N00014-77-C-0578, and Austrian Research Funds Grant S-18/03. All computations were performed at NMFECC, Livermore.

*) Permanent address: Institute for Theoretical Physics, University of Innsbruck, A-6020 Innsbruck, Austria.

[1] J.R. Pierce, J. Appl. Phys. 15, 721 (1944).

[2] B.B. Godfrey, Reports AMRC-R-282 (1981), AMRC-N-212 (1982), and AMRC-N-245 (1983), Mission Research Corp., Albuquerque, NM 87106.

[3] S. Kuhn, Phys. Fluids (to appear June 1984).

[4] Wm.S. Lawson, User's Manual for the PDW1 Code, EECS/ERL, U.C. Berkeley, CA 94720 (1984).

Paper presented at the Second Symposium on Plasma Double Layers and
Related Topics, July 5/6, 1984, Innsbruck, Austria.

H . Theory and Simulation of Ion Acoustic Double Layers

K. Y. Kim and T. L. Crystal

E.R.L., University of California, Berkeley,CA. 94720

1. Simulations of Ion Acoustic Double Layer

All simulations are done with a 1d axially-bounded electrostatic PIC code. In all of our simulations, we have used the same mass ratio ($m_i / m_e = 100$); the time step is $\omega_e \, \delta t = 0.2$. Initially, the simulation plasma density is uniform in space. The ion and electron distribution functions are both Maxwellian; the ions are cold, $T_i \ll T_e$, and the electrons are drifting relative to them with drift velocity v_d. This relative drift between the electrons and ions constitutes a current and can result in instability depending on v_d.

(a) Simulations of current driven systems

In our simulations of constant current driven system, we have found that, weak ion acoustic double layers can be formed even in a very short system ($80\lambda_e$), and even when the electron drift velocity is small compared to previous simulations ($v_d = 0.45 v_{th} \approx 4.5 C_s$); the double layer formation mechanism is still based essentially on amplification of a small negative potential dip, due to reflection of electrons.

Using a temperature ratio $\tau = T_e / T_i = 20$ and plasma parameter $n\lambda_e = 100$, the system plasma is loaded uniformly in space; there is thus no electric field initially. From Figure 1 note that by time $\omega_e t = 480$ a small negative potential dip has developed that is associated with an ion phase space distortion as well as with an ion density dip. From subsequent "snapshots" of this potential dip, it is seen to be moving with nearly ion acoustic velocity (C_s). Therefore it can start to trap those ions which are resonant with the structure (*i.e.*, ions in the *positive* velocity tail of the distribution), and an ion hole starts to form there. At the left side of the growing potential dip, electrons with velocity slightly greater than the ion acoustic velocity contribute to the structure's growth; their velocity distribution (in the moving frame of potential dip) has positive slope, so that they give up their energy to this potential.

As the negative potential structure grows and decelerates due to this electron reflection, the dip is able both to trap more ions and, at the same time, to reflect more electrons. "Positive" momentum transfer due to electron reflection leads to "deceleration" of the ion hole, and the potential thus appears to have a negative effective mass as well as negative effective charge. This deceleration and growth of the potential dip can lead to increased ion trapping, because the structure sees more densely populated ion distribution as it decelerates. This electron reflection causes the asymmetry of potential due to more electron density buildup at the left hand side of potential dip than that of right hand side. At time $\omega_e t = 880$, an ion acoustic double layer is well developed, with a negative net potential jump $|\delta\varphi| = 0.3 \, T_e$ over a distance of about $10\lambda_e$.

One reason for initiation with the low drift velocity of our simulation is the condition of *constant* current injection as opposed to the previous simulations using decaying current injection. Of cource, there is a similarity between our system (with constant current condition) and previous long periodic simulations with decaying current conditions; because the system length is *long* in the periodic simulation and because of periodicity (a particle leaving at one boundary is replaced at the opposite boundary by an incoming particle with the same initial velocity), early in time there is *nearly* constant current coming in and going out. This nearly constant current in a *long* periodic simulation acts as a source of energy which leads to the formation of weak ion acoustic double layers by the reflection of electron current. However, our bounded simulation system, with constant current injection has more energy available than that of a long periodic simulation system, resulting in a lower threshold drift velocity than that of a periodic system.

In all of our simulations, the negative potential dip always moves in the same direction (*i.e.*, that of the electron drift velocity). This is because right going ion acoustic waves are preferentially amplified by the inverse electron Landau damping but left going ion acoustic waves are severely attenuated by the Landau damping. The early growth and deceleration of the potential dip can be understood qualitatively as a simple momentum exchange between the structure and the particles. The rate of change of ion acoustic double layer momentum should be approximately equal to the negative of the rate of change of particle momentum; this can be expressed by considering the reflection of electrons and ions by the ion acoustic double layer as follows(see Fig. 2.(b)):

$$-\frac{dP_{iadl}}{dt} = -2m_e \int_0^{(p_{e1}-p_e)^{1/2}} dv\, v^2 f_e(M+v) \; + 2m_e \int_0^{(p_{e1})^{1/2}} dv\, v^2 f_e(M-v)$$

$$- 2m_i \int_0^{p_i^{1/2}} du\, u^2 f_i(M+u)\,. \qquad (1)$$

where $p_e = \frac{e}{m_e}\psi$, $p_{e1} = \frac{e}{m_e}\psi_1$, $p_i = \frac{e}{m_i}\psi$ and M represents the velocity of ion acoustic double layer. It is straightforward to write down the small amplitude limit(ψ_1, $\psi \ll 1$) of the above equation.

The first term in Eq.(1) represents the positive momentum transfer(i.e. electron momentum loss) due to electron reflection from the left hand side of ion acoustic double layer. The second term in Eq.(1) represents the negative momentum transfer due to electron reflection from the right hand side of ion acoustic double layer. The third term in Eq.(1) represents the positive momentum transfer due to ioer due to ion reflection from the left hand side of ion acoustic double layer.

Initially there is no appreciable asymmetry in the potential structure (*i.e.*, $\psi \approx 0$) and $dP_{iadl}/dt > 0$ since electron drift is in the right direction and thus $\frac{df_e(M)}{dv} > 0$. Due to this *positive* momentum transfer(i.e. electron momentum loss) by electron reflection, the ion acoustic double layer having negative effective mass decelerates; the negative effective mass results from the ion density dip associated with the ion acoustic double layer. As potential asymmetry develops by electron reflection(i.e. $\psi > 0$), ion reflection starts come into play and the second term starts to compete with the first term. For the cold ion case, the third term can be considered negligible, and ion acoustic double layer can receive net positive or negative momentum transfer and thus decelerate or accelerate, depending on the relative magnitude of ψ_1 and ψ, the velocity of the ion acoustic double layer and the electron distribution function at both sides of the ion acoustic double layer.

(b) Simulation of voltage driven systems

For the constant voltage driven system with current injection ($\delta\varphi = 0.5$), we have found results that are similar to the above current driven simulation. An important new feature however, is that the ion acoustic double layer now *always* appears first near the left side of wall and develops more quickly than in the earlier current driven simulation (Fig. 4 and 3). In addition, our constant voltage driven simulation requires a lower electron drift velocity ($0.2v_{th}$) for the formation of ion acoustic double layers than was necessary in the constant current driven simulations.

In our constant voltage driven system with current injection at the boundary, an applied potential across the system acts to increase the *effective* drift velocity of electrons. Since ions injected at left boundary see a potential barrier due to the applied potential, they will be reflected, thereby forming an ion phase space density dip, which contributes to the formation of a negative potential dip near the left side of the wall(Fig. 3(a)). Therefore, we expect to find formation of ion acoustic double layers at a lower electron drift velocity and near the left side of the wall.

2. Theory of Ion Acoustic Double Layers

Using our graphic method, we shall show that there is a "critical" velocity for the existence of ion acoustic double layers, which is smaller than the value reported in previous papers, and that there are maximum amplitudes of the potential dip corresponding to the drift velocities exceeding critical velocity. *We also find that the net potential jump across the ion acoustic double layers is* determined by the temperature difference between two plasma regions.

From the simulations we see that the electron kinetics are important and our theory accordingly must start with a reasonable yet tractable kinetic electron model which uses all three constants of motion. To this end, we introduce the following *"modified Schamel" type of electron distribution function*, having three electron components:

$$f_e = \frac{1}{\sqrt{2\pi}} \left\{ e^{-\frac{1}{2}(\mathrm{sgn}\, v \sqrt{\varepsilon} - v_d)^2} \Theta(\varepsilon - 2\psi_1) \right. \tag{2}$$

$$\left. + e^{-\frac{v_d^2}{2}} \left[f_\beta \Big(1 - \mathrm{sgn}(x - x_m)\Big) e^{-\frac{\beta\varepsilon}{2}} + f_\delta \Big(1 + \mathrm{sgn}(x - x_m)\Big) e^{-\frac{\delta\varepsilon}{2}} \right] \Theta(-\varepsilon + 2\psi_1) \right\}$$

where $\varepsilon = v^2 - 2\varphi$. The first component is the "free" (or untrapped) group of electrons. They make up the bulk of the electrons, and are modeled here as a drifting Maxwellian function at $\varphi = 0$; as given, their temperature has been normalized (*i.e.*, to T_e/e). Reflected (or "trapped") particles populate the regions either $x > x_m$ or $x < x_m$ on each side of the double layer, and cannot communicate with each other; therefore, we have introduced two separate temparatures (β and δ) and two normalization constants (f_β and f_δ) for them. Here, electron velocity (v), the potential (φ), and the distance (x) are normalized to the electron thermal velocity $(T_e/m_e)^{1/2}$, the "free" electron temperature T_e/e, and the electron Debye length $\lambda_e = (T_e/4\pi n_0 e^2)^{1/2}$, respectively. Θ represents simply the Heaviside step function.

Since we are interested in describing ion acoustic double layers, we shall use a fluid formalism to describe the essentially cold ions:

$$(n_i)_t + (n_i u)_x = 0\,, \qquad u_t + u\,u_x + \varphi_x = 0 \tag{3}$$

Considering a time stationary situation, the above fluid ion model yields $n_i\,u = n_0\,u_0$ and $u^2/\,2 + \varphi = E_0$ where n_0, u_0 and E_0 are constants.

From these two species models, the corresponding densities for electrons and ions in the ion acoustic double layer frame can be found analytically by velocity-integration and Poisson's equation may be written by introducing a Sagdeev potential $V(\varphi)$ as follows:

$$\varphi_{xx} = -\frac{dV(\varphi)}{d\varphi} = n_e(\varphi) - n_i(\varphi) \quad . \tag{4}$$

The Sagdeev potential is found from the obvious first integral of Poisson's equation with appropriately chosen boundary conditions.

Numerically solving our nonlinear eigenvalue equation, we have been able to find that, in fact, there is a "critical" velocity for ion acoustic double layer solutions to exist. Arguing that the smallest *visible* potential dip in a simulation would be of order $\delta\varphi \geq 0.1$, the corresponding "critical" velocity for this amplitude solution to exist is found to be $v_d \approx 0.4 v_{th}$. This value is considerablly smaller than has been reported in other papers, and much closer to our simulation result (*i.e.*, that $v_d \geq 0.45 v_{th}$ was necessary before the current driven double layer would form). See Fig. 4.

Examining solutions to our nonlinear eigenvalue system, we have found that there are maximum amplitude limits for the negative potential dip $(-\psi_1)$; these depend on the electron drift velocity exceeding the critical value (Fig. 4).

We have also calculated ion drift velocities in the frame of ion acoustic double layers and found that the usual Bohm condition is *not* met in the case of ion acoustic double layers. In fact, the ion drift velocity decreases (below C_s) as both amplitudes of negative dip $(-\psi_1)$and net potential drop $(+\psi)$ increase (see Fig. 5). In confirmation, the simulation DL potential minima are always observed to move subsonically(Fig. 1 and 3).

With regard to the common identification made between the ion acoustic soliton and our double layer solutions, we point out that the velocity of the usual (rarefactive, having negative polarity) ion acoustic soliton *increases* with increasing amplitude; this character is in direct conflict with our earlier observation that the ion acoustic double layer slows down as it grows. It is important to note that net amplitude of an ion acoustic double layer correlates directly with the temperature difference between the two plasmas: the net potential drop (ψ)increases with increased temperature of reflected electrons on the high potential side(see Fig.2 (b)).

We would like to thank to Prof. C. K. Birdsall, Dr. M. Hudson, Dr. S. Kuhn, Dr. W. Lotko, Dr. J-P. Lynov, Dr. V. Thomas. We are grateful to Mr. N. Otani and Mr. W. Lawson for their computer simulation code. This work was supported by DOE Contract DE-AT03-76ET53064 at ERL, University of California, Berkeley.

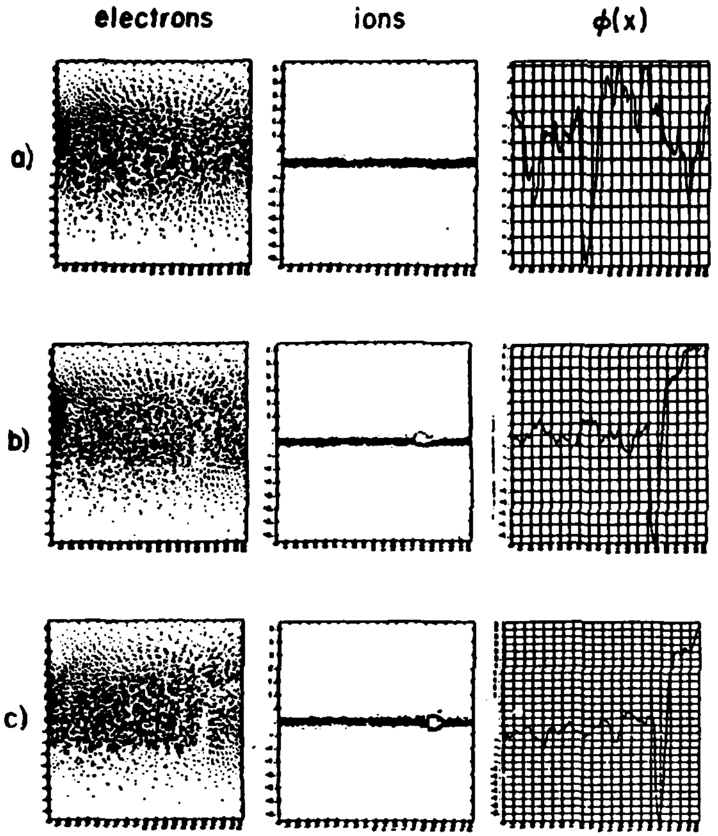

Fig. 1 (a) Simulation phase space for electrons, and ions and the potential profile at time $\omega_e t = 400$ for current driven system. Here, (b) and (c) is given at time $\omega_e t = 800$ and $\omega_e t =$ [illegible] respectively.

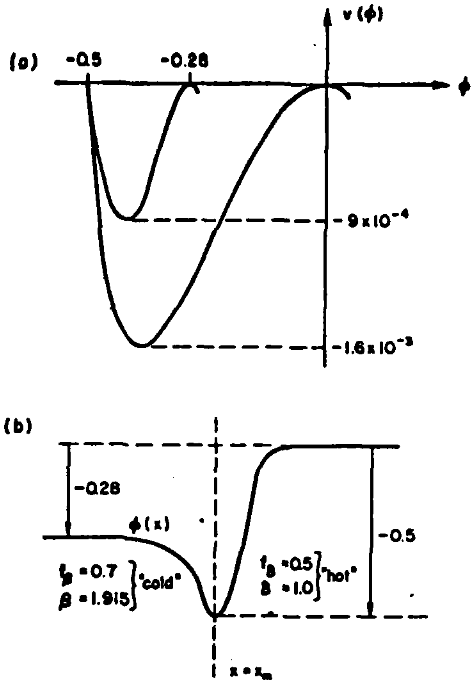

Fig. 2 (a) Calculated Sagdeev potential for ion acoustic double layer. (b) Corresponding ion acoustic double layer; using left side potential as a zero reference, then $\psi_1 = 0.5$ and $\psi = 0.28$(see text) with $v_d = 0.9$.

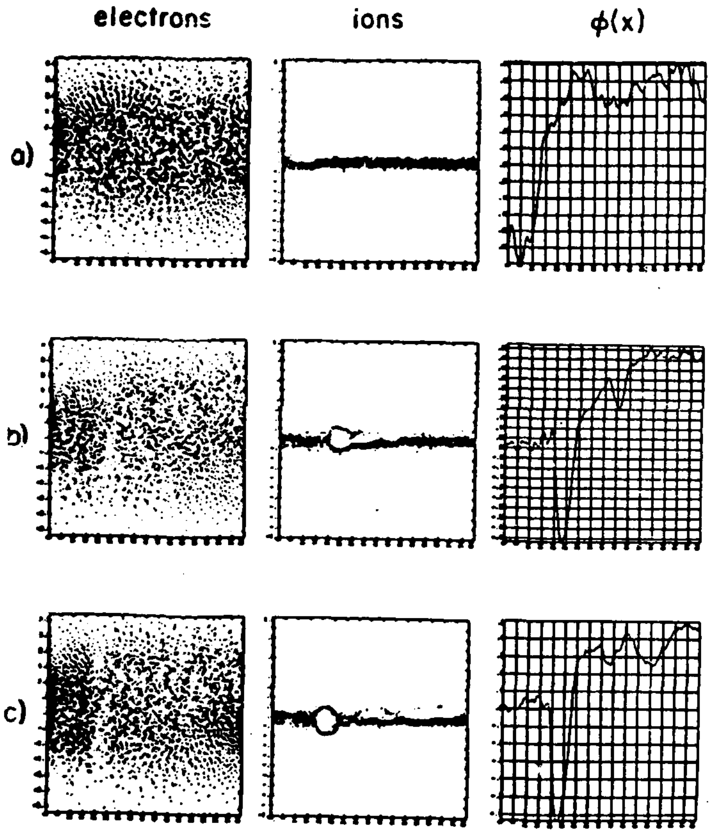

Fig. 3 (a) Similar phase space for electrons and ions, and potential profile at time $\omega_e t = 200$ for voltage driven system. Here, (b) and (c) is given at time $\omega_e t = 800$ and $\omega_e t = 840$, respectively.

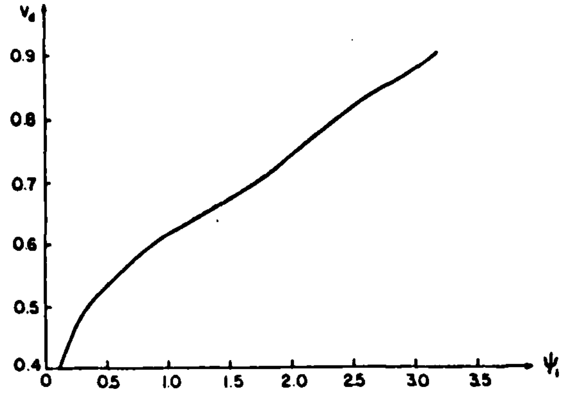

Fig. 4 Calculated electron drift velocity (v_d) and corresponding maximum ion acoustic double layer amplitude (ψ_i).

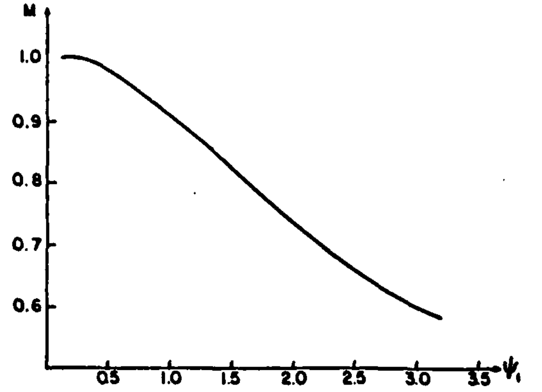

Fig. 5 Calculated ion acoustic double layer velocity(M) v.s. maximum amplitude(ψ_i).

SECTION II: CODE DEVELOPMENT

A. Uniform Number Generation (for Quiet Starts)*

N. Otani

We describe a simple pseudo-random number generator based on *n- roman reversing* . To each integer index i, a real funber f is assigned in the interval $(0,1)$ according to the following prescription:

1) Write i in base-n:

$$i = \sum_{p=0}^{P} m_p n^{-(p+1)}$$

Simply, to the integer i expressed in base-n

$$i = m_P \cdots m_2 m_1.0 \quad (\text{base} n)$$

the fraction

$$f = 0.m_1 m_2 \cdots m_P \quad (\text{base} n)$$

is assigned.

For the purpose of *loading* particles, the algorithm implemented need not be fast; the one shown here simply uses the above definition:

```
      subroutine nrev (i, fract, n)
c
c     Returns a fraction between 0 and 1 representing the
c     n-reversed number corresponding to i.
```

---

[*] See C. K. Birdsall and A. B. Langdon, *Plasma Physics via Computer Simulation*, McGraw Hill, 1985, Section 16-5, p. 393.

```
c   i    index to be n-reversed
c    fract:   number between 0 and 1 representing the
           integer in-reversed.
c   n   : the integer i will be reversed in base n.
           integer i, n
           real fract
c
           j = i
           fract = 0
           powern = 1.
10   jnext = j/n
           powern = powern/n
           fract = fract  +  (j-jnext*n)*powern
           if (jnext .eq. 0) return
           j = jnext
           go to 10
           end
```

SECTION III: JOURNAL ARTICLES, REPORTS, VISITORS, TALKS

Journal Articles

(1) S. Kuhn, "Linear longitudinal oscillations in collisionless plasma diodes with thin sheaths: Part I. Method," Phys. Fluids, *27*, 7 (July 1984) 1821.

(2) S. Kuhn, "Linear longitudinal oscillations in collisionless plasma diodes with thin sheaths: Part II. Application to an extended Pierce-type problem," Physics. Fluids, *27*, 7 (July 1984) 1834.

Reports

(1) T. L. Crystal, S. Kuhn, "Particle simulation of the low-α Pierce diode," Memorandum No. UCB/ERL M84/74, 20 September 1984, Electronics Research Laboratory, University of California, Berkeley.

(2) N. F. Otani, "Application of nonlinear constants of motion in a single electromagnetic wave to the study of the Alfven-ion-cyclotron instability," Memorandum No. UCB/ERL M84/49, 16 July 1984, Electronics Research Laboratory, University of California, Berkeley.

(3) K. P. Kenyan, "Simulation of Quiet Start Magnetized Plasmas, Including Maxwellian and Velocity-Space Ring Distributions," Memorandum No. UCB/ERL M84/64, 27 July 1984, Electronics Research Laboratory, University of California, Berkeley.

Poster Papers for the International Conference on Plasma Physics, June 27-July 3, 1985, Lausanne, Switzerland.

(1) (P8-11) S. Kuhn, C. K. Birdsall, T. L. Crystal, P. L. Gray, William S. Lawson, "One dimensional particle simulations of the collisionless single-ended Q machine." (The full paper was printed in the First and Second Quarter Progress Report of the Plasma Theory and Simulation Group. 1984.)

(2) (P33-11) T. L. Crystal and S. Kuhn, "Particle simulations of the low-alpha Pierce diode." (The full paper is Section I(G) of this Quarterly Progress Report.)

Poster Papers for the Second Symposium on Plasma Double Layers and Related Topics, July 5-6, 1984, Innsbruck, Austria.

(1) P. Gray, S. Kuhn, T. L. Crystal and C. K. Birdsall, "Particle simulations of the unstable states of a collisionless single-ended plasma device." (The full paper is in the Quarterly Progress Report I and II, 1984.)

(2) N. F. Otani, "Evolution of ion holes and large potential structures in simulations of bounded current-driven magnetized plasma systems." (The full paper is in the Quarterly Progress Report I and II, 1983, in essentially identical form.)

(3) K. Y. Kim and T. L. Crystal, "Double layers in formulation and theory." (The fullpaper is in Section I(H) of this Quarterly Progress Report.)

Notes:

The full paper of (2) is in the Quarterly Progress Report I and II, 1983, in essentially identical form; the full paper of (1) is in the Quarterly Progress Report I and II, 1984, and the full paper of (3) is in Section I(H) of the present report.

Poster Papers for the APS Division of Plasma Physics Meeting, November 1984, Boston, MA.

(1) William S. Lawson, "Simulations of obliquely propagating Berstein waves."

(2) C. K. Birdsall, William S. Lawson, T. L. Crystal, S. Kuhn, N. F. Otani, A. B. Langdon, "Plasma diode simulation: the PDW1 code."

(3) N. F. Otani, "Hybrid simulations of the gravitational instability in the presence of a large-amplitude RF wave."

(4) L. A. Schwager, "Simulation of charged particle reflection and emission effects in the plasma-sheath region."

Abstracts follow.

Visitors

(1) Dr. Michael J. Gerver, from the Plasma Fusion Center, Massachusetts Institute of Technology, was a visitor for two weeks in July 1984.

SIMULATION OF OBLIQUELY PROPAGATING BERNSTEIN WAVES*.

Wm. S. Lawson, *U.C. Berkeley, Electronics Research Laboratory.*

A modification of the code PDW1 is being used to simulate the boundary value problem for Bernstein waves propagating slightly off-perpendicular to the magnetic field. The numerical experiment is modeled after the Q-machine experiment of Armstrong et al.[1]. In the simulation, Bernstein waves are excited at one end of the simulation (which is assumed to be symmetric about the exciter). The exciter is a set of three grids, the outer two being tied together. Imposing a voltage between the inner and outer grids at a particular frequency generates Bernstein waves which are seen to propagate from the exciter across the system. Wave numbers and spatial damping rates (due to Landau damping) can be accurately measured and compared with linear theory. Effects observed include the onset of non-linearity at electric potential amplitudes of only a few percent of thermal energies.

[1] Armstrong, Rasmussen, Stenzel, and Trulsen, *Physics Letters*, 85A(1981)281-284.

* Work performed under Dept. of Energy contract DE-AT03-76ET53064 using the NMFECC computers at Livermore.

PLASMA DIODE SIMULATION: THE PDW1 CODE

C.K. BIRDSALL, Wm.S. LAWSON, T.L. CRYSTAL, S. KUHN, N.F. OTANI, A.B. LANGDON, *E.R.L., Univ. of Calif., Berkeley, CA 94720.**

PDW1 solves for electron and ion motions in the self-consistent electrostatic field of a 1d(1,2,3v) plasma device having external series RLC circuit as shown below. *The code and complete documentation are now available.* Among many options, one may model open circuit, short circuit, fixed potential drive, constant current drive, or a full RLC circuit. Standard code options include various particle injection schemes (e.g. drifting cutoff Maxwellians) from either or both electrodes, and a static magnetic field $\mathbf{B}_0$ at an angle ψ to the system axis. Recent applications, include the Pierce diode, weak and strong double layers both with and without $\mathbf{B}_0$, Bernstein waves, and magnetic sheaths and first walls. **PDW1** was produced for and during a Plasma Device Workshop.

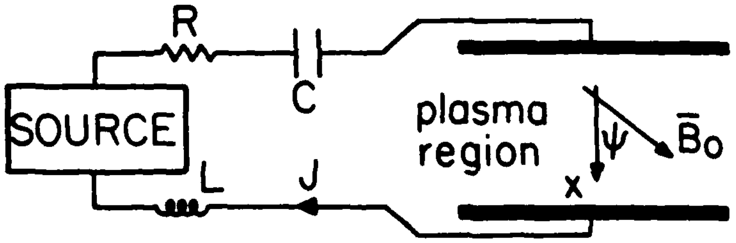

* Work was supported by DOE contract DE-AT03-76ET53064 and ONR contract N00014-77-C-0578. Computations were done at the NMFECC, Livermore.

Hybrid Simulations of the Gravitational Instability in the Presence of a Large-Amplitude RF Wave. **NIELS F. OTANI,** *Electronics Research Lab, U. of Calif., Berkeley, CA 94720.** A 2 1/2-d particle-ion, fluid-electron nonlinear Darwin simulation code has been developed for the study of the behavior of the gravitational instability in an equilibrium modified by ponderomotive and other effects due to the presence of a large-amplitude RF wave in the ion-cyclotron frequency range. No change is observed in the linear growth rate of the instability when the RF wave is loaded as a long-wavelength ($k_\perp \sim L_n^{-1}$), compressional Alfvén standing wave in a cold plasma with initial amplitude $e^2 \nabla |E|^2 / 4 m^2 \omega^2 g \sim O(1)$; however, this type of wave lacks the usual ion-cyclotron resonance. A theoretical prediction of the second-order RF-wave-induced d.c. current in the $\mathbf{k}_\perp \times \mathbf{B}_0$-direction in a uniform plasma agrees with results obtained from simulation, with assessment of the current's stabilization properties still pending. Further simulations employing waves exhibiting the ion-cyclotron resonance (i.e., finite-$k_\parallel$ Alfv' n waves or ion-Bernstein waves) as well as antenna-launched waves are anticipated.

*Work supported by DOE Contract. No. DE-AT03-76ET53064; computation facilities provided by NMFECC.

SIMULATION OF CHARGED PARTICLE REFLECTION AND EMISSION EFFECTS IN THE PLASMA-SHEATH REGION,*

L.A. SCHWAGER, U.C. BERKELEY, E.R.L., CA 94720

The plasma sheath region is modelled by a one-dimensional, time-dependent system using PDW1, which simulates the injection of particle ions and electrons from a plasma region into a grounded plate. At this plate electrons and ions are reflected, emitted, and absorbed. Current work indicates that a reflected ion current increases the plasma potential above that generated with a purely absorbing plate. Also presented is a parametric study of the effects of secondary electron emission and of charged particle reflection on the potential profile and on particle and energy transport to the wall.

* Work supported by DOE contract DE-AT03-76ET53064

DISTRIBUTION LIST

Department of Energy
Hitchcock. Katz. Lankford. Nelson. Sadowski

Department of Navy
Condell. Florance. Roberson

Austin Research Associates
Drummond. Moore

Bell Telephone Laboratories
Hasegawa

Cal. Inst. of Technology
Liewer. Bridges. Gould

Calif. State Polytech. Univ.
Rathmann

Cambridge Research Labs
Rubin

Columbia University
Chu

E. P. R. I.
Scott

General Atomic Company
Bernard. Helton. Lee

Hascomb Air Force Base
Rubin

Hughes Aircraft Co., Torrance
Adler. Longo

Hughes Research Lab, Malibu
Harvey. Poeschel

JAYCOR
Hobbs. Klein. Tumolillo. Wagner

Kirtland Air Force Base
Pettus

Los Alamos National Lab.
Barnes. Borovsky. Forslund. Kwan. Lindemuth. Mason. Mostrom. Nielson. Oliphant. Sgro. Thode

Lawrence Berkeley Laboratory
Cooper. Kaufman.Kim. Kunkel. Lee. Pyle

Lawrence Livermore National Lab
Albritton. Anderson. William Barr. Brengle. Briggs. Bruijnes. Byers. Chambers. Chen. B. Cohen. R. Cohen. Denavit. Estabrook. Fawley. Friedman. Fries. Fuss. Harte. Hewett. Killeen. Kruer. Langdon. Lasinski. Maron. Matsuda. Max. Nevins. Nielsen. Smith. Tull

Mass. Inst. of Technology
Berman. Bers. Gerver.

Mission Research Corporation
Godfrey

Naval Research Laboratory
Boris. Craig. Haber. Orens. Winsor

New York University
Grad. Harned. Weitzner

Northeastern University
Silevitch

Oak Ridge National Lab.
Dory. Meier. Mook

Princeton Plasma Physics Lab
Chen. Cheng. Lee. Okuda. Tang. Graydon

Sandia Labs, Albuquerque
Freeman. Humhries. Poukey. Quintenz. Wright

Sandia Labs, Livermore
Marx

Science Applications, Inc.
Drobot. Mankofsky. McBride. Siambis. Smith

Stanford University
Blake. Buneman

University of Arizona
Morse

University of California, Berkeley,
Arons. Chorin. Grisham. Hudson. Keith. Lichtenberg. Lieberman. McKee. Morse. Birdsall. Lawson. Otani. Theilhaber. Wendt

University of California, Davis
DeGroot. Woo

University of California, Irvine
Rynn

University of California, Los Angeles
Dawson. Decyk. Huff. Lin

University of Iowa
Knorr. Nicholson

University of Maryland
Gillory. Rowland. Winske

University of Pittsburgh
Zabusky

University of Texas
Lebouef. Horton. McMahon. Tajima

Institute of Fusion Studies
Librarian

University of Washington
Potter

University of Wisconsin
Shohet

Varian Associates
Helmer

Bhabha Research Centre
Aiyer. Gioel

Culham Laboratory
Eastwood

Ecole Polytechnique, Lausanne
Hollenstein. Rousset

Ecole Polytechnique, Palaiseau
Adam

Centro de Electrodinamica, Lisbon
Brinca. Crystal

Kyoto University
Abe. Jimbo. Matsumoto

Nagoya University
Kamimura

Max Planck Inst. für Plasmaphysik
biskamp. Kraft. Chodura

Osaka University
Mima. Nishihara

Oxford University
Allen

Riso National Labs
Lynov. Pecseli

Tel Aviv University
Cuperman

Tohoku University
N. Sato

Universität Bochum
Schamel

Universität Innsbruck
Cap. Kuhn

Universität Kaiserslautern
Wick

University of Reading
Hockney

University of Tromso
Trulsen. Armstrong

END

FILMED

4-86

DTIC